Design and Development of Homo/Hetero Junction-based 2D Materials for Supercapacitor Application

A Dissertation Submitted to the
Indian Institute of Technology Guwahati
in Partial Fulfilment for the Degree of

DOCTOR of PHILOSOPHY

by

Alpana Sahu
Roll No. 206122101

DEPARTMENT OF CHEMISTRY

INDIAN INSTITUTE OF TECHNOLOGY GUWAHATI

GUWAHATI, ASSAM, INDIA

STATEMENT

I hereby declare that the scientific findings included in this thesis entitled, "**Design and Development of Homo/Hetero Junction-based 2D Materials for Supercapacitor Application**" is the outcome of research work carried out by me under the supervision of Prof. Mohammad Qureshi, at the Department of Chemistry, Indian Institute of Technology Guwahati, Assam, India, for the award of the degree of Doctor of Philosophy.

The work embodied in this thesis is the result of original research done by me, except where otherwise stated in this thesis, with proper citations. I confirm that the investigations were conducted in accordance with the ethics policies and integrity standards of the Indian Institute of Technology Guwahati, and that the research data are presented honestly and without bias. The thesis work has not been submitted for a degree or professional qualification to any other university or institution.

IIT Guwahati
September 2025

Alpana Sahu
Candidate
Department of Chemistry
IIT Guwahati, Guwahati-781039,
Assam, India

Mohammad Qureshi
Department of Chemistry
Indian Institute of Technology Guwahati
Guwahati – 781039, India
Email: mq@iitg.ac.in

CERTIFICATE

Certified that the work described in this thesis entitled "**Design and Development of Homo/Hetero Junction-based 2D Materials for Supercapacitor Application**" by Ms. Alpana Sahu, Department of Chemistry, Indian Institute of Technology Guwahati, has been carried out under my supervision and has not been submitted elsewhere for a degree.

Guwahati
September 2025

Mohammad Qureshi
Thesis supervisor
Department of Chemistry
Indian Institute of Technology Guwahati
Guwahati – 781039, Assam, India

Dedicated To

My Parents and Family

ACKNOWLEDGEMENTS

It gives me immense pleasure to express my heartfelt gratitude to all those who have contributed to the successful completion of my Ph.D. thesis. This journey has been both beautiful and memorable, made possible by the unwavering support and encouragement I received along the way. As I reflect on the years devoted to this pursuit, I am deeply thankful to everyone, both directly and indirectly, who played a role in helping me reach this milestone.

Foremost, I would like to express my deepest gratitude to my Supervisor, Prof Mohammad Qureshi, for giving me the opportunity to work under his expert supervision. I am immensely grateful for his invaluable guidance and constant support throughout my PhD journey. His insightful feedback and encouragement greatly contributed to shaping me as well as my research. His belief in my potential, even during moments of self-doubt, was a constant source of motivation. His patience, vision, and unwavering faith in my abilities have been a continual source of inspiration, and I consider myself extremely fortunate to have had the chance to develop under his guidance.

I am extremely grateful to my doctoral committee members, Dr. Kalyan Raidongia, Dr. Akshai Kumar Alape Seetharam, and Dr. Selvaraju Narayanasamy for their assistance and suggestions throughout my PhD work. Additionally, I would like to recognize Dr. Kalishankar Bhattacharyya and Partha Pratim Borah for helping me with theoretical calculations, which gave me a better insight into my research work.

A special thanks to the Indian Institute of Technology Guwahati and the Ministry of Health and Research Development for providing all the necessities and financial support to carry out my research work. I would also extend my gratitude to all the faculty members and staff members of Department of Chemistry for their help regarding various aspects. My sincere thanks to the staff of Central Instruments Facility for their help and guidance in the utilization of the various instrumental facilities. A special thanks to Sujit Kumar Deb and Rupak for teaching me the operation of FETEM instrument.

My lab seniors have been a source of support and energy, and their indispensable input and guidance are worth mentioning. Dr. Tushar Kanta Sahu, Dr. Suhaib Alam and Dr. Adit Kumar Shah, thank you for being the tutors and motivation in the lab. Special thanks to Dr. Sourav Bhowmick, Dr. Manoj Kumar Mohanta, and Dr. Ching Thian Moi for being not just mentors but also friends who made my lab life more comfortable. Your guidance has been truly invaluable. And my lab colleagues, Dr. Bishal Das. Nitul Kalita, Peeyush Pandey, N Anjana Singha, Priyanka Ray, Dikshita Goswami, Ankit Sharma, Ankit Kumar Singh, and Prithiviraj Patra I appreciate your timely assistance, support, and for creating a friendly environment in the lab.

To my dearest friends, thank you for being my pillars of strength, for listening patiently, cheering me on, and believing in me even when I doubted myself. Rani and Rajashree, my best friends, you have always been there through my thick and thin days, encouraging me to continue my research. Jagnyesh, having you as a friend once again at IITG has truly been a comforting presence, and thank you for always being there to help me. Thank you, my wonderful M.Sc. friends Prangya, Swarna, Gourab, Arun, Aisa, Jitu, Siddhu Dada, Bikas, Abhipsa, Abhijit, and Anandita for the shared struggles, thoughtful discussion, and constant support that inspired my research journey. My friends at IITG have been my pillars of strength and motivation to carry out my PhD work. Neha, Pallavi, Megha, Nilotpola, Priti Didi, Mira, Dharismita, Soumya, and Biswa, you guys were like a family at IITG. Whether in small moments or big milestones, you were always by my side, motivating me to keep going. Thank you, Dr. Abhijeet Rana, for your constant encouragement, caring presence, and unwavering belief in me throughout this journey. I extend my sincere thanks to my beloved seniors, Umesh Bhai, Moumita Didi, and Meghali Didi for their care, love, and support.

ACKNOWLEDGEMENTS

I would like to thank all my teachers for believing in me and motivating me to achieve my goal. Special mention goes to my teachers at Sambalpur University, Prof. Pramila Kumari Mishra, Dr. Hirak Chakraborty, Dr. Satya Narayan Sahu, Dr. Amaresh Mishra, Prof. Pradipta Kumar Behera, Dr. Ram Naresh Mahaling, and Dr. Naba Krushna Behera for inspiring and implanting in me a love towards research for this subject. I would also like to extend my gratitude to all my teachers from my school, 12th, and Bachelor's for their direct or indirect support and motivation which guided me to reach this far.

Finally, my Ph.D. endeavour could not have been completed without the endless love, unending support, tolerance, and blessings from my family. I owe a debt of gratitude to my mother Tribeni Sahu and father, Prafulla Sahu, whose belief in me has always been a source of motivation. My Sister Kalpana Sahu, my brother Ankit Sahu, and my brother-in-law, Sushanta Sahu, always stood by me, supporting me in every challenge. I express my love to my niece Khusi, whose smile brought immeasurable joy to my life. I also dedicate my work to my Aja Prabhat Kumar Sahu and Aai Basanti Sahu, who always encouraged and inspired me in my studies to build a better future. Also, dedicated to my Jeje Harekrushna Sahu and Dadima Rangalata Sahu for their endless love and affection.

Still, many names are missing whose contributions and help are worth mentioning.

Alpana

Table of Contents

hesis Title:	**Design and development of homo/hetero junction-based 2D materials for supercapacitor application**
Name of the Candidate:	Alpana Sahu
Registration Number:	206122101
Thesis Supervisor:	Prof. Mohammad Qureshi
Department:	Chemistry
Institute:	Indian Institute of Technology Guwahati, Assam – 781039, India.

Thesis Overview

Chapter 1: Introduction

A comprehensive overview of supercapacitors as vital components of electrochemical energy storage systems has been discussed here. It highlights the growing demand for sustainable and efficient storage solutions, emphasizing the critical role of supercapacitors. Recent advances in 2D electrode materials, featuring high surface area, tunable band gap, and unique electronic properties, are discussed. Additionally, strategies like hybridization and surface modification are explored to enhance their charge storage capacity and scalability for practical applications. The chapter concludes with the objectives and motivation that led to the design and fabrication of several 2D material-based electrodes for supercapacitor applications.

Chapter 2: Experimental

The instrumental methods and procedures employed for material characterization and device fabrication are outlined, along with a brief overview of key electrochemical analysis techniques such as cyclic voltammetry, galvanostatic charge-discharge, and electrochemical impedance spectroscopy, followed by distribution of relaxation time analysis.

Chapter 3: Internal Stimuli Strategy: High-valent vanadium-enabled redox activation and NiMn-LDH synergy for advanced supercapacitors

A synergistic strategy was employed by integrating high-valent vanadium into CoO(OH) and coupling it with 2D NiMn-LDH nanosheets to enhance electrochemical performance. The incorporation of vanadium ions improved surface hydrophilicity and increased electrolyte ion adsorption, thereby boosting the redox activity of Co ions. Simultaneously, the deposition of NiMn-LDH nanosheets onto the hexagonal CoVO(OH) structure significantly expanded the surface area and increased the number of electroactive sites. This optimized composite

delivered a high specific capacity of 786 C g^{-1} at 1 A g^{-1}, with a retention of 75% at 10 A g^{-1}. Long-term cycling stability was demonstrated with 96% capacity retention after 5000 cycles at 10 A g^{-1}, outperforming the bare CoVO(OH)/CP, which retained only 88%. The assembled asymmetric supercapacitor NiMn-LDH@CoVO(OH)/CP//AC achieved an energy density of 46 Wh kg^{-1} at a power density of 752 W kg^{-1}. The practical viability of the device was further validated by powering a 3V LED using two units connected in series under ambient conditions.

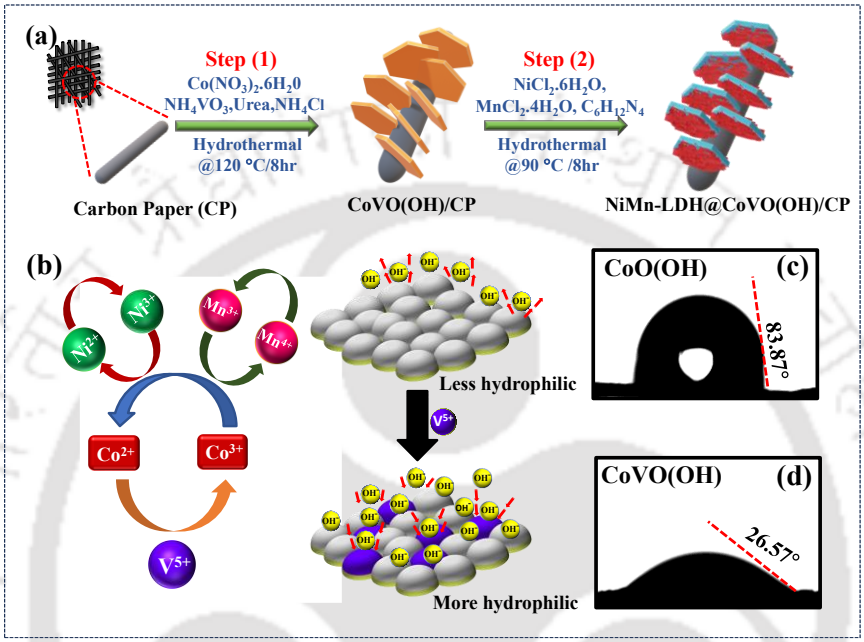

Figure 3.1: (a) Schematic representation of the synthetic protocol used for the fabrication of the composite electrode (NiMn-LDH@COV/CP), (b) Schematic representation of the proposed plausible mechanistic pathway involving the contribution of spectator ion vanadium along with redox-active ions such as cobalt, nickel, and manganese. Contact-angle measurements of (c) CoO(OH) and (d) CoVO(OH) showing an increase in hydrophilicity with incorporation of vanadium (*Chem. Comm.* **2023**, 59, 1038)

Chapter 4: Redox-Capacitive Interplay: Redox-active $Mn_2V_2O_7$ rods integrated with MXene sheets for enhanced charge transfer

A strategic approach that combines capacitive and redox-active materials to address the challenges faced by traditional supercapacitors in terms of high-power delivery and increased energy density was implemented. We have effectively utilized a combination of MXene and manganese vanadium oxide ($Mn_2V_2O_7$) nanorods to address challenges related to the restacking of MXenes. Formation of pathways for ion migration in the $Mn_2V_2O_7$/MXene composite, resulting in increased conductivity, enhanced ion transport capacity, and structural stability in aqueous electrolytes, gives high performance with a specific capacitance of 627 Fg^{-}

[1] at 1 Ag^{-1}. Furthermore, the assembled device $Mn_2V_2O_7$/MXene//AC demonstrated a high potential window of 2 V with an energy density of 65 Wh kg^{-1} at a power density of 1000 W kg^{-1}. To gain deeper insights into the electrochemical processes, we have utilized the Distribution of Relaxation Time (DRT) analysis to extract complex impedance spectra. This approach enhances the resolution and provides a comprehensive understanding of the dynamics of charge transfer kinetic processes involved in our developed supercapacitor system.

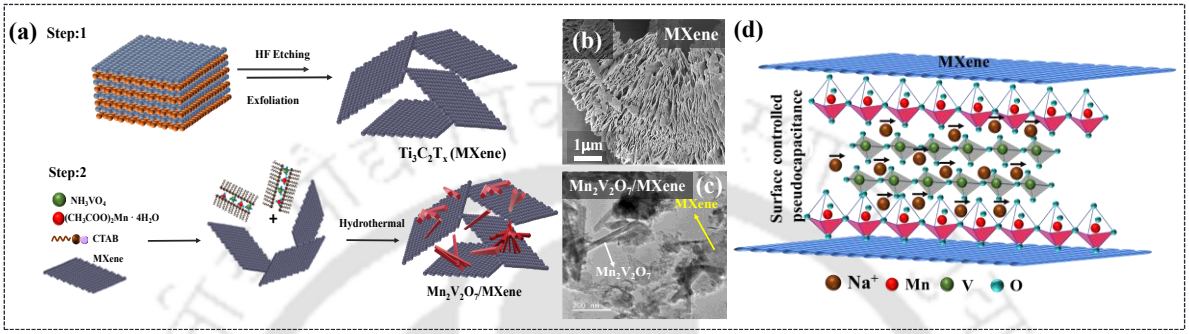

Figure 4.1: (a) Schematic of the synthesis procedure in 2 steps, etching and delamination MAX phase to form MXene (Step 1) and hydrothermal synthesis of $Mn_2V_2O_7$/MXene composite (Step 2) (b) FESEM image of exfoliated MXene and (c) FETEM image of MXene/$Mn_2V_2O_7$ (d) Probable mechanism of charge storage in the $Mn_2V_2O_7$/MXene composite. (*ACS Appl. Energy Mater.* **2024**, 15, 6062)

Chapter 5: Boron and Oxygen-Coordinated Heterostructures: Interface-driven electronic modulation for high-performance supercapacitors

In this chapter, we have utilized the electron deficiency of boron, arising from its vacant p-orbital, which readily interacts with the lone pair electrons of oxygen, enhancing electron delocalization and electrical conductivity. Such interactions are leveraged to improve the performance of supercapacitor electrodes.

Chapter 5a: Metal-free Borophene/rGO composite with Dirac semi-metallicity for supercapacitors

A flexible, metal-free rGO-supported borophene electrode was explored for energy storage applications. By leveraging the unique semi-metallic Dirac properties of borophene and increasing the interlayer spacing between rGO and borophene, the ion diffusion and electrochemical performance were enhanced significantly. The results demonstrate a high specific capacitance of 328 Fg^{-1} at 1 Ag^{-1}, along with excellent rate capability and cycling stability. The fabricated flexible symmetric supercapacitor achieves an energy density of 24.3 Wh kg^{-1} at a power density of 600 Wkg^{-1} and maintains a stable energy output even under

bending angles of up to 180°. To gain a deeper understanding of the electrochemical processes, we employed Distribution of Relaxation Time (DRT) analysis to extract complex impedance spectra. This method improves resolution and offers a comprehensive view of the charge transfer kinetics in the supercapacitor system. Additionally, we have performed theoretical calculations using DFT to support our experimental results. The DFT study reveals that the contributions of boron (B) and carbon (C) atoms at the Fermi level impart semi-metallic properties to the composite material, enhancing ion transfer and improving charge storage capacity.

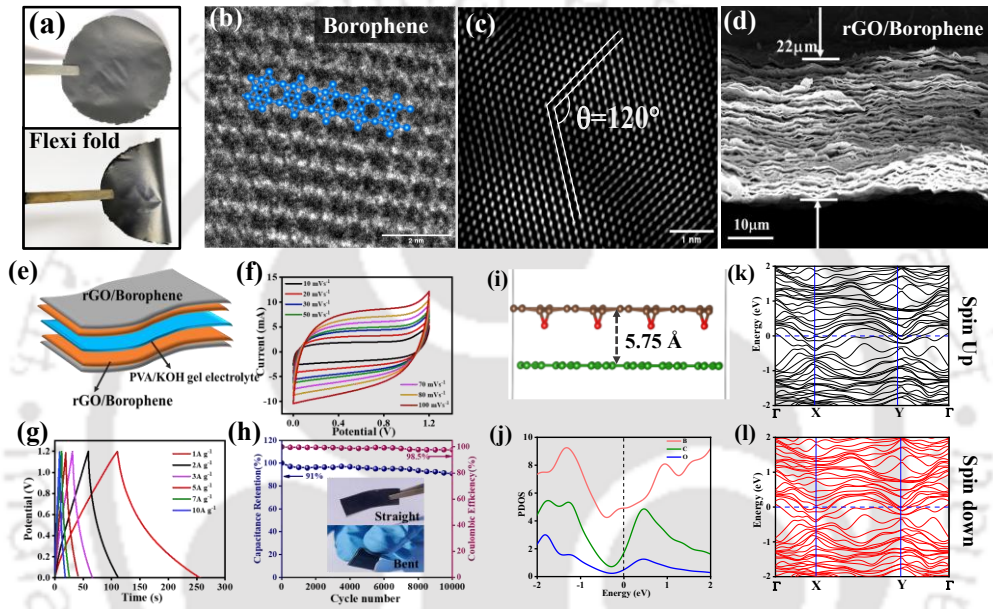

Figure 5a.1: (a) Photographic images of the hybrid film under flexible geometrical configuration. (b) Honeycomb lattice of borophene. (c) Corresponding fast Fourier transform pattern of image (d) Cross-sectional FESEM image of the rGO/borophene 2D hybrid electrode. (e) Schematic presentation of the device tested. (f) CV (g) GCD curves of (h) Long-term cycling performance and Coulombic efficiency of the rGO/Bp//rGO/Bp device (photographic image of FSS). heterolayer structure of (i) borophene with rGO (j) PDOS calculation, Spin-polarized electronic band structure of rGO/borophene for structure (k) spin-up and (l) spin-down band structure (*Nano Lett.* **2025**, 25, 5019)

Chapter 5b: Homo-interface engineering of O-Doped and B-Doped g-C_3N_4 composite for energy storage

Utilizing the intrinsic electric field of a *p–n* junction electrode, which enhances charge transport at the interface, this chapter presents a novel method for improving electrochemical energy storage. This study presents the rational design of a heterostructure electrode material that consists of n-type oxygen-doped g-C_3N_4 (O:g-C_3N_4) nanosheets combined with p-type

boron-doped g-C_3N_4 (B: g-C_3N_4) hollow nanotubes, resulting in a well-defined homo-interface (p–n) junction. The doping strategy successfully reduces the band gap of g-C_3N_4, with O: g-C_3N_4 and B: g-C_3N_4 showing band gaps of 2.6 eV and 2.3 eV, respectively, which leads to

improved electrical conductivity. The unique hollow tubular morphology of B: g-C_3N_4 coupled with the layered structure of O: g-C_3N_4, affords a high surface area and short ion diffusion paths. The redistribution of charge within the p-n junction leads to the formation of space-charge regions and an internal electric field, which promotes charge transfer and subsequently increases intrinsic activity. Leveraging these benefits, the optimal B: g-C_3N_4/O: g-C_3N_4 composite electrode achieves a remarkable specific capacitance of 366 F g^{-1} at 1 A g^{-1}. An asymmetric coin cell supercapacitor (B: g-C_3N_4/O: g-C_3N_4//AC) was further assembled, achieving an energy density of 24 Wh kg^{-1} at a power density of 700 W kg^{-1}, and demonstrating 83% capacitance retention and 100% coulombic efficiency after 20,000 charge–discharge cycles. This work highlights the importance of homo-interface *p-n* junction engineering in improving the electrochemical performance of metal-free electrode materials for energy storage applications.

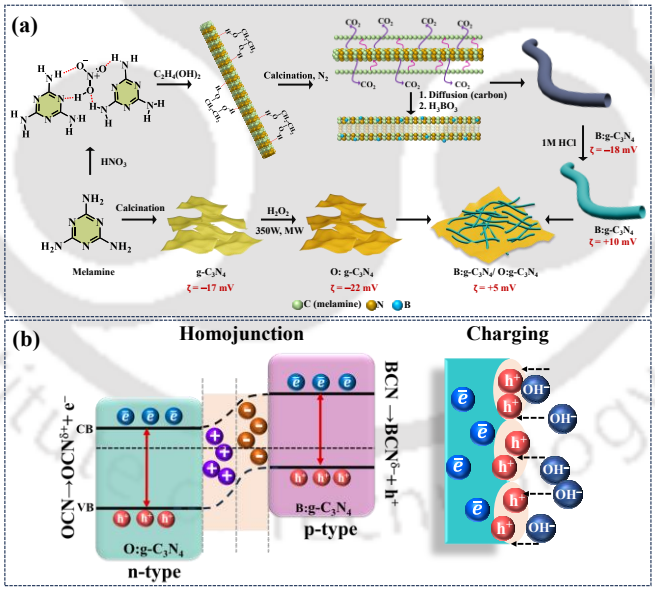

Figure 5b.1: (a) Schematic illustration of the synthesis routes for B: g-C_3N_4, O: g-C_3N_4, and the B: g-C_3N_4/O: g-C_3N_4 homojunction composite. (b) p–n Homojunction Formation and band alignment in B: g-C_3N_4 /O: g-C_3N_4, enhancing electrolyte adsorption during charging via polarization induced by the Built-in Electric Field *(Manuscript in revision)*

CHAPTER 1

Introduction and Literature Survey

A comprehensive overview of supercapacitors as vital components of electrochemical energy storage systems has been discussed here. It highlights the growing demand for sustainable and efficient storage solutions, emphasizing the critical role of supercapacitors. Recent advances in 2D electrode materials, featuring high surface area, tunable band gap, and unique electronic properties, are discussed. Additionally, strategies like hybridization and surface modification are explored to enhance their charge storage capacity and scalability for practical applications. The chapter concludes with the objectives and motivation that led to the design and fabrication of several 2D material-based electrodes for supercapacitor applications.

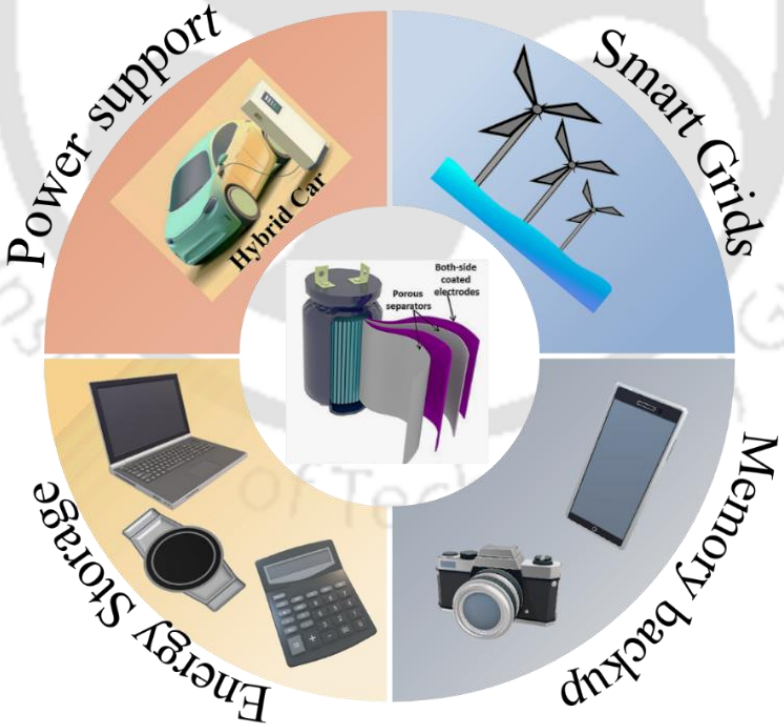

Chapter 1

1.1.ENERGY STORAGE SYSTEMS:

Electricity, a vital and widely utilized energy source of modern life, is essential for powering homes, businesses, and technologies around the world.[1–3] The rapid increase in energy demand, which is mostly due to industrial growth, reliance on fossil fuels like coal, oil, and gas, has led to urgent environmental issues like global warming and rising greenhouse gas emissions. To combat these issues, it is crucial to reduce the use of fossil fuels and transition to renewable and sustainable energy sources such as solar, wind, and tidal energy.[4–6] Renewable energy now makes up a larger share of the energy supply, with solar and wind power being major contributors to the central grid. However, these energy sources have limitations, such as being dependent on weather conditions, which makes their energy output inconsistent and unpredictable. This inconsistency can complicate the delivery of reliable and high-quality electricity to the grid and end-users. To overcome these challenges and increase the use of renewable energy in power generation, effective energy storage systems are essential.[7,8] These systems can store excess energy when production is high and release it when needed, helping to smooth out fluctuations in energy supply. They also protect power grids and generators, extending their lifespan by improving frequency regulation and reducing the need to meet sudden peaks in energy demand.[9,10]

Recent years have witnessed a surge in interest in electrochemical energy storage (EES) devices owing to their important contribution to modern energy technologies.[6] There are various types of EES systems, in which supercapacitors (SCs) and rechargeable batteries have been highlighted.[11,12] Rechargeable batteries have a high energy density, but their power density is standard, and their efficiency and cycle life are low relative to those of SCs.[13] The remarkable characteristics include extremely high-power density, minimal maintenance requirements, long operational lifespans, rapid charge/discharge capabilities, broad working temperature ranges, and inherent safety and stability, SCs have attracted significant attention and position it as strong contenders for next-generation energy storage technologies, making them ideal for repetitive use.[14,15] Due to their versatility and reliability, supercapacitors can be used in a variety of applications, including electric vehicles (EV), hybrid electric vehicles (HEV), uninterruptible power supplies (UPS), portable electronic devices (PED), grid load levelling, peak power saving, and frequency regulation.[16–18]With their capacity to meet the evolving challenges faced by modern energy systems, supercapacitors are positioned in their transformative role in the future of energy storage.[19–22]

1.2. ELECTROCHEMICAL SUPERCAPACITORS: FUNDAMENTALS

Among various methods of energy storage that ensure a controlled and reliable supply, EES stands out as one of the most efficient solutions, offering superior energy conversion rates. Key examples of EES systems include fuel cells, batteries, supercapacitors (also known as electrochemical capacitors), and traditional capacitors.[12,23] While batteries have traditionally dominated the EES landscape, but they face notable challenges such as limited cycle life, safety concerns, and low power density, which prevent them from being the ultimate energy storage solution.[24,25] As illustrated in **Figure 1.1**, supercapacitors offer distinct advantages in power management compared to batteries and capacitors. Although they exhibit a moderate energy density than batteries of similar size, their power density is significantly higher.[26,27] This distinct feature enables supercapacitors to be well-suited for applications where quick energy is required. Additionally, integrating supercapacitors with batteries in a hybrid energy storage system allows taking advantage of both technologies that maximizes both power and energy capabilities. In recent years, supercapacitors have gained considerable attention, particularly with two-dimensional (2D) electrode materials. These materials have unlocked new possibilities for enhancing supercapacitor performance, paving the way for advanced energy storage technologies.[28,29]

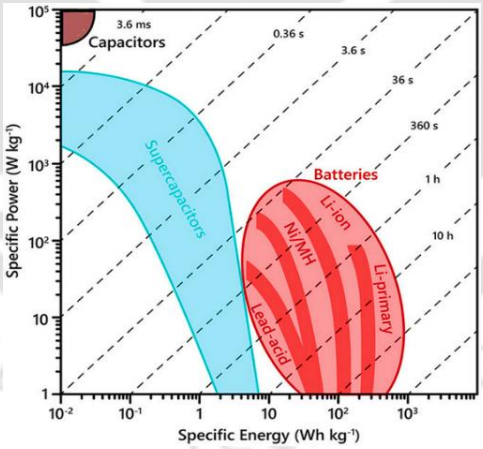

Figure 1.1. Ragone plot comparing the power and energy densities of various electrical energy storage devices, Adapted from ref. [30]

In the case of a capacitor, a dielectric medium separates the two parallel capacitor plates, and when voltage is applied, charge is stored electrostatically on the plates. The capacity of such a device is defined as,

$$C = \frac{\varepsilon A}{d} \quad \ldots. (1.1)$$

where ε, A, and d are the dielectric constant, electrode area, and distance between the metal plates, respectively. The given equation explains, capacitance is solely dependent on the area of the capacitor plate and the distance between them in the device. Capacitors can store charge through electrostatically rather than chemical reactions, unlike batteries. This fundamental difference limits their charge storage capacity compared to other energy storage systems, as it is constrained by the available surface area and the small separation between the plates. In an electrochemical supercapacitor, solvated electrolyte ions replace the traditional dielectric material, storing charge at the electrode-electrolyte interface when a bias is applied. When the electrodes are polarized, solvated ions with opposite charges migrate toward the corresponding electrodes, forming a dielectric layer of water molecules between the polarized electrode surface and the layer of solvated ions.[31] The atomistic separation created by the water layer significantly increases capacitance. Furthermore, using 2D materials instead of traditional metal plates substantially increases the surface area of the electrode, increasing its energy storage capacity.

Depending on the interfacial charge storage mechanism, electrochemical capacitors are generally categorized into three different categories: (a) Electrochemical double-layer capacitors (EDLC), (b) pseudocapacitors, and (c) hybrid capacitors.[32]

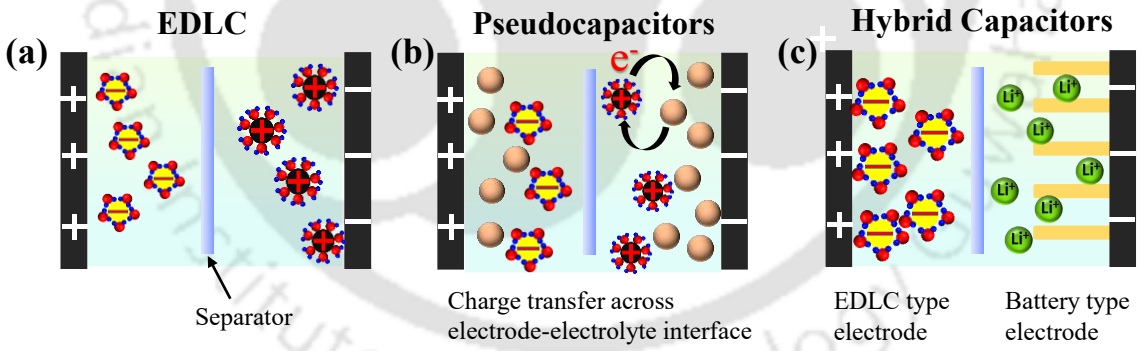

Figure 1.2: Schematic representation of different electrochemical capacitors (a) an electric double layer capacitor (EDLC), (b) a Pseudocapacitor, and (c) a hybrid system that comprises an EDLC and an intercalative charge storage process.[32]

1.2.1. Electrochemical double-layer capacitors:

An electric double-layer capacitor (EDLC) is a fascinating device that stores energy by separating charges at the interface between the electrode and the electrolyte. When the conductive electrodes are dipped into an ion-conductive electrolyte, an opposite charge is gathered at the electrode surface, creating a double layer that is separated by a thin layer of

solvent molecules. These solvated molecules act as a barrier, preventing charge transfer between the electrode and the electrolyte, which means energy is stored electrostatically instead of through faradaic reactions.[33] To achieve better performance in supercapacitors, electrodes with a high surface area and good conductivity are essential. A significant amount of research has focused on graphite carbon electrodes, which are considered the best options for pure EDLC energy storage owing to their high surface area, affordability, easy availability, and well-established production methods.[34] The capacitance of these materials is influenced by several factors, including specific surface area, pore shape, size distribution, surface functionality, and electrical conductivity. A larger surface area means more room for charge accumulation, while surface functionalization and the right pore structure are key to boosting their specific capacitance.[35] Additionally, their impressive electrochemical stability across different electrolytes makes them reliable candidates for pH-independent EDLC electrode materials.[36]

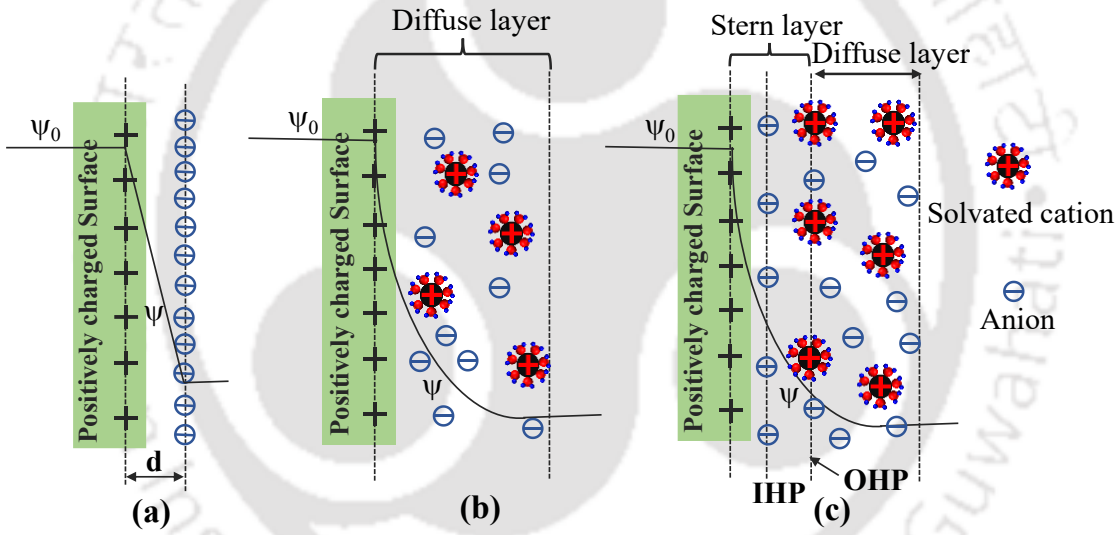

Figure 1.3: Models of the electrical double layer at a positively charged surface: (a) the Helmholtz model, (b) the Gouy–Chapman model, and (c) the Stern model, showing the inner Helmholtz plane (IHP) and outer Helmholtz plane (OHP).[37]

Several models have been proposed for EDLC formation at the interface of electrode-electrolyte, starting from the first description ever proposed in 1853 by Helmholtz.[38] The concept of the EDL was first modelled by von Helmholtz, who described it as two layers of opposite charges at the electrode/electrolyte interface, separated by an atomic distance, resembling a parallel plate capacitor. Gouy and Chapman refined this model by introducing a diffuse layer where ions are distributed due to thermal motion, but their approach overestimated capacitance by not accounting for ion size and proximity effects.[39] Stern later combined the

Helmholtz and Gouy–Chapman models, introducing two regions: the compact (Stern) layer, which includes the **inner Helmholtz plane (IHP)** of specifically adsorbed ions, and the **outer Helmholtz plane (OHP)** of non-specifically adsorbed counterions, and the diffuse layer, where ions are distributed as described by the Gouy–Chapman model.[37,40] This hybrid model provides a more accurate depiction of ion behavior and capacitance in the EDL. The total double-layer capacitance of this arrangement can be considered as two capacitors in series, such that:

$$\frac{1}{C_{dl}} = \frac{1}{C_{IHP}} + \frac{1}{C_{OHP}} \quad \ldots.(1.2)$$

1.2.2. Pseudocapacitors:

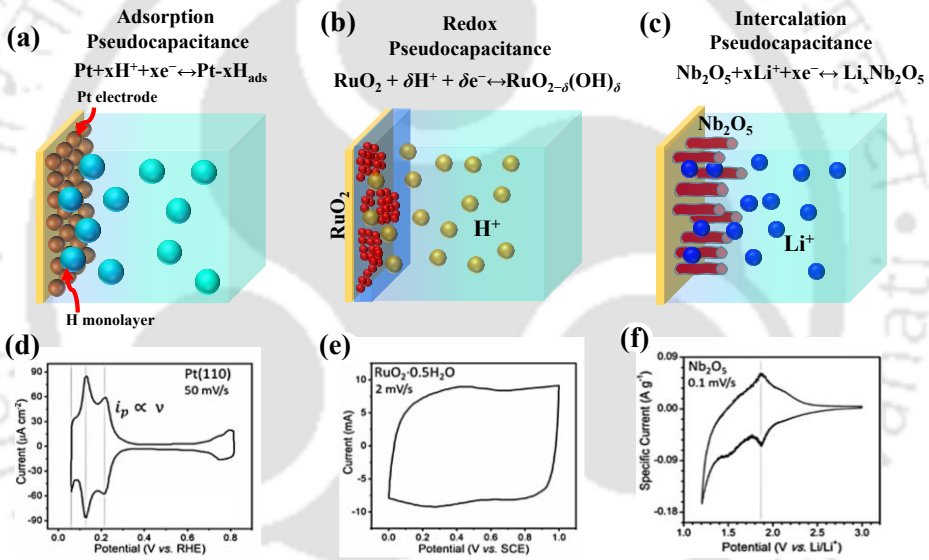

Figure 1.4: Three types of mechanisms that give rise to pseudocapacitance as defined by Conway (a) Adsorption pseudocapacitance, (b) redox pseudocapacitance, and (c) intercalation pseudocapacitance. and (d–f) their corresponding cyclic voltammograms. Adapted from ref. [42,46]

Pseudocapacitor electrode materials store energy through fast, reversible Faradaic (redox) reactions at the electrode surface, unlike electric double-layer capacitance, which relies mainly on electrostatic charge separation. The term "pseudo" refers to identifying electrode materials whose electrochemical behaviour is capacitive, but charge storage occurs by charge-transfer Faradaic reactions that take place on the surface or near-surface of the electrode materials. It is an intermediate electrochemical behavior between electrostatic EDLCs and diffusion

dominated by Faradaic reactions in battery-type materials.[41,42] These faradaic processes involve charge transfer between the electrode and electrolyte ions, often through mechanisms such as redox reactions, intercalation, or adsorption. Pseudocapacitive materials, such as transition metal oxides (RuO_2)[43], conducting polymers (PANI)[44], and some 2D materials (like MXenes and LDHs)[45], exhibit high specific capacitance due to their ability to store charge across multiple oxidation states. The combination of pseudocapacitance and double-layer capacitance enhances the overall performance of supercapacitors, offering higher energy density than traditional capacitors while maintaining rapid charge-discharge capabilities.

a) **Adsorption pseudocapacitance**: Reversible pseudocapacitance occurs when electrochemical species get adsorbed over the electrode surface. Examples of such processes include adsorption of H on the Pt surface or O and OH over the surface of nickel oxides.[47]

b) **Redox pseudocapacitance**: Here, the adsorbed species from the electrolyte get involved in reversible faradaic reactions. For example, adsorption and faradaic reaction of H^+ ions over $Ti_3C_2T_x$ MXene surface, redox reaction of RuO_2 in hydrous electrolyte.[48][43]

c) **Intercalation pseudocapacitance:** In this case, the electrochemical ions get intercalated into the pores and channels, followed by a Faradic reaction. Unlike a battery, no phase change occurs in the active material. The intercalation of Li^+ ions into Nb_2O_5 is an example of such intercalation-type pseudocapacitance.[49]

1.2.3. Asymmetric Supercapacitors:

A "hybrid capacitor" or "asymmetric supercapacitor" refers to a device, not electrodes; rather, it is a supercapacitor device where the two electrodes employ different charge storage mechanisms: capacitive and pseudocapacitive, and it offers a broader operational range. These devices combine two distinct electrode materials, where the active materials may exhibit different charge storage mechanisms or varying ratios of redox-active sites. They may also use different redox-active electrolytes or employ the same EDLC carbon material with differing surface functional groups.[50,51]Hybrid devices are a specific subset of asymmetric devices. A common example of a hybrid capacitor is a device with one Faradaic electrode (e.g., $Ni(OH)_2$ or Co_3O_4) paired with a carbon-based electrode.

1.3. EMERGENCE OF 2D MATERIALS IN SUPERCAPACITORS:

Supercapacitor performance largely depends on the electrochemical properties of the electrode materials, such as electrical conductivity, accessible active sites, and efficient ionic transport within the electrolyte that directly affect the cell voltage, energy and power output.[52,53] Nanostructured materials offer additional advantages, including high surface areas that provide numerous active sites for electrochemical reactions, short ionic diffusion paths, and fast chemical kinetics.[54] The emergence of 2D materials in the supercapacitor field has revolutionized energy storage by addressing the limitations of traditional materials. With atomic-scale thickness, high surface area, and tunable electronic properties, 2D materials are highly versatile contenders for advanced energy storage applications.[55–57]

Graphene, a fascinating 2D material, has shown incredible potential due to its unique hexagonal lattice made up of sp^2 hybridized carbon atoms.[58,59] Its impressive charge storage capabilities come from its ultra-high surface area and minimal ohmic losses, which contribute to its excellent electrical conductivity in energy devices. However, there are challenges to overcome, such as the restacking of graphene sheets and the hurdles of large-scale production, which have sparked interest in exploring alternative 2D materials. Beyond graphene, a variety of materials like MXenes[60], transition metal dichalcogenides (TMDs)[61], layered double hydroxides (LDHs)[62], as well as borophene[63], phosphorene[64], black phosphorus,[65] and hexagonal boron nitride (h-BN)[66,67], etc., are emerging as promising candidates for electrode materials. For example, MXenes are not only metallic and conductive but also hydrophilic, making them particularly well-suited for applications in pseudocapacitance. Similarly, LDHs are notable for their adjustable compositions and strong pseudocapacitive properties, while Xenes'(such as Borophene, phosphorene) exceptional characteristics, including high conductivity and flexibility, present innovative possibilities for energy storage solutions. The advent of 2D materials has also paved the way for new designs in hybrid and composite electrodes. By combining different 2D materials or integrating them with non-2D materials (i.e., 0D, 1D,3D), it is possible to develop electrodes that benefit from the synergistic properties of multiple components. This strategy can effectively mitigate these issues, and improve ion transport, as well as using surface area as effectively as possible. In this thesis, various types of 2D electrode materials have been explored and subjected to different modification strategies, as discussed in the sections below.

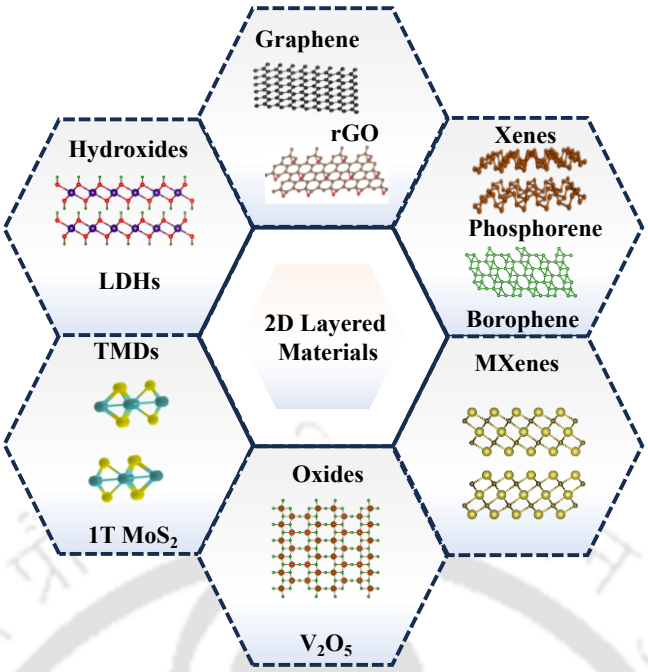

Figure 1.5: Several types of two-dimensional-layered materials that have been widely studied recently for supercapacitor applications.

1.3.1. Layered oxyhydroxide:

Layered double hydroxides (LDHs) are a notable class of 2D layered materials categorized under hydrotalcite-like (HT) compounds, also known as anionic clays. The structure of LDHs consists of charged brucite-like layers formed by divalent metal ions (M^{2+}, such as Ca^{2+}, Zn^{2+}, Mg^{2+}, Ni^{2+}) that are octahedrally coordinated with six hydroxyl (OH^-) groups. A portion of the divalent cations (M^{2+}) is replaced by trivalent metal ions (M^{3+}, such as Al^{3+}, Fe^{3+}, Cr^{3+}, In^{3+}), creating positively charged layers. To maintain overall electroneutrality, these layers are intercalated with exchangeable anions (A^{n-}, such as hydroxyl groups, nitrates, carbonates, or sulphates) along with water molecules. The general chemical formula of LDHs is $[M_{1-x}^{2+}M_x^{3+}(OH)_2]A_{x/n}^{n-}.mH_2O$ where $M^{2+}$and M^{3+} represent divalent and trivalent metal ions, A^{n-} refers to inorganic or organic anions, m is the number of water molecules, and $x = M^{3+}/(M^{2+}+M^{3+})$ defines the layer charge density or molar ratio.[62] For example, the electrochemical properties of NiAl-LDHs have been reported as early as 2007, where a redox peak was observed in the cyclic voltammetry (CV) curves, which can be represented by the following reaction:[68]

$$\mathbf{Ni(II)(OH)_2 + OH_{sol}^- \leftrightarrow Ni(III)OOH + H_2O + e^-}$$

LDH follows a pseudocapacitive charge storage mechanism that results from a combined mechanism that includes "electron hopping" within layers of LDH and proton migration from hydroxyl-bound M^{2+} sites to the electrolyte, a process facilitated by the faradaic redox reactions of the metal cations, given by the following equation.

$$\mathbf{M^{3+} + e^- \leftrightarrow M^{2+}}$$

Where M represents a redox-active metal ion such as Ni, Co, or Fe.

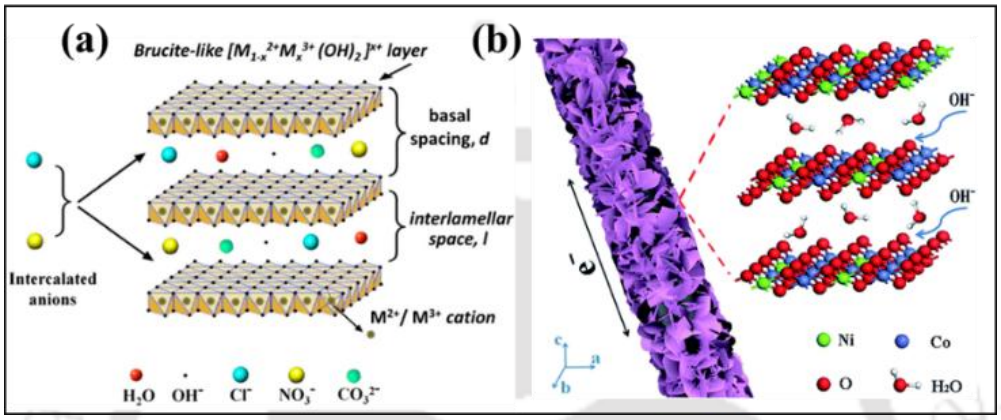

Figure 1.6: (a) The idealized structure of LDHs with different M^{2+}/M^{3+} molar ratios and different intercalated ions (b) Illustration of the electrochemical processes for NiCo-LDH/CNFs showing diffusion of OH^-, Adapted from ref. [67,69]

The intercalated anions (such as NO_3^-, CO_3^{2-}, SO_4^{2-}) and water molecules present in the interlayer spaces play a crucial role in the charge storage mechanism by engaging in ion exchange during electrochemical cycling. This process facilitates the efficient movement of ions (like OH^-) from the electrolyte, helping to maintain charge neutrality throughout the redox reactions as illustrated in **Figure 1.6b**. Besides faradaic reactions, LDHs also demonstrate a certain level of double-layer capacitance, which arises from the adsorption of electrolyte ions on their extensive surface area. However, this contribution is generally less pronounced when compared to the pseudocapacitive effects.

1.3.2. Graphene:

Graphene, a 2D material with a hexagonal lattice of sp^2 hybridized carbon atoms, exhibits exceptional physical and chemical properties, including high intrinsic carrier mobility (200,000 $cm^2V^{-1}s^{-1}$), high thermal conductivity (5000 $Wm^{-1}K$, ten times better than copper), high optical transmittance (97.7%), high Young's modulus (1.0TPa), high tensile strength, excellent flexibility, and an extremely high specific surface area (theoretically 2630 m^2g^{-1}). These

characteristics make graphene highly promising for a wide range of applications, particularly in energy storage.[70–72] Its unique atomic structure provides a significant surface area, crucial for superior EDLC performance, while its delocalized π electrons offer excellent electronic conductivity, reducing ohmic losses in supercapacitive devices. The success of graphene has prompted extensive research into other carbon-based materials such as carbon dots (0D), carbon nanotubes (CNTs, 1D)[73], and porous activated carbons (3D), all of which have shown considerable potential in energy storage applications.[74]

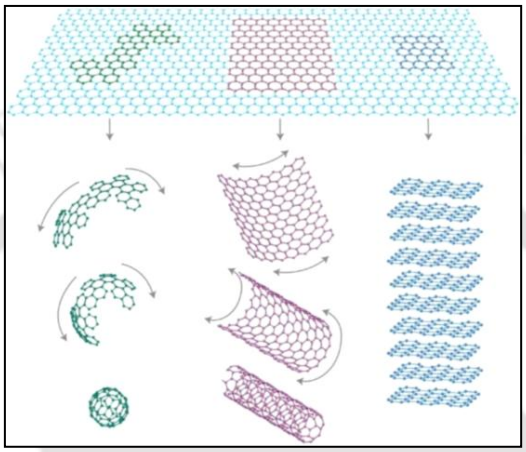

Figure 1.7: Graphene is a 2D building material. It can be piled to create 3D graphite, rolled into 1D nanotubes, or wrapped into 0D buckyballs. Adapted from ref.[71]

The practical application of Graphene is often limited by difficulty in large-scale production and agglomeration, leading to the development of graphene oxide (GO), which is a more practical and versatile material. GO is commonly synthesized via Hummer's method, and is further chemically reduced to form rGO, which has an improved conductivity and enables scalable production of macrostructures.[75] For example, Li et al. demonstrated rGO film electrodes via vacuum filtration of chemically reduced graphene. These rGO-based structures combine enhanced conductivity and mechanical stability, making them promising for scalable and cost-effective energy storage applications.[76]

1.3.3. Xenes:

The discovery of graphene and its remarkable properties have revolutionized energy materials, enabling their application in supercapacitors and batteries. This progress has expanded the research and development of graphene-like materials from group 13-16 of the periodic table beyond carbon-based materials. After the discovery of silicene, there is a race of development of 'Xene systems, where "X" refers to different elements. These include

borophene, aluminene, gallenene, and thallene (group 13); silicene, germanene, and stanene (group 14); phosphorene, arsenene, and antimonene (group 15); and sulfurene, selenene, and tellurene (group 16), offering vast potential for next-generation energy technologies.[77] Their maximum surface-to-bulk ratio provides abundant active sites for electrochemical charge storage. With layered structures and superior ion accommodation capabilities, they enhance energy storage through a combination of electrostatic double-layer capacitance and redox capacitance at defects, edges, and basal planes, collectively improving pseudocapacitance.

1.3.4. MXenes:

MXenes are pseudocapacitive materials, garnering significant attention in energy storage research. First introduced by Gogotsi et al. in 2011, MXenes uniquely combine metallic conductivity with pseudocapacitance and hydrophilicity.[78]These exceptional physicochemical properties have driven extensive research into their potential for various applications, including energy storage, sensing, electromagnetic interference shielding, solar water evaporation, and catalysis. To date, over 150 types of MXene materials have been predicted, with new variants continuously being discovered.

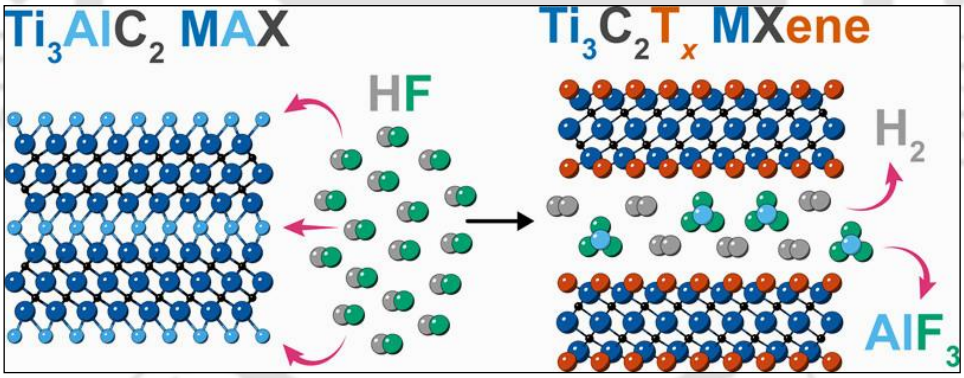

Figure 1.8: Schematic of the Ti_3AlC_2 MAX etching reaction using hydrofluoric acid, which produces hydrogen gas and aluminium fluoride. Adapted from ref.[79]

MXenes are synthesized from MAX phase materials, which are represented by the general formula $M_{n+1}AX_n$, where M stands for transition metals, A refers to group IIIA or IVA elements, X represents carbon and/or nitrogen, and n ranges from 1 to 3. The process of obtaining MXenes involves selectively removing the A atoms from the MAX phase using chemical etching techniques. Most 2D materials, like graphene, are stacked in bulk structures via van der Waals forces, enabling simple delamination. In contrast, MXenes, derived from MAX phase materials ($M_{n+1}AX_n$), have strong metallic M-A bonds, making etching more challenging. Chemical etching targets these weaker M-A bonds.[80] Naguib and Gogotsi

pioneered MXene synthesis by etching Ti_3AlC_2 with hydrofluoric acid (HF), producing $Ti_3C_2T_x$ MXene with functional groups (–OH, –Cl, –F, –O) on the basal plane. The reaction involves:[79]

$$Ti_3AlC_2 + 3HF \rightarrow Ti_3C_2 + AlF_3 + \frac{3}{2}H_2$$

$$Ti_3C_2 + 2H_2O \rightarrow Ti_3C_2(OH)_2 + H_2$$

$$Ti_3C_2 + 2HF \rightarrow Ti_3C_2F_2 + H_2$$

Post-etching delamination uses methods like ultrasonication and cation intercalation to produce few-layer MXene flakes. HF-based etching is now often replaced by safer, efficient in-situ HF methods using hydrochloric acid (HCl) and fluoride salts (LiF), introduced by Ghidiu et al. This "MILD" method enhances yield, reduces defects, and achieves delamination with minimal effort, such as handshaking.[81]

1.3.5. Transition metal Oxides:

Transition metal oxides (TMOs), such as MnO_2,[82] V_2O_5,[83] RuO_2,[84] NiO,[85] etc. are highly promising for supercapacitor electrodes due to their inherently rich redox activity and large surface areas, which provide ample sites for electrochemical double-layer charge storage. Additionally, their thin and flexible forms, coupled with excellent mechanical and chemical stability, make them suitable for integration into next-generation flexible devices. RuO_2 is a highly attractive metal oxide for supercapacitor electrodes due to its excellent metallic conductivity, reversible redox reactions, and remarkable thermal, chemical, and catalytic stability in both amorphous and crystalline forms. However, its high cost confines its extensive use, and alternative oxides such as MnO_2 and V_2O_5 are often utilized for supercapacitors. Both manganese ($Mn^{2+/3+/4+}$) and vanadium($V^{4+/5+}$) exhibit multiple oxidation states, enabling efficient charge storage on their surfaces.

1.3.6. Transition metal dichalcogenides:

2D TMDs are made of layered materials, where a transition metal (M) layer is sandwiched between two chalcogen (X) layers, following the formula MX_2 (with M being Mo, W, V and X being S, Se, or Te). [86]These materials boast a large surface area and varying oxidation states, allowing for both electrical double-layer capacitance and fast, reversible Faradic charge storage. The electrochemical performance of 2D TMDs is often hindered by their susceptibility to oxidation, which limits cycle life, as well as inherent low conductivity, significant volume changes, and a tendency to restack. For instance, the sheet-like morphology of MoS_2 proposed

by Soon et al. offered a large surface area for double-layer charge storage. However, due to its poor electrical conductivity, it displayed a relatively low specific capacitance of approximately 100 F g^{-1} at a scan rate of 1 mV s^{-1}.[87]To overcome the challenges of 2D TMDs, they are combined with conductive materials like carbon and conducting polymers through various synthetic approaches which enhances conductivity and interfacial contact, while TMDs provide short ion diffusion and electron transport paths.[88] Together, they significantly improve electrochemical performance, making them promising for advanced energy storage applications.

1.4. CHALLENGES AND STRATEGIES FOR 2D ELECTRODE MATERIAL:

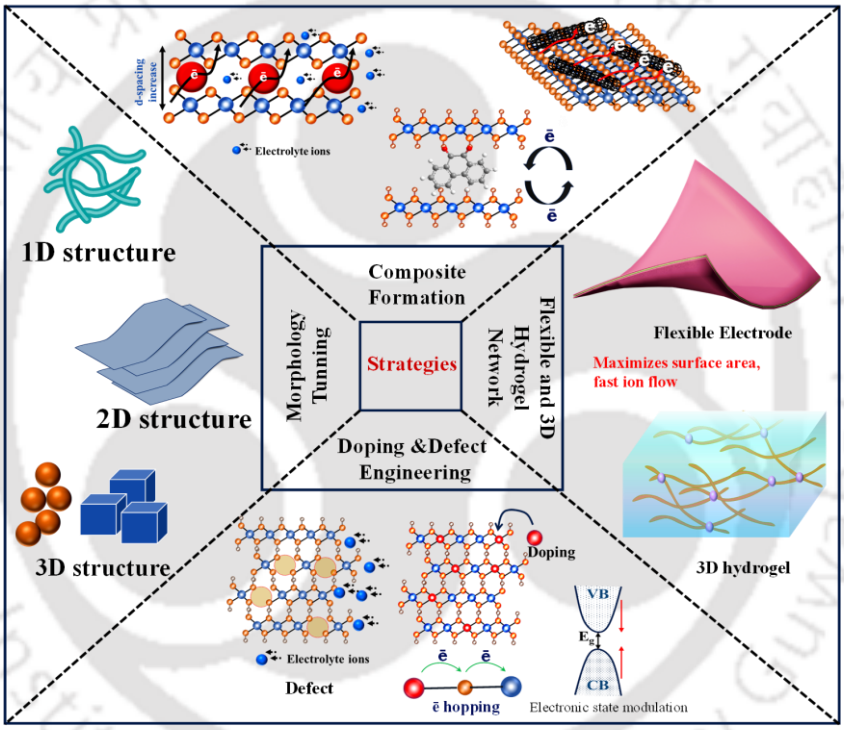

2.

3. **Figure 1.9**: Schematic illustration of several active approaches to improve charge storage properties of 2D electrode materials.

However, the properties that make 2D materials attractive as electrode materials in energy storage applications are accompanied by several drawbacks that limit its performance, which need to be resolved via modification. Restacking and aggregation of 2D layers based on van der Waals interactions lead to shrinking surface area and ion diffusion pathways, hindering charge storage and slowing charge-discharge rate. Again, the presence of high defect density, particularly in transition metal dichalcogenides (TMDs) impedes the electronic properties that are critical for energy storage. Furthermore, the scalability issues present themselves with techniques like chemical vapor deposition (CVD) and liquid phase exfoliation being unable to

reach commercialization at their current manufacturing processes. Adding to the further complication of the use of 2D materials, black phosphorus and some dichalcogenides are vulnerable to oxidation, degradation, and/or phase transformation under natural conditions or under cycling. Furthermore, achieving highly conductive and electrochemically useful properties is challenging when graphene has great conductive but low capacitance, or transition metal dichalcogenides (TMDs) have good pseudocapacitance but low conductivity. Integrating this material for electrode architectures retaining its mechanical, structural stability with high energy density and a cost-effective synthesis technique remains challenging. These related issues must be addressed through modification by defect engineering, scalable fabrication techniques, stability enhancement strategies to prevent restacking, porous structure creation, optimized doping methods, interface improvement, and cost-efficient systems to realize the full potential of 2D materials in energy storage.

3.2.1. Composite formation:

Energy storage performance in 2D materials is often limited by restacking, which decreases the ion-accessible surface area and hinders ion movement and charge storage. To address this, guest species can be introduced into exfoliated 2D sheets, increasing interlayer spacing and active sites while reducing restacking, thereby improving ion transport and cycling stability. In some cases, the 2D material itself serves as a conductive support for the growth of host materials, creating efficient pathways for charge transfer, enhancing mechanical stability, lowering internal resistance, and improving power delivery.[89–91] Building on these approaches, hybridization strategies, such as intercalation of other species, such as metal ions, conducting polymers, organic species, or making composite materials with nanotubes, nanoparticles, or different 2D materials, lead to an increased interlayer distance, thereby increasing the active site for charge storage.[92]

Graphene-based hybrids (e.g., graphene/NiO,[93] graphene/MnO_2,[94] graphene/LDH[95]) and conductive polymer (CP)-TMD composites also show enhanced performance. Ren et al. reported MoS_2/PANI hybrids with a specific capacitance of 552 F g^{-1} at 0.5 A g^{-1}, attributed to the 3D structure facilitating ion access for enhanced energy storage.[96] Similarly, MXenes suffer from restacking, which can be mitigated by incorporating polymers, carbon derivatives, or metal oxides as interlayer spacers. Many MXene-based hybrids, such as MnO_2/MXene,[97] MXene/MoS_2,[98] MXene/BCN,[99] and MXene/BN/NiCo-MOF[100] composites have been reported to exhibit enhanced energy storage performance.

3.2.2. Flexible electrode and 3D hydrogel network:

Supercapacitors that bend and stretch are made possible by the use of 2D materials on flexible substrates or free-standing, which is essential for wearable and portable applications. High capacitance and mechanical stability are maintained under deformation using textile-based 2D electrodes, such as graphene,[101] V_2O_5,[102] MXene,[103] etc., with heterostructure coatings on fabric or free-standing electrodes. For example, Zhao et al. proposed an interlayer hydrogen-bonded MXene/metal-porphyrin frameworks (MPFs) free-standing film electrode.[104] The resulting structure improves ionic and electronic transport rates by alternating MXene and MPFs to construct a 3D interconnected "MPFs-to-MXene-to-MPFs" network. Strong chemical stability is provided by interlayer hydrogen bonds (F···H–O and O···H–O), which enable the material to withstand volume change and prevent structural collapse during repeated cycles of charge and discharge, shown in **Figure1.10**.

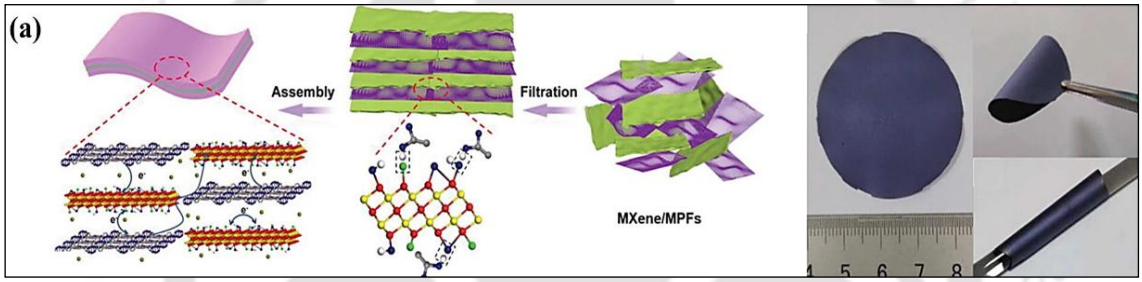

Figure 1.10: (a) Synthetic route to interlayer hydrogen-bonded MXene/MPFs films (left) and digital images of flexible and free-standing MXene/MPFs films (right). Adapted from ref.[104]

In order to balance electron/ion transport and volumetric performance, 2D nanosheets are assembled into 3D structures (aerogels, macroporous frameworks, hydrogels) to improve packing density and porosity. These networked structures provide efficient ion pathways and confine active materials to improve energy density, rate capability, and cycling stability. Examples include graphene oxide hydrogels,[105,106] MXene hydrogels [96] and other hybrid hydrogel architectures. These electrodes mostly provide mechanical robustness for practical energy storage applications.

3.2.3. Doping and Defect Engineering:

Doping has been demonstrated to be an effective strategy for tailoring physicochemical features of 2D materials. Incorporation of foreign atoms into a 2D lattice serves different functions such as: (1) Heteroatom doping can form multi-component 2D materials to adjust metal valence ratio in case of oxides and LDH (2) regulate and increase active metal sites (3)

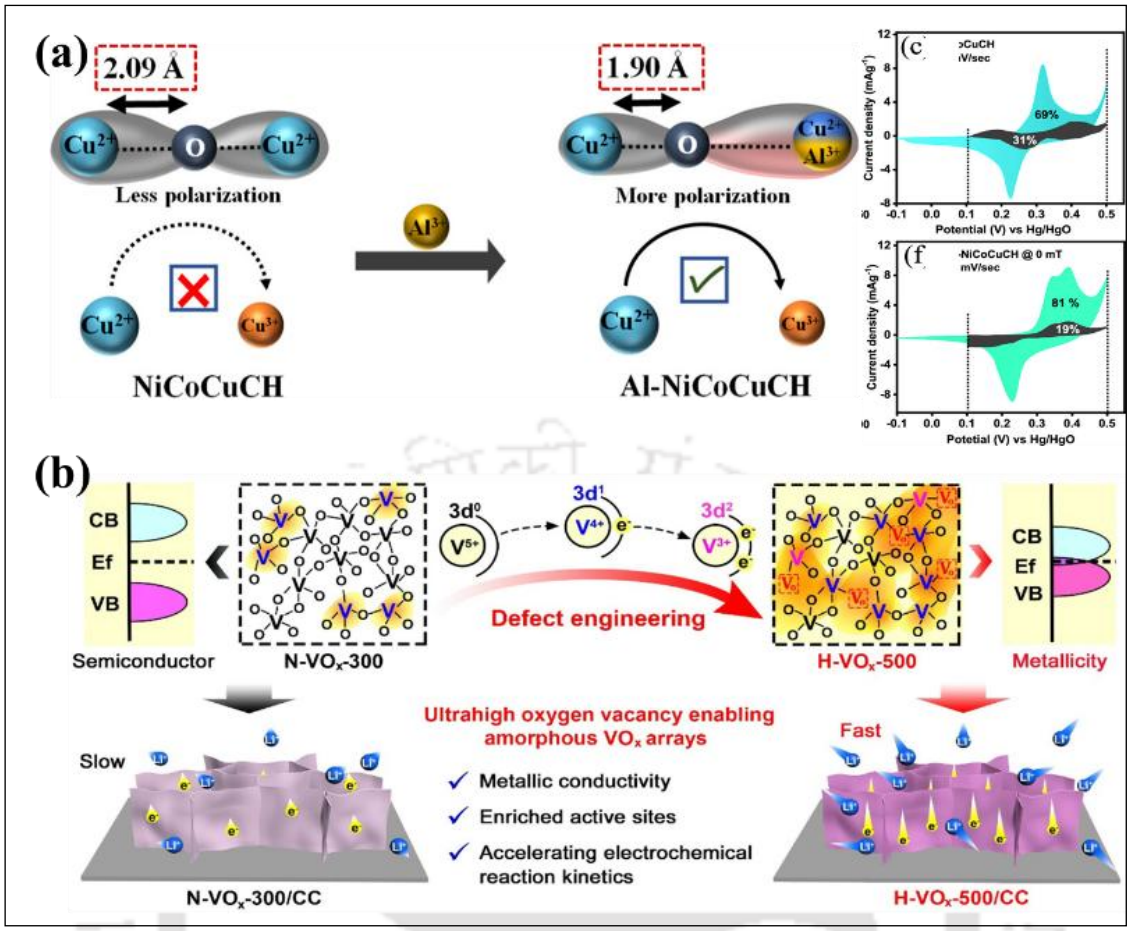

Figure 1.11:(a) Mechanistic aspects of Al^{3+} doping at the Cu^{2+} lattice site in NiCoCuCH, shortening the Cu–O bond to facilitate easy formation of the Cu^{2+}/Cu^{3+} redox pair, aiding the electrochemical performance, Adapted from ref.[110] (b) Schematic diagram for the regulation of the V 3d band edge with high electrical conductivity by defect engineering and the electrochemical advantages of the as-formed metallic amorphous VO_x nanosheet arrays Adapted from ref.[113]

tune electronic states to improve conductivity, and (4) increase interlayer spacing to reduce the restacking.[107–109] We can either dope cation or anion doping for tuning the electronic structure and chemical characteristics of the material. Pandey *et al.* reported Al^{3+} doped NiCoCu carbonate Hydroxide (NiCoCuCH), where Al^{3+} replaced Cu, which has a higher polarization power. The doping of aluminum, in the copper site, resulted in electrons shifting toward the Al–O bond as Al has higher polarization power, thereby creating electron-deficient Cu in the species. This electron-deficient copper encouraged the easy oxidation of Cu^{2+} to Cu^{3+}, which in turn enhanced the diffusion contribution toward pseudocapacitance, shown in **Figure 1.11a**.[110] Similarly, the anion doping (e.g., F^-, Cl^-, Br^-, SO_4^{2-}, etc.) is also beneficial to enhance intrinsic conductivity, thus effectively increasing the electrochemical performance.

Yue et al. discovered that the synthesis of β-FeOOH nanorods is significantly influenced by the incorporation of various anions. These anions interact with the FeO_6 octahedral unit in β-FeOOH, leading to variations in the crystalline structure and morphology of the nanoparticles, even under the same conditions, which is helpful to increase the charge storage.[111]

On the other hand, vacancy engineering refers to the deliberate creation of atomic defects, such as missing oxygen or metal atoms within the material structure. These vacancies act as extra active centres for ion adsorption and redox reactions, thereby boosting capacitance and facilitating rapid ion transport. For example, Sanjit et al. reported an F-doped h-BN/rGO composite, where F doping in h-BN induced defects and disorder, thereby facilitating ion diffusion and enhancing redox charge transfer, which contributed to improved charge storage from the interior sites of the electrode material.[112]Similarly, Chain et.al reported amorphous vanadium oxide nanosheet arrays with metallicity through defect engineering, achieving a high oxygen vacancy, and DOS calculations reveal the absence of a band gap, and the oxygen vacancies lower the ion migration energy barrier, enhancing electrochemical performance. shown in **Figure 1.11b.** [113]

3.2.4. Morphology tuning:

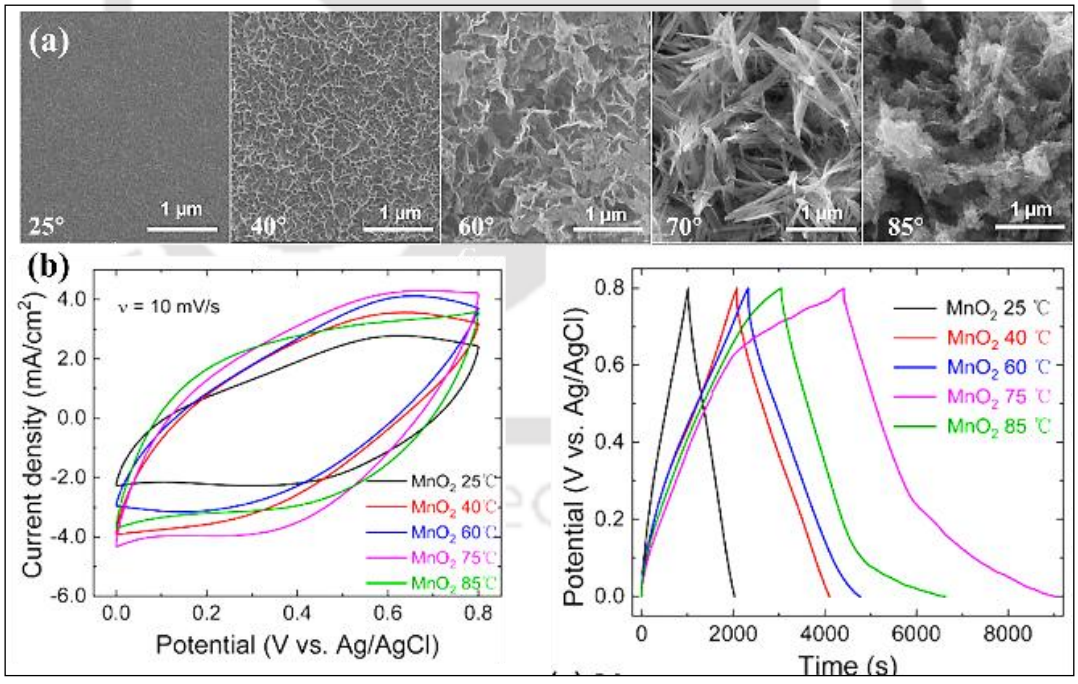

Figure 1.12: (a) MnO_2 synthesized via electrodeposition with time variation showing different morphology and (b) corresponding electrochemical behaviour, Adapted from ref.[116]

Charges are stored on the surface of the supercapacitor electrodes; an electrode with a higher surface area leads to an improved specific capacitance. Nano structuring of electrode materials

is an achievable method to considerably improve the surface area of the electrodes, which enables efficient electrolyte infiltration, while the reduced particle dimensions shorten ion transport and diffusion paths, thereby promoting faster kinetics and high charge–discharge rates.[54] Generally, 2D layered metal oxide and LDH always do not always have a sheet-like structure, so they need structural modification, either using structure structure-directing agent or doing optimization, which can modify into different morphologies owing to high surface area and is useful to increase the charge storage. One-dimensional (1D) nanostructures improve the flow of electrons by making it easier for them to move directly from one place to another. Large specific surface area allows the electrolyte to enter and generate a large number of accessible active sites, which increases catalytic activity. Nanobelts, nanowires, nanofibers, nanorods, nanotubes, and so on are common 1D nanostructures.[114] Two-dimensional (2D) nanostructured materials have a higher theoretical specific surface area than one-dimensional (1D) materials, which allows for surface property modification.[92] The change in chemical, physical, and electrical properties of 2D nanostructures is largely dependent on their lateral dimension and thickness. The most likely two-dimensional forms are nanoplates and nanosheets, which also improve electrolyte-electrode interaction.[115]

Similarly, 3D nanostructures have the advantage of morphological versatility based on their synthesis methods and offer control over facet-oriented crystallization. For instance, Liu et al. synthesized MnO_2 on an Au–Ni substrate using an electrodeposition technique. By varying the temperature while keeping the electrodeposition time fixed at 900 s, they obtained MnO_2 with different morphologies, each exhibiting a distinct specific capacitance as shown in **Figure 1.12**.[115]

3.3. MOTIVATION AND OBJECTIVES OF THE PRESENT WORK

The development of high-performance energy storage resolution demanded tremendous research on supercapacitors having ultrafast charge and discharge capability, long cyclic life, and high-power density. Nevertheless, the stability problem of using traditional electrode materials, e.g. activated carbon and metal oxides, and low conductivity have become the major obstacles to the development of EESs. Beyond these material limitations, supercapacitors still face challenges in achieving high energy density while maintaining excellent power capability and cycling stability. The performance of supercapacitors is primarily governed by the choice of electrode materials, where factors such as conductivity, surface area, electrochemical stability, and cost play a crucial role.

In this regard, the emergence of 2D materials such as graphene and MXenes LDHs provides great promise for next-generation supercapacitor electrodes because these materials offer a very high surface area, tunable electronic properties, and possible surface functionalization. As such, advancements in supercapacitor technology rely on the development of 2D materials with better electrochemical properties. However, there have been many studies regarding 2D materials, yet these problems remain, like the optimization of charge storage mechanism, enhancement of long-term stability, as well as having as much loading into the capacitance without destroying the structure. Such challenges can lead to next-generation high-performance supercapacitors with better energy storage efficiency.

Thus, the prime objectives of the present thesis work are as follows:

[1] **Selection of 2D Materials for Supercapacitor Electrodes:** Explore and utilize 2D materials that exhibit high stability and electrical conductivity to improve charge storage efficiency.

[2] **Doping of Foreign Elements to Enhance Electrochemical Performance**: Introduce heteroatom doping (e.g., B, O, N, S) into the lattice of 2D materials to improve conductivity, charge mobility, and electroactivity.

[3] **Incorporation of Electroactive Materials for Enhanced Charge Storage**: Hybridize 2D materials with electroactive species (e.g., metal oxides, conductive polymers, or nanoparticles) to improve redox activity and energy storage capacity.

[4] **Optimization of Morphological Features for Enhanced Surface Area:** Engineer the structure of 2D materials to increase porosity, interlayer spacing, and surface-active sites for better ion diffusion and charge accumulation.

[5] **Development of Composite Electrode Materials to Synergize Properties:** Design and fabricate composite electrodes combining different 2D materials to leverage their strengths and suppress limitations.

[6] **Fabrication of Freestanding Electrodes:** Synthesize and fabricate binder-free, flexible electrodes to assess their practical application in high-performance supercapacitors.

1.6. REFERENCES:

1. Enerdata, *GLOBAL ENERGY TRENDS Continued Growth in Energy Consumption and Emissions*, **2024**.
2. H. Chen, T. N. Cong, W. Yang, C. Tan, Y. Li, Y. Ding, *Progress in Nat. Sci.* **2009**, *19*, 291.
3. W. Strielkowski, L. Civín, E. Tarkhanova, M. Tvaronavičienė, Y. Petrenko, *Energies* **2021**, *14*, 8240.
4. A. Z. AL Shaqsi, K. Sopian, A. Al-Hinai, *Energy Reports* **2020**, *6*, 288.
5. M. Amir, R. G. Deshmukh, H. M. Khalid, Z. Said, A. Raza, S. M. Muyeen, A.-S. Nizami, R. M. Elavarasan, R. Saidur, K. Sopian, *J Energy Storage* **2023**, *72*, 108694.
6. Economic considerations on the demand-side of electricity markets in a context of energy transition. Economics and Finance. *Université Paris sciences et letters*, **2023**. English. NNT: 2023UPSLM054.
7. J. R. Miller, P. Simon, *Science* **2008**, *321*, 651.
8. N. S. Wade, P. C. Taylor, P. D. Lang, P. R. Jones, *Energy Policy* **2010**, *38*, 7180.
9. A. Aghmadi, O. A. Mohammed, *Batteries* **2024**, *10*, 141.
10. Z. Fang, J. K. H. Shek, W. Sun, *J Energy Storage* **2025**, *118*, 116226.
11. J. Zhang, M. Gu, X. Chen, *Micro and Nano Engineering* **2023**, *21*, 100229.
12. A. Burke, *J Power Sources* **2000**, *91*, 37.
13. J.-M. Tarascon, M. Armand, *Nature* **2001**, *414*, 359.
14. R. F. Service, *Science* **2006**, *313*, 902.
15. B. K. Kim, S. Sy, A. Yu, J. Zhang, in *Handbook of Clean Energy Systems*, Wiley, **2015**,1. DOI:1002/9781118991978.hces146
16. A. M. Saleh, I. Vokony, M. Waseem, M. A. Khan, A. Al-Areqi, *Energy Reports* **2025**, *13*, 2637.
17. A. Lahyani, P. Venet, A. Guermazi, A. Troudi, *IEEE. Trans Power Electron.* **2013**, *28*, 1509.
18. N. Kularatna, K. Subasinghage, K. Gunawardane, D. Jayananda, T. Ariyarathna, *Electronics* **2021**, *10*, 1697.
19. K. V. G. Raghavendra, R. Vinoth, K. Zeb, C. V. V. Muralee Gopi, S. Sambasivam, M. R. Kummara, I. M. Obaidat, H. J. Kim, *J Energy Storage* **2020**, *31*, 101652.
20. D. Iannuzzi, F. Ciccarelli, D. Lauria, *Transp. Res. Part C Emerg. Technol.* **2012**, *21*, 321.
21. X. Zhang, Z. Zhang, H. Pan, W. Salman, Y. Yuan, Y. Liu, *Energy Convers Manag* **2016**, *118*, 287.
22. I. Ushiyama, *Renew Energy* **1999**, *16*, 1174.
23. M. Winter, R. J. Brodd, *Chem Rev* **2004**, *104*, 4245.
24. D. Larcher, J.-M. Tarascon, *Nat Chem* **2015**, *7*, 19.
25. A. Noori, M. F. El-Kady, M. S. Rahmanifar, R. B. Kaner, M. F. Mousavi, *Chem Soc Rev* **2019**, *48*, 1272.
26. P. Simon, Y. Gogotsi, *Nat Mater* **2008**, *7*, 845.
27. Y. Gogotsi, P. Simon, *Science* **2011**, *334*, 917.

28. M. Tomy, A. Ambika Rajappan, V. VM, X. Thankappan Suryabai, *Energy & Fuels* **2021**, *35*, 19881.
29. M. Ali, A. M. Afzal, M. W. Iqbal, S. Mumtaz, M. Imran, F. Ashraf, A. Ur Rehman, F. Muhammad, *Int J Energy Res* **2022**, *46*, 22336.
30. S. Sagadevan, A. R. Marlinda, Z. Z. Chowdhury, Y. B. A. Wahab, N. A. Hamizi, M. M. Shahid, F. Mohammad, J. Podder, M. R. Johan, in *Advances in Supercapacitor and Supercapattery*, Elsevier, **2021**,27. DOI:10.1016/B978-0-12-819897-1.00001-X.
31. J. M. Lim, Y. S. Jang, H. Van T. Nguyen, J. S. Kim, Y. Yoon, B. J. Park, D. H. Seo, K.-K. Lee, Z. Han, K. (Ken) Ostrikov, S. G. Doo, *Nanoscale Adv.* **2023**, *5*, 615.
32. J. Huang, B. G. Sumpter, V. Meunier, *Chemistry – A European Journal* **2008**, *14*, 6614.
33. C. Largeot, C. Portet, J. Chmiola, P.-L. Taberna, Y. Gogotsi, P. Simon, *J. Am. Chem. Soc.* **2008**, *130*, 2730.
34. M. G. Ashritha, K. Hareesh, *Smart Supercapacitors*, Elsevier, **2023**, 179. **ISBN:**978-0-323-90530-5.
35. L. Miao, Z. Song, D. Zhu, L. Li, L. Gan, M. Liu, *Mater Adv.* **2020**, *1*, 945.
36. L. L. Zhang, X. S. Zhao, *Chem Soc Rev* **2009**, *38*, 2520.
37. V. D. Ivanov, *J. of Solid-State Electrochemistry* **2024**, *28*, 2487.
38. H. Wang, L. Pilon, *The Journal of Physical Chemistry C* **2011**, *115*, 16711.
39. M. Gouy, *Journal de Physique Théorique et Appliquée* **1910**, *9*, 457.
40. Y. Jiang, J. Liu, *Energy & Environmental Materials* **2019**, *2*, 30.
41. S. Fleischmann, J. B. Mitchell, R. Wang, C. Zhan, D. Jiang, V. Presser, V. Augustyn, *Chem Rev* **2020**, *120*, 6738.
42. S. Ardizzone, G. Fregonara, S. Trasatti, *Electrochim. Acta* **1990**, *35*, 263.
43. D. Cevher, A. Cirpan, *J Energy Storage* **2025**, *109*, 115246.
44. M. Hu, H. Zhang, T. Hu, B. Fan, X. Wang, Z. Li, *Chem Soc Rev* **2020**, *49*, 6666.
45. V. Augustyn, P. Simon, B. Dunn, *Energy Environ Sci* **2014**, *7*, 1597.
46. B. E. Conway, E. Gileadi, *Transactions of the Faraday Society* **1962**, *58*, 2493.
47. S. B. Ambade, R. B. Ambade, W. Eom, S. H. Noh, S. H. Kim, T. H. Han, *Adv Mater Interfaces* **2018**, *5*, 1801361.
48. B. E. Conway, *Electrochim Acta* **1993**, *38*, 1249.
49. A. Muzaffar, M. B. Ahamed, K. Deshmukh, J. Thirumalai, *Renewable and Sustainable Energy Reviews* **2019**, *101*, 123.
50. K. Sun, Z. Zhang, H. Peng, G. Zhao, G. Ma, Z. Lei, *Mater Chem Phys* **2018**, *218*, 229.
51. Reenu, Sonia, L. Phor, A. Kumar, S. Chahal, *J Energy Storage* **2024**, *84*, 110698.
52. L. Hao, X. Li, L. Zhi, *Advanced Materials* **2013**, *25*, 3899.
53. S. Chen, W. Xing, J. Duan, X. Hu, S. Z. Qiao, *J. Mater. Chem. A* **2013**, *1*, 2941.
54. A. Philip, A. Ruban Kumar, *Renewable and Sustainable Energy Reviews* **2023**, *182*, 113423.
55. X. Chia, M. Pumera, *Nat Catal* **2018**, *1*, 909.
56. A. Kumar, C.-Y. Hsu, A. Ved, R. Premkumar, B. N. Sahu, S. Kant, A. Aggarwal, P. Jassal, M. Dehghanipour, *J Energy Storage* **2025**, *132*, 117667.
57. A. K. Geim, *Science* **2009**, *324*, 1530.
58. M. F. El-Kady, Y. Shao, R. B. Kaner, *Nat Rev Mater* **2016**, *1*, 16033.

59. T. Jiang, Y. Wang, G. Z. Chen, *Small Methods* **2023**, *7*,2201724.
60. M. Ali, A. M. Afzal, M. W. Iqbal, S. Mumtaz, M. Imran, F. Ashraf, A. Ur Rehman, F. Muhammad, *Int J Energy Res* **2022**, *46*, 22336.
61. X. Li, D. Du, Y. Zhang, W. Xing, Q. Xue, Z. Yan, *J Mater Chem A* **2017**, *5*, 15460.
62. K. Hareesh, *J Energy Storage* **2024**, *84*, 110857.
63. H. Xiao, Z.-S. Wu, L. Chen, F. Zhou, S. Zheng, W. Ren, H.-M. Cheng, X. Bao, *ACS Nano* **2017**, *11*, 7284.
64. X. Xin, Y. Xu, H. Wuliji, F. Sun, Q. Liu, Z. Wang, T. Wei, X. Zhao, X. Song, L. Gao, *ACS Nano* **2023**, *17*, 657.
65. S. Byun, J. H. Kim, S. H. Song, M. Lee, J.-J. Park, G. Lee, S. H. Hong, D. Lee, *Chemistry of Materials* **2016**, *28*, 7750.
66. F. Lai, Y.-E. Miao, L. Zuo, H. Lu, Y. Huang, T. Liu, *Small* **2016**, *12*, 3235.
67. E. Scavetta, A. Mignani, D. Prandstraller, D. Tonelli, *Chemistry of Materials* **2007**, *19*, 4523.
68. G. Arrabito, A. Bonasera, G. Prestopino, A. Orsini, A. Mattoccia, E. Martinelli, B. Pignataro, P. Medaglia, *Crystals* **2019**, *9*, 361.
69. A. A. Balandin, S. Ghosh, W. Bao, I. Calizo, D. Teweldebrhan, F. Miao, C. N. Lau, *Nano Lett* **2008**, *8*, 902.
70. A. K. Geim, K. S. Novoselov, *Nat Mater* **2007**, *6*, 183.
71. Y. Zhang, T.-T. Tang, C. Girit, Z. Hao, M. C. Martin, A. Zettl, M. F. Crommie, Y. R. Shen, F. Wang, *Nature* **2009**, *459*, 820.
72. T. De Silva, C. Damery, R. Alkhaldi, R. Karunanithy, D. H. Gallaba, P. D. Patil, M. Wasala, P. Sivakumar, A. Migone, S. Talapatra, *ACS Appl. Mater Interfaces* **2021**, *13*, 56004.
73. M. F. El-Kady, Y. Shao, R. B. Kaner, *Nat Rev Mater* **2016**, *1*, 16033.
74. W. S. Hummers, R. E. Offeman, *J Am Chem Soc* **1958**, *80*, 1339.
75. Y. Wang, X. Yang, A. G. Pandolfo, J. Ding, D. Li, *Adv Energy Mater* **2016**, *6*,1600185.
76. S. Santra, A. Ghosh, B. Das, S. Pal, S. Pal, A. Adalder, *RSC Sustainability* **2024**, *2*, 1631.
77. Y. Gogotsi, B. Anasori, *ACS Nano* **2019**, *13*, 8491.
78. M. Anayee, C. E. Shuck, M. Shekhirev, A. Goad, R. Wang, Y. Gogotsi, *Chemistry of Materials* **2022**, *34*, 9589.
79. K. R. G. Lim, M. Shekhirev, B. C. Wyatt, B. Anasori, Y. Gogotsi, Z. W. Seh, *Nature Synthesis* **2022**, *1*, 601.
80. M. Ghidiu, M. R. Lukatskaya, M.-Q. Zhao, Y. Gogotsi, M. W. Barsoum, *Nature* **2014**, *516*, 78.
81. Y.-C. Hsieh, K.-T. Lee, Y.-P. Lin, N.-L. Wu, S. W. Donne, *J Power Sources* **2008**, *177*, 660.
82. W. Bi, J. Huang, M. Wang, E. P. Jahrman, G. T. Seidler, J. Wang, Y. Wu, G. Gao, G. Wu, G. Cao, *J Mater Chem A* **2019**, *7*, 17966.
83. K. Du, L. Zhang, J. Shan, J. Guo, J. Mao, C.-C. Yang, C.-H. Wang, Z. Hu, T. Ling, *Nat Commun* **2022**, *13*, 5448.
84. F. Chen, W. Zhou, H. Yao, P. Fan, J. Yang, Z. Fei, M. Zhong, *Green Chemistry* **2013**, *15*, 3057.

85. M. Chhowalla, H. S. Shin, G. Eda, L.-J. Li, K. P. Loh, H. Zhang, *Nat Chem* **2013**, *5*, 263.
86. L.-Q. Fan, G.-J. Liu, C.-Y. Zhang, J.-H. Wu, Y.-L. Wei, *Int. J Hydrogen Energy* **2015**, *40*, 10150.
87. X. Wang, M. Ma, W. Wang, C. Tang, Z. Wang, J. Ru, H. Li, B. Li, Y. Zhang, X. Zhu, *J. Mater. Chem. A* **2023**, *11*, 16383.
88. X. Wu, S. Xiao, Y. Long, T. Ma, W. Shao, S. Cao, X. Xiang, L. Ma, L. Qiu, C. Cheng, C. Zhao, *Small* **2022**, *18*, 2105831.
89. A. Raza, J. Z. Hassan, U. Qumar, A. Zaheer, Z. U. D. Babar, V. Iannotti, A. Cassinese, *Mater Today Adv* **2024**, *22*, 100488.
90. Y. Zhu, K. Rajouâ, S. Le Vot, O. Fontaine, P. Simon, F. Favier, *Nano Energy* **2020**, *73*, 104734.
91. J. Wang, V. Malgras, Y. Sugahara, Y. Yamauchi, *Nat Commun* **2021**, *12*, 3563.
92. B. Zhao, J. Song, P. Liu, W. Xu, T. Fang, Z. Jiao, H. Zhang, Y. Jiang, *J Mater Chem* **2011**, *21*, 18792.
93. O. Sadak, W. Wang, J. Guan, A. K. Sundramoorthy, S. Gunasekaran, *ACS Appl Nano Mater* **2019**, *2*, 4386.
94. J. Memon, J. Sun, D. Meng, W. Ouyang, M. A. Memon, Y. Huang, S. Yan, J. Geng, *J Mater Chem A* **2014**, *2*, 5060.
95. L. Ren, G. Zhang, Z. Yan, L. Kang, H. Xu, F. Shi, Z. Lei, Z.-H. Liu, *ACS Appl Mater Interfaces* **2015**, *7*, 28294.
96. M. Mahmood, A. Rasheed, I. Ayman, T. Rasheed, S. Munir, S. Ajmal, P. O. Agboola, M. F. Warsi, M. Shahid, *Energy & Fuels* **2021**, *35*, 3469.
97. X. Wang, H. Li, H. Li, S. Lin, W. Ding, X. Zhu, Z. Sheng, H. Wang, X. Zhu, Y. Sun, *Adv Funct Mater* **2020**, *30*, 1910302.
98. K. Nasrin, V. Sudharshan, K. Subramani, M. Karnan, M. Sathish, *Small* **2022**, *18*, 2106051.
99. A. Singha, P. Pandey, A. Sahu, M. Qureshi, *J Phys Chem Lett* **2024**, *15*, 2123.
100. C. Wan, Y. Jiao, J. Li, *J Mater. Chem. A* **2017**, *5*, 3819.
101. M. Karuppaiah, J. K. Lee, G. Ravi, *ACS Appl. Electron. Mater.* **2024**, *6*, 1504.
102. Y. Shabangoli, A. Esfandiar, M. Torkashvand, N. Ashari Astani, *ACS Appl Energy Mater* **2025**, *8*, 767.
103. W. Zhao, J. Peng, W. Wang, B. Jin, T. Chen, S. Liu, Q. Zhao, W. Huang, *Small* **2019**, *15*, 1901351.
104. Z. Zhu, Z. Wang, Z. Ba, X. Li, J. Dong, Y. Fang, Q. Zhang, X. Zhao, *J Energy Storage* **2022**, *47*, 103911.
105. P. Dutta, S. K. Deb, A. Patra, A. Majumdar, G. M. Karim, C. K. Parashar, M. K. Mohanta, M. Qureshi, U. N. Maiti, *Adv Funct Mater* **2022**, *32*,2204622.
106. Y. Qin, G. Lu, F. Yang, C. Xu, S. Jiang, Y. Wang, Y. Tang, P. Wang, *Mater Adv* **2023**, *4*, 1226.
107. R. Nasser, X.-L. Wang, A. B. G. Trabelsi, F. H. Alkallas, H. Elhouichet, J.-M. Song, *J Energy Storage* **2022**, *52*, 104619.

108.K. Jitapunkul, K. Deshsorn, K. Payakkachon, T. Chaisrithong, L. Lawtrakul, P. Iamprasertkun, *The J. of Phys. Chem. C* **2023**, *127*, 18316.
109.P. Pandey, S. Bhowmick, M. Qureshi, *ACS Appl Mater Interfaces* **2023**, *15*, 39435.
110.B. Liu, Y. Wang, H. Peng, R. Yang, Z. Jiang, X. Zhou, C. Lee, H. Zhao, W. Zhang, *Advanced Materials* **2018**, *30*,1803144.
111.S. Saha, P. Samanta, N. C. Murmu, A. Banerjee, R. S. Ganesh, H. Inokawa, T. Kuila, *Chemical Engineering Journal* **2018**, *339*, 334.
112.S. Chen, H. Jiang, Q. Cheng, G. Wang, S. Petr, C. Li, *Chemical Engineering Journal* **2021**, *403*, 126380.
113.Y. Xu, X. Su, H. Shi, J. Yu, J. Sui, Q. Zhang, L. Yu, L. Dong, *J Energy Storage* **2025**, *108*, 115123.
114.Y.-H. Liu, Z.-Y. Jiang, J.-L. Xu, *ACS Appl Mater Interfaces* **2019**, *11*, 24047.
115.H. Jiang, P. S. Lee, C. Li, *Energy Environ. Sci.* **2013**, *6*, 41.

CHAPTER 2

Experimental

This chapter outlines the instrumental methods and procedures for material characterization and device fabrication. It also provides a brief overview of key parameters related to electrochemical analysis, including cyclic voltammetry, galvanostatic charge-discharge, and electrochemical impedance spectroscopy.

Chapter 2

2.1. INTRODUCTION

This chapter covers the synthesis, fabrication, and characterization of the prepared supercapacitor electrode materials. It includes the chemicals used, characterization techniques, and electrochemical measurements, along with a brief overview of key techniques for better understanding.

2.2. REAGENTS AND CHEMICALS USED:

Cobalt nitrate hexahydrate ($Co(NO_3)_2.6H_2O$), Urea (CH_4N_2O), Nickel Chloride hexahydrate ($NiCl_2.H_2O$), Manganese chloride tetrahydrate ($MnCl_2.4H_2O$) Ammonium metavanadate (NH_4VO_3), MAX phase (Ti_3AlC_2), hydrofluoric acid (HF), manganese (II) acetate tetrahydrate, cetyltrimethylammonium bromide (CTAB), boron powder, melamine ($C_3H_6N_6$), potassium permanganate ($KMnO_4$) are from **Sigma Aldrich**. Sodium sulfate anhydrous (Na_2SO_4), Potassium hydroxide (KOH), boric acid, N, N-Dimethylformamide (N, N′-DMF), urea, ammonium chloride (NH_4Cl), graphite (particle size: 60 mesh), sodium nitrate ($NaNO_3$), sulfuric acid (H_2SO_4), and hydrogen peroxide (30% H_2O_2) are from **Merck**. Carbon paper (CP) was from **Alfa Aesar**. For the synthesis protocol, we have used Milli-Q water of 18.2 MΩ-cm. All reagents are of analytical grade and used as received.

2.3. CHARACTERIZATION OF THE AS-SYNTHESIZED MATERIALS:

Various analytical techniques were used to characterize the synthesized materials and fabricated devices. Instrumental tools used in the present studies are listed below:

(1) Powder X-ray diffraction (PXRD) analysis was done to determine the structure and phase purity of all the materials using Rigaku SmartLab using Cu K_α (λ = 1.54 Å) as the source with 9kW power.

(2) Micro-Raman spectroscopy analysis was done to determine different modes of vibration present in the sample, using a laser micro-Raman system (Horiba Jobin Vyon, LabRam HR) with and 633 nm laser excitation.

(3) Perkin Elmer (Spectrum-II) instrument with KBr pellet was used to perform Fourier-transformed infrared spectroscopic (FT-IR) studies.

(4) Field emission scanning electron microscopic (FESEM) analysis was done to determine the surface morphology of as-synthesized materials using Zeiss (Gemini) and Zeiss (Sigma) instruments, operating at the voltages of 3 kV−10 kV.

(5) Elemental mapping, morphological features, d-spacing value, and selected area electron diffraction (SAED) patterns of the samples were determined through, Field emission

transmission electron microscopy (FETEM) using JEOL (JEM-2100F) instrument with an operating voltage of 200 kV.

(6) To determine the valence state, elemental composition, and change in the electronic environment around the elements, X-ray photoelectron spectroscopy (XPS) analysis was carried out using the PHI 5000 Versa Probe III instrument features an Al–K_α X-ray source with a photon energy of 1486.6 eV. C 1s spectrum (284.77 eV), as a reference, was used to compensate for the surface charging effect. XPSPEAK 4.1 software was used to fit and deconvolute the data.

(7) Gamry Instrument model Interface1010 E was used to record all the electrochemical measurements, including galvanostatic charge-discharge (GCD), cyclic voltammetry (CV), electrochemical impedance spectroscopy (EIS), and Mott-Schottky (MS).

(8) To measure the surface potential, Kelvin Probe Force Microscopy (KPFM) analysis was carried out using an MFP-3D-BIO instrument (Asylum Research, Oxford Instruments) operated in non-contact mode with a silicon (Si) probe.

(9) The real surface and roughness analysis were characterized through an atomic force microscope (AFM) instrument of Asylum Cypher, Oxford Instruments.

(10) To know the surface potential of the synthesized material, zeta potential analysis was recorded on a Malvern Nano-ZS90 ZETASIZER instrument.

(11) The UV-Vis absorption spectra were characterized on Shimadzu UV-2600, JASCO Model V-650 and PerkinElmer Lambda 750 UV/VIS/NIR spectrophotometers at room temperature by taking reference of $BaSO_4$.

2.4. ELECTROCHEMICAL MEASUREMENTS FOR EVALUATING CHARGE STORAGE:

To evaluate the performance parameters of the as-synthesized materials, electrochemical measurements were carried out using an electrochemical analyser (model: Interface 1100E) in a three-electrode configuration. Measurements were performed in a polypropylene electrochemical cell using aqueous KOH (Chapters 3, 5, and 6) and 1 M Na_2SO_4 (Chapter 4) as electrolytes. The synthesized materials were coated onto conductive Toray carbon paper (Alfa Aesar) and used as the working electrode in Chapters 3, 4, and 6. In Chapter 5, a free-standing electrode was synthesized and directly employed. A Hg/HgO electrode was used as the reference, and a platinum wire served as the counter electrode, as shown in the **Figure 2.1a**.

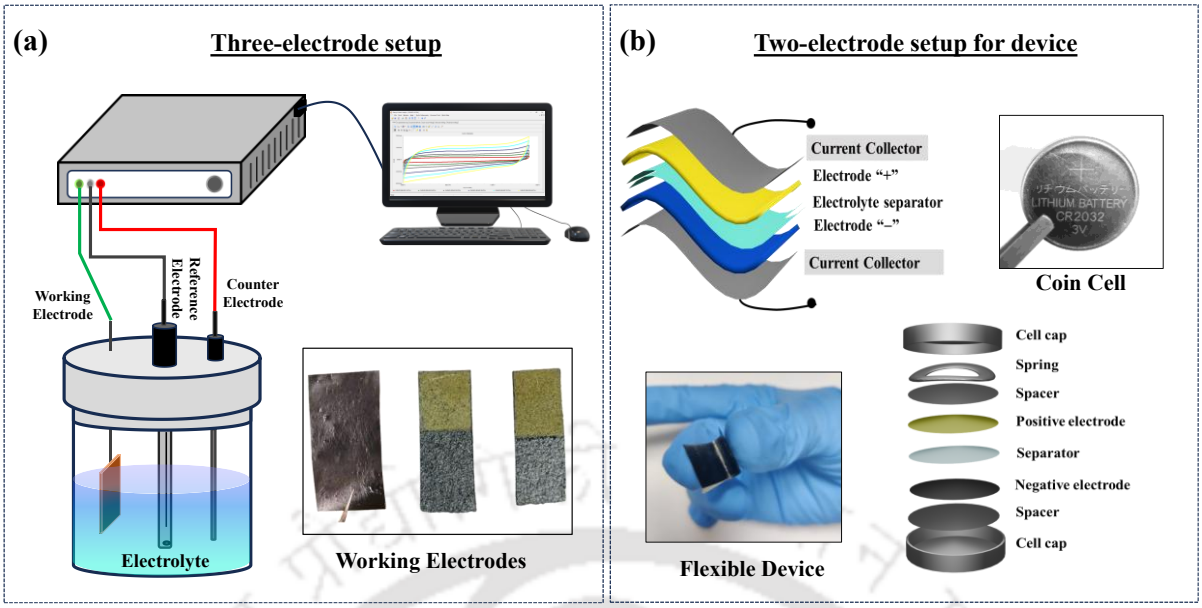

Figure 2.1: (a) Schematic representation showing the experimental setup for electrochemical measurement, where voltage is applied through a potentiostat (b) Illustrating the two-electrode setup for the device fabrication to show the practical application

To demonstrate the practical applicability of the as-synthesized materials, a two-electrode configuration was employed, using activated carbon as the negative electrode (Chapters 3, 4, and 6). A PVA–KOH gel electrolyte separator was used in Chapters 3, 5, and 6, while a PVA–Na_2SO_4 gel electrolyte separator was used in Chapter 4. For device fabrication, a pouch cell was assembled in Chapters 3, 4, and 5, and a coin cell supercapacitor was fabricated in Chapter 5. Different parts of the supercapacitor device are shown in the **Figure 2.1b**.

2.5. PERFORMANCE PARAMETER OF SUPERCAPACITOR:

2.5.1. Capacitance:

Capacitance refers to the amount of charge stored per unit and can be expressed gravimetrically, volumetrically, or in areal, depending on the type of sample. It primarily depends on factors such as, surface area of material, structural properties like porosity, the electrolyte used, the nature of faradaic reactions, and the thickness of the electrostatic EDLC layer. Several electrochemical techniques are used to determine the capacitance of an electrode. Some of these methods are outlined below:

2.5.1.1.Cyclic Voltammetry:

In voltammetry (CV) technique, the current response of a working electrode is measured as a potential is applied relative to a reference electrode. The resulting plot of current versus potential, obtained through successive linear potential sweeps in a cyclic manner, is known as

a cyclic voltammogram. The potential is initially swept from a starting voltage (V_1) to a final voltage (V_2) at a defined scan rate (mV s^{-1}), and then reversed back from V_2 to V_1.[1,2] From the shape of the obtained CV, the mechanism of charge storage (electrical double-layer capacitance or pseudocapacitance) can be predicted. CV measurements can be conducted using either a three-electrode or two-electrode configuration. The three-electrode approach is the best way to accurately determine the potential window, specific capacitance, and capacitive/diffusion behavior of materials. Choosing a suitable potential window is essential for accurately estimating the capacitance of the active material and is achieved through CV analysis by progressively raising the potential window at a very slow scan rate. Care must be taken to avoid the exponential region in the CV curve, as voltammograms showing an exponential increase in current response at high polarization (dashed line in **Figure 2.2a**) indicate that the device is being overcharged.[3] Overcharging can lead to parasitic side reactions, such as the decomposition of the electrode material, the electrolyte, or both, which compromise the performance, stability, and coulombic efficiency of the device. The capacitance of a material or device can be normalized with its mass, area, or volume of the material, which then gives specific capacitance like gravimetric (C_s, Fg^{-1}), areal (C_{area}, F cm^{-2}) and volumetric (C_{Vol}, Fcm^{-3}) capacitance respectively. After choosing a suitable potential window the capacitance can be calculated as,

$$\boldsymbol{C = Xv\Delta V \int_{v_i}^{v_f} idV} \quad \text{....(2.1)}$$

In **eqn 2.1**, i is the current density (A), ΔV is the potential window (V) of the supercapacitor, v is the scan rate (mV s^{-1}) and X can be area(cm^2), mass(g), or volume(cm^3) of the active material, Vi and V_f are the initial and final potentials respectively.[4] In the three-electrode configuration, the mass or volume is considered only for the active material of the working electrode. In contrast, both the mass and volume of the electrodes are considered for two-electrode devices.

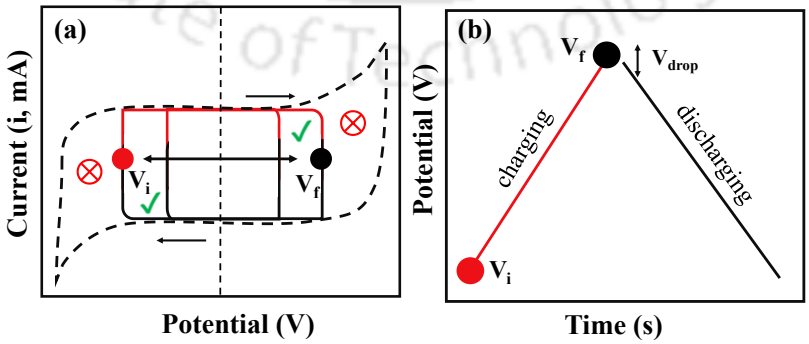

Figure 2.2: Schematics of (a) Cyclic voltammetry (CV) to choose a stable potential window (b) galvanostatic charge-discharge (GCD) curve.

2.5.1.2.Galvanostatic charge-discharge:

In Galvanostatic Charge-Discharge (GCD) technique, a constant current is applied to the electrode material, and the resulting voltage variations are recorded within a defined potential range (V_i to V_f for a positive constant current, and vice versa for a negative constant current) as a function of time. This process is also known as "current reversal chronopotentiometry." [5]When a positive constant current is applied to the working electrode, the voltage rises from an initial potential V_i to a final potential V_f over time (t), followed by the application of a negative constant current of the same magnitude, causing the voltage to decrease. Similar to CV, the shape of GCD profiles also gives information about the charge storage mechanism and kinetics.[6] This part letter is discussed in **Section 2.5.5**. Beyond analyzing the charge storage mechanism, the GCD curve can also reveal the resistive drop, which is observed at the beginning of the discharge curve of the electrode **(Figure 2.2b)**.

While determining the capacitance from GCD curves, one must be aware of the type of capacitive storage mechanism first. For linear relationships, the relations governing the capacitance can be expressed as,

$$\mathbf{C} = \frac{\mathbf{I}*\Delta\mathbf{t}}{\Delta\mathbf{V}*\mathbf{X}} \quad \text{.... (2.2)}$$

X=m, A, or V of the working electrode, and Δt represents the total discharge time. However, for a non-linear relationship, it is more appropriate to express the relation as an integral of the current over time,

$$\mathbf{C} = \mathbf{I}\int_{\mathbf{V_i}}^{\mathbf{V_f}} \frac{\mathbf{1}}{\mathbf{V(t)}}\,\mathbf{dt} \quad \text{.... (2.3)}$$

where *I* is the applied constant-current density, *t* is the discharge time, and *V*(*t*) is the potential as a function of *t*.

2.5.2. Impedance analysis followed by Distribution of relaxation time (DRT):

Electrochemical impedance spectroscopy (EIS) is a powerful technique for analyzing the electrode/electrolyte interface in supercapacitors. By applying an alternating current over a wide frequency range, the impedance of the system is measured as a function of frequency.[7] The results are commonly represented using a Nyquist plot, which displays the imaginary component of the impedance versus the real component, as shown in **Figure 2.3a.** This method gives us useful information about charge transfer resistance, electrolyte ion diffusion, and overall electrochemical behavior of the supercapacitor. The Nyquist plot for supercapacitors

can be broken down into three distinct areas: high-frequency, mid-frequency, and low-frequency. When you look at the intersection with the real impedance axis (Z_{real}), it shows the equivalent series resistance (ESR), which comes from the electrolyte, separator, and the inherent resistance of the electrode material. This is often followed by a semicircle, which is characteristic of faradaic processes and indicates the charge transfer resistance due to electron transfer at the electrode–electrolyte interface. In the high-frequency region, a 45° line appears, demonstrating the semi-infinite diffusion resistance of the material. The charge-transfer resistance at the electrode-electrolyte interface is determined from the intersection of the extrapolated semicircle with the real impedance axis.[8,9] At low frequencies, beyond the Warburg impedance region, the plot shows a vertical rise, which reflects the capacitive behavior of the electrodes. Ideally, a perfect capacitor would produce a completely vertical line in the Nyquist plot, while a purely resistive component would show a horizontal line parallel to the X-axis, with no imaginary impedance.

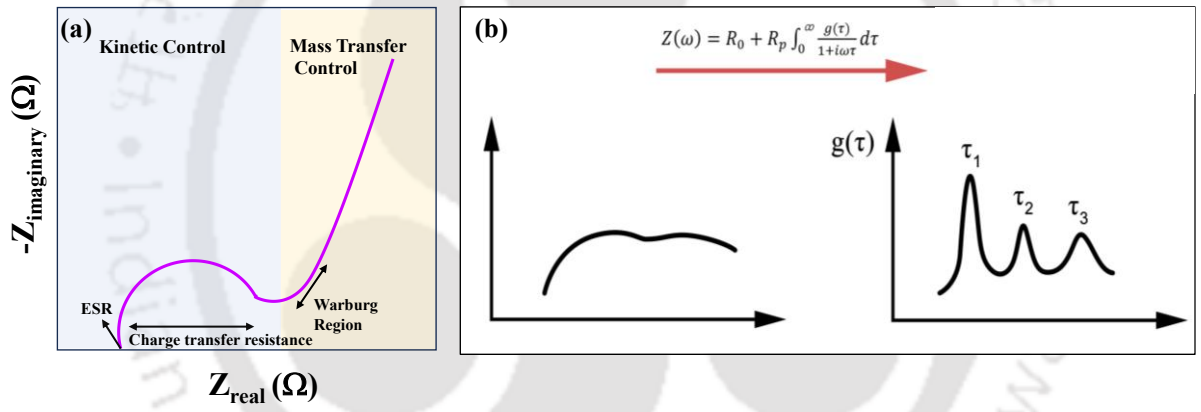

Figure 2.3. (a) Typical Nyquist plot showing EIS spectra and its different regions (b) Distribution of relaxation time curve showing conversion of frequency domain EIS data to time domain data, Reproduced from Ref [10]

EIS yields complex impedance data encompassing overlapping of processes such as ion transport from/to electroactive sites, ion diffusion, and charge transfer processes having different dynamics and they manifest themselves at different frequencies, which potentially allows their differentiation. However, extensive overlap in these time constants hinders the resolved interpretation of dynamic events in terms of their time scales. Utilizing the Distribution of Relaxation Time (DRT) methodology enables the determination of time scales required for the system to transition between equilibrium states at a specific frequency. This approach reveals distinct chemical processes aligned with various relaxation times. We have analyzed the DRT by utilizing tools in MATLAB and pyDRT tools, based on the AC impedance

spectra. Peaks observed in the high-frequency range primarily result from ion transport across the electrode/electrolyte interface. In the intermediate frequency range, the peaks are associated with the charge transfer process, while those in the low-frequency range are linked to electrode diffusion.[11] Our analytical method involves determining the Distribution of Relaxation Time (DRT) for the measured sample, as outlined in **equation 2.4**.[10]

$$\boldsymbol{Z(\omega) = R_0 + R_{pol} \int_{-\infty}^{+\infty} \frac{\tau(\log(\tau))}{1+j\omega\tau} d(\log(\tau))} \quad \ldots. (2.4)$$

Here, $\boldsymbol{R_0}$ series resistance, $\boldsymbol{Z(\omega)}$ represents the impedance of the processes, R_{pol} stands for the total polarization resistance, $\boldsymbol{\tau}$ signifies the relaxation time, and **ω** denotes the frequency. After transformation, the DRT converts impedance data, originally collected as a function of frequency, into a spectrum of time constants (or relaxation times) associated with different electrochemical processes. Each peak in the DRT plot corresponds to a distinct process occurring at a specific timescale, and the area under each peak represents the polarization resistance of that particular process, presented in **Figure 2.3b.**

Explanation of Each Region:

1. **High Frequency region:** Interfacial contact/conductivity of composite. Typically assigned to *ohmic resistance* or fast interface phenomena, such as the electrolyte resistance in supercapacitors
2. **Mid-frequency region:** Associated with *charge-transfer resistance*, *adsorption/desorption processes*, or other electrode reaction kinetics.
3. **Low-frequency region:** Diffusion processes of the electrolyte, and reveal how efficiently ions can fill all available spaces in the electrodes over longer timescales

2.5.3. Energy and Power density:

Energy and power are the two important parameters for the characterization of electrochemical energy storage devices. Specific energy (Wh kg^{-1}) or energy density (Wh L^{-1}, or Wh cm^{-2}) is the amount of energy stored in an energy storage device per unit mass/ volume/area of the electrode active materials or the whole device, respectively. Specific power (W kg^{-1}) or power density (W L^{-1}, or W cm^{-2}) is the amount of power an energy storage device can deliver per unit mass or volume/area of the electrode active materials or the whole device, respectively. The respective density was evaluated by using the given equation.

$$\mathbf{E} = \frac{\mathbf{1}}{\mathbf{2*3.6}}\mathbf{c_s}\Delta\mathbf{V^2} \quad \text{....(2.5)}$$

$$\mathbf{P} = \frac{\mathbf{E\times3600}}{\mathbf{\Delta t}} \quad \text{....(2.6)}$$

The power and energy densities of a supercapacitor are influenced by two parameters, potential window and specific capacitance, which can be modulated by tuning the active surface area and electroanalytical properties of an electrode material.

2.5.4. Cyclic stability and Coulombic efficiency:

In practical applications, durability serves as a crucial indicator for assessing the quality of SCs. To evaluate the cyclic stability of the composite electrode, galvanostatic charge-discharge tests were conducted at a constant current density within a certain potential range. Coulombic efficiency is another essential metric, representing the ratio of charge discharged to charge stored during each cycle. It is expressed as:

$$\boldsymbol{Coulombic\ efficiency}\ (\boldsymbol{\eta}) = \frac{\boldsymbol{Discharging\ time(td)}}{\boldsymbol{Charging\ time(\ tc)}} \times \mathbf{100} \quad \text{....(2.7)}$$

A high coulombic efficiency indicates minimal energy loss during the charge-discharge process, signifying excellent reversibility and stability of the electrode material. Both parameters are crucial for determining the practicality and reliability of supercapacitors in real-world applications.

2.5.5. Determination of capacitance type and quantification techniques

The distinction between supercapacitors and batteries remained clear until the 1970s, when Conway identified redox-active metal oxides, such as RuO_2[12] and MnO_2[13], which exhibit surface-limited charge storage. Subsequently, the emergence of two-dimensional (2D) materials, including conductive polymers, metal oxides, and transition metal carbides and nitrides, layered double hydroxide (LDH) blurred the boundaries between batteries and supercapacitors. This convergence blurs the traditional distinction between these technologies, highlighting the need for further investigation to fully understand and optimize their performance potential. The subsequent section discusses several techniques for the accurate identification of energy storage materials.[14]

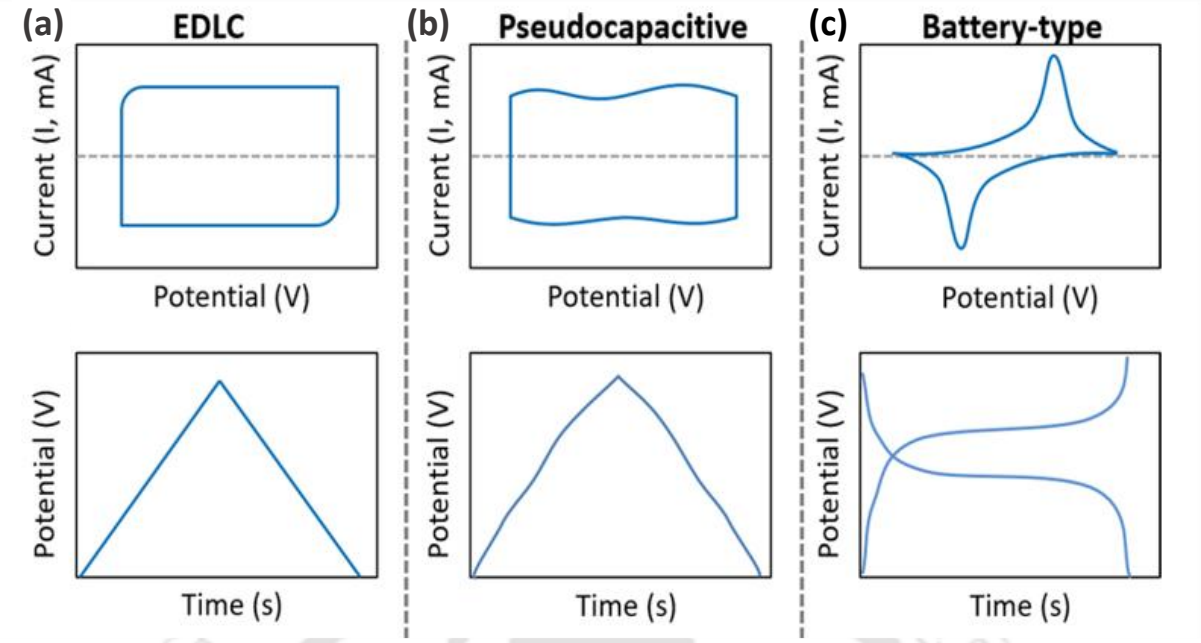

Figure 2.4. Determination of charge- storage mechanism analysing CV and GCD curve of (a) EDLC type (b) Pseudocapacitive type (c) Battery type materials showing significant differences in the polarisation curves. Adapted from ref.[15]

To accurately distinguish pseudocapacitive materials from EDLC and battery-type materials, analyzing CV and GCD profiles plays a critical role. For EDLC materials, the CV curve is strictly rectangular, the GCD profile shows a linear relationship between potential and time **(Figure 2.4a)**, and the b value is 1in the current potential relationship **Eqn. 2.8**.

$$\boldsymbol{i(V) = av^b} \qquad \text{....(2.8)}$$

(where *i(V)* is the current at specific potential, *a* and *b* are constants and *v* represent the scan rate). Materials exhibiting prominent redox peaks without significant separation and highly reversible reactions occurring without phase changes resulting in symmetrical CV curves and GCD profiles with an almost linear potential-time relationship are characteristic of pseudocapacitive behavior, shown in **Figure 2.4b**. This indicates that the charge storage involves fast, surface or near-surface redox reactions, in pseudocapacitive and the b value for pseudocapacitive materials is close to 1, indicating capacitive-like behavior, but with contributions from fast, reversible redox reactions. In contrast, battery-type materials exhibit CV curves with distinct redox peaks and large peak separations, but no phase transformation occurs during the charging process. GCD profiles also show noticeable plateaus, regardless of whether these features diminish at high rates, **Figure 2.4c**. The b value for bulk battery-like materials is typically around 0.5, reflecting diffusion-limited processes. However,

nanostructured, or specially engineered battery materials can exhibit b>0.5, suggesting kinetics similar to pseudocapacitive behavior.[16]

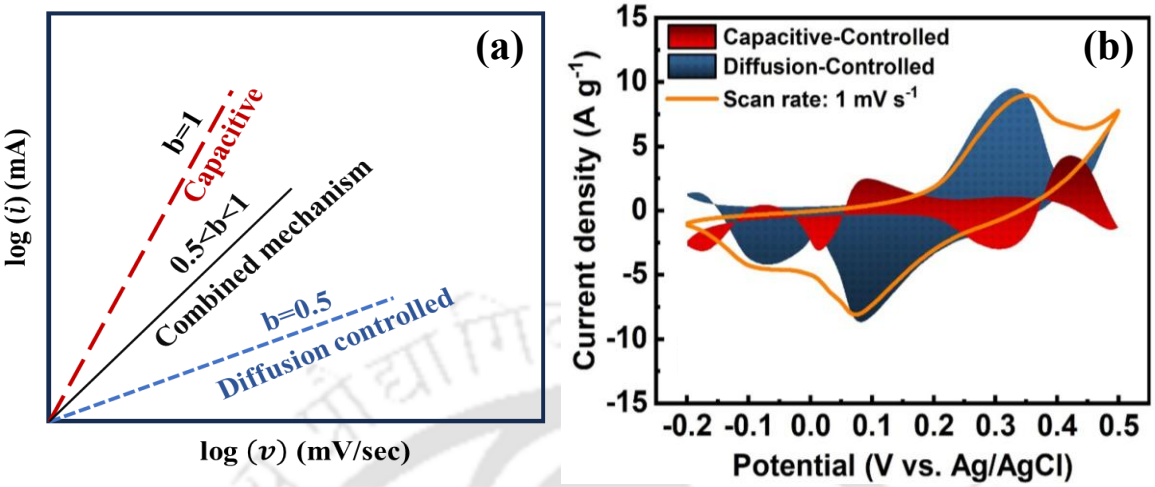

Figure 2.5: (a) Plot of log (scan rate) vs log (current) for evaluating the b-value, providing insight into the charge storage mechanism (b) Capacitive and diffusion contribution of obtained from Dunn's analysis, Adapted from ref.[17]

Ideally, for pseudocapacitors, although the b value should be near 1, this can depend on electrode material and architecture, especially the available porosity and thickness of the electrode. Now, to quantify the charge storage contributions, Trassati and Dunn have formalized a cyclic voltammetry-based procedure with the help of the equation,[18]

$$i = k_1 v + k_2 v^{1/2} \quad \text{....(2.9)}$$

$$\frac{i\,(V)}{v^{1/2}} = k_1 v^{1/2} + k_2 \quad \text{....(2.10)}$$

By calculating constants k_1 and k_2 in **Eqn. 2.9**, the contributions of current from capacitive and diffusion processes can be calculated at specific potentials as depicted in **Figure 2.5b.**

- $k_1 v$ represents the capacitive contribution (surface-controlled process).
- $k_1 v^{1/2}$ represents the diffusion-controlled contribution (battery-like behavior).

2.6. REFERENCES:

1. G. A. Mabbott, *J. Chem. Educ.* **1983**, *60*, 697.
2. J. J. Van Benschoten, J. Y. Lewis, W. R. Heineman, D. A. Roston, P. T. Kissinger, *J. Chem. Educ.* **1983**, *60*, 772.
3. T. S. Mathis, N. Kurra, X. Wang, D. Pinto, P. Simon, Y. Gogotsi, *Adv Energy Mater* **2019**, *9*, 1902007
4. A. Noori, M. F. El-Kady, M. S. Rahmanifar, R. B. Kaner, M. F. Mousavi, *Chem. Soc. Rev* **2019**, *48*, 1272.
5. W. Lu, R. Hartman, L. Qu, L. Dai, *J Phys. Chem. Lett.* **2011**, *2*, 655.
6. M. D. Stoller, R. S. Ruoff, *Energy Environ. Sci.* **2010**, *3*, 1294.
7. E. Barsoukov, J. R. Macdonald, Eds., *Impedance Spectroscopy*, Wiley, **2018**.ISBN:9781119381860
8. A. Ch. Lazanas, M. I. Prodromidis, *ACS Measurement Science Au* **2023**, *3*, 162.
9. M. E. Orazem, B. Tribollet, *Electrochemical Impedance Spectroscopy*, Wiley, **2008**. ISBN: 978-1-118-52739-9
10. Y. Lu, C.-Z. Zhao, J.-Q. Huang, Q. Zhang, *Joule* **2022**, *6*, 1172.
11. A. B. Tesler, D. R. Lewin, S. Baltianski, Y. Tsur, *J. Electroceram.* **2010**, *24*, 245.
12. H. Kim, B. N. Popov, *J Power Sources* **2002**, *104*, 52.
13. Y.-C. Hsieh, K.-T. Lee, Y.-P. Lin, N.-L. Wu, S. W. Donne, *J Power Sources* **2008**, *177*, 660.
14. B. E. Conway, *Electrochemical Supercapacitors: Scientific Fundamentals and Technological Applications*, Kluwer Academic/Plenum Publishers,**1999**. ISBN: 978-1-4757-3058-6
15. Y. Jiang, J. Liu, *Energy Environ. Mater.* **2019**, *2*, 30.
16. T. Schoetz, L. W. Gordon, S. Ivanov, A. Bund, D. Mandler, R. J. Messinger, *Electrochim. Acta* **2022**, *412*, 140072.
17. M. H. Sepahdar, S. M. Masoudpanah, M. Sh. Bafghi, S. Mohammadi, M. Namayandeh Jorabchi, *J. Energy Storage* **2024**, *104*, 114557.
18. V. Augustyn, P. Simon, B. Dunn, *Energy Environ. Sci.* **2014**, *7*, 1597.

CHAPTER 3

Internal stimuli strategy: High-valent vanadium-enabled redox activation and NiMn-LDH synergy for advanced supercapacitors

The critical role of spectator-metal ions, such as vanadium, in enhancing electrochemical performance in supercapacitors has been demonstrated. The strategy centered on increasing surface activity with vanadium and leveraging multiple redox-active ions to optimize electrochemical performance and durability, leading to the development of an efficient pseudo-capacitor material.

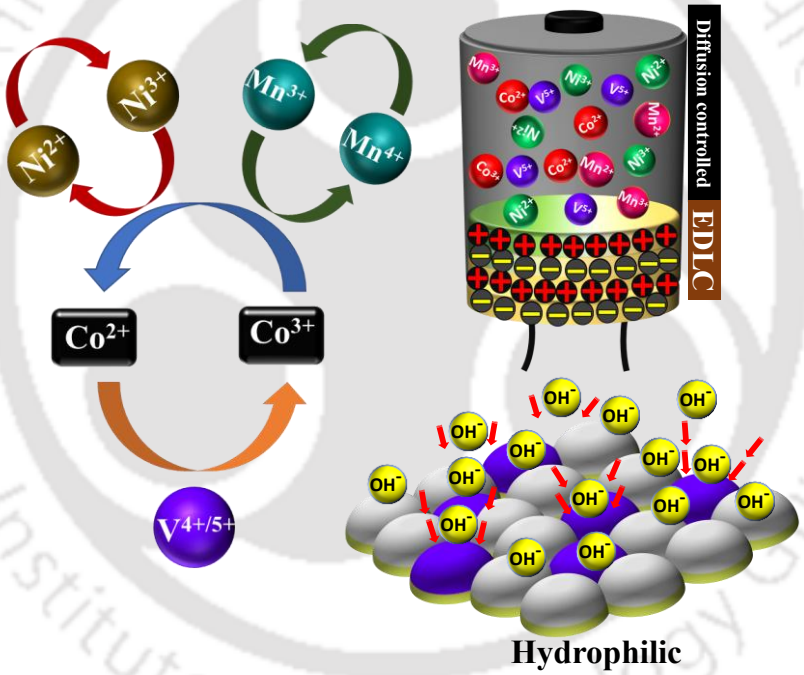

Part of this manuscript has been published in ***Chem. Comm.*** **2023, 59, 1038**

3.1. INTRODUCTION:

Increase in world-wide population has led to the upsurge usage of the energy-based appliances to meet their daily needs. Significant efforts to develop sustainable and efficient energy storage devices, among which supercapacitors (SCs) have proved to be much efficient due to their higher charge-discharge rate, economical, and long charge-discharge cycles[1,2]. However, SCs low energy density restricts its wide range applicability[3–5]. The power and energy densities of a supercapacitor are critically influenced by two parameters, the potential window at which a supercapacitor operates and the specific capacitance which are dependent on the active surface area and electro-redox properties of an electrode material[6,7]. Based on energy storage mechanism, supercapacitors are mainly classified as electric double layer capacitors (EDLC) and pseudo-capacitors[8,9]. In general, pseudo-capacitors accompanies higher energy storage than EDLCs, because of the fast and reversible redox reactions during charge-discharge process[10]. The electrode materials have a significant impact on the performance of devices. Considering the Faradaic process occurring at the electrode-electrolyte interface, transition metal-based hydroxides, oxyhydroxides, and/or layer double hydroxides, are best suited in virtue of their variable oxidation states, supporting the faster redox cycles and higher stability in the alkaline medium [11,12].It has been discovered that environmentally friendly MOOH (M = Fe, Co, Ni, Mn, V, and Al) have distinct electronic structures, variable valence states, and abundant natural resources. Generally, MOOHs are formed as a two-dimensional (2D) layered structure, consisting of the edge-sharing octahedral (MO_6) subunits stacked to form a 2D layered structure. The interplanar spaces are occupied with various ionic species from the precursor that intercalated during the synthesis process, which determines the interplanar spacing and provides structural stability. These 2D-layered structures with the intercalated ions (spacers) can enhance the conductivity, surface texture, and adjust the volume extension of the material during prolonged electrochemical applications, making MOOHs promising electrode for energy storage.[13–15] These attributes can result in higher theoretical energy storage capacities at reduced costs, making them a promising alternative to commercial products. Cobalt-based hydroxides and/or oxyhydroxides have been widely utilized as pseudo-capacitor materials due to their ease of fabrication, tuneable morphologies, ease of electronic structure tuning by doping, and facile redox cycle ($Co^{2+} \leftrightarrow Co^{3+} \leftrightarrow Co^{4+}$)[16]. However, the Co-oxy hydroxide materials reported so far, have non-porous structures with poor specific surface area, which makes a huge diffusional limitation for the solvated ions and deteriorates the performance of the final electrode[17]. Recently, Bimetallic oxyhydroxides synergistically

enhance electrochemical performance by offering multiple redox couples as active sites.[18] Cobalt and vanadium-based binary hydroxides have also been reported as supercapacitors electrode materials having high charge storage capacity[19]. Furthermore, incorporating "spectator ions," which are redox-inactive, enhances overall electrochemical performance by improving ionic conductivity, stabilizing electrode structure, and facilitating efficient charge transfer.[20] This led to incorporating vanadium into cobalt oxyhydroxide to add up their pros compensating the individual shortcomings. Further, the charge transfer kinetics of the system can be improved using redox-active double hydroxide systems compatible with the present system. In this regard, layered double hydroxide (LDH) is best component owing to its two-dimensional structure with efficient redox active of 3d transition metal centres providing the required high active surface area and high stability in harsh alkaline conditions. [21,22]

In this work, *in-situ* grown cobalt vanadium oxyhydroxide, CoVO(OH) (COV), utilizing hydrothermal method over carbon paper (CP) has been demonstrated. To further improve the electrochemical performance of COV material, we have directly grown NiMn-LDH nano flakes over the COV/CP electrode by hydrothermal method to ensure a better contact and interaction between the electro-active metal centres. The optimized NiMn- LDH@COV/CP hybrid electrode delivered a superior specific capacitance value of 786 Cg^{-1} at a current density of 1 Ag^{-1} with a high capacitive retention of 96% compared to the bare COV/CP which showed a retention capacitance of 88% after 5000 cycles at a current density of 25 Ag^{-1}.

3.2. EXPERIMENTAL SECTION:

3.2.1. Synthesis of CoVO (OH):

Cobalt and vanadium precursors are taken in different ratios (1:0,2:1,1:1,1:2) dissolved in 25mL deionized water followed by the addition of NH_4Cl (2.5 mmol) and CH_4N_2O (4 mmol) and hydrothermally treated at 120 ˚C in a 50mL Teflon autoclave with activated CP [23]for 8h. The synthesized product grown on CP is cleaned with deionized water and absolute ethanol and dried overnight in vacuum oven. The electrodes were named according to their molar ratio of cobalt and vanadium. (COV11 indicates Co:V = 1:1)

3.2.2. Synthesis of NiMn-LDH@CoVO (OH):

To prepare NiMn-LDH@CVO, $NiCl_2.6H_2O$, $MnCl_2.4H_2O$ in 3:1 ratio and hexamine(2mmol) dissolved in 35mL deionized water, hydrothermally treated along with CoVO (OH)/CP substrate at 90ºC for 8h.[24]

Scheme 3.1: Schematic representation of synthetic protocol utilized for the fabrication of the composite electrode (NiMn-LDH@COV/CP) in a two-step hydrothermal method.

3.3. RESULTS AND DISCUSSION:

3.3.1. Phase and Structural Analysis

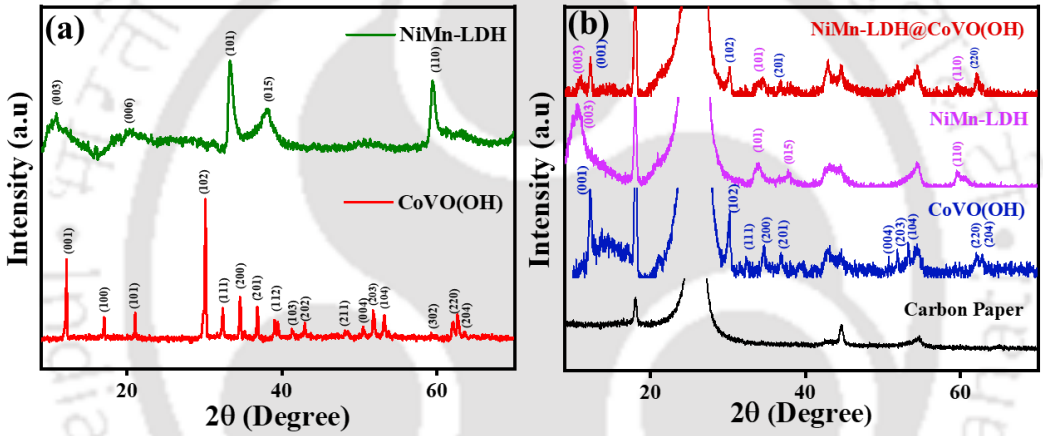

Figure 3.1: Powder X-ray diffraction of (a) Individual powder sample collected and (b) CoVO(OH), NiMn-LDH and NiMn-LDH@CoVO(OH) on carbon paper.

The formation and phase purity of the as-synthesized materials were confirmed using the powder X-ray diffraction (PXRD) method. **Figure 3.1** shows the XRD pattern of bare COV (CoVO (OH)) and NiMn-LDH. All the peaks are indexed with no impurity peaks. The COV corresponds to the hexagonal phase (JCPDS no. 00-057-0519) while the NiMn-LDH corresponds to the rhombohedral phase (JCPDS no. 38-0715). The peak at ~10° (2θ) for the NiMn-LDH corresponds to the interlayer spacing of LDH sheets in the "*c*" direction (003 plane) with an interplanar spacing of ~1.19 nm, confirming its two-dimensional (2D) nature. Further, in XRD presence of peaks corresponding to both COV and NiMn-LDH further confirms the successful formation of the composite.

3.3.2. Morphological Analysis:

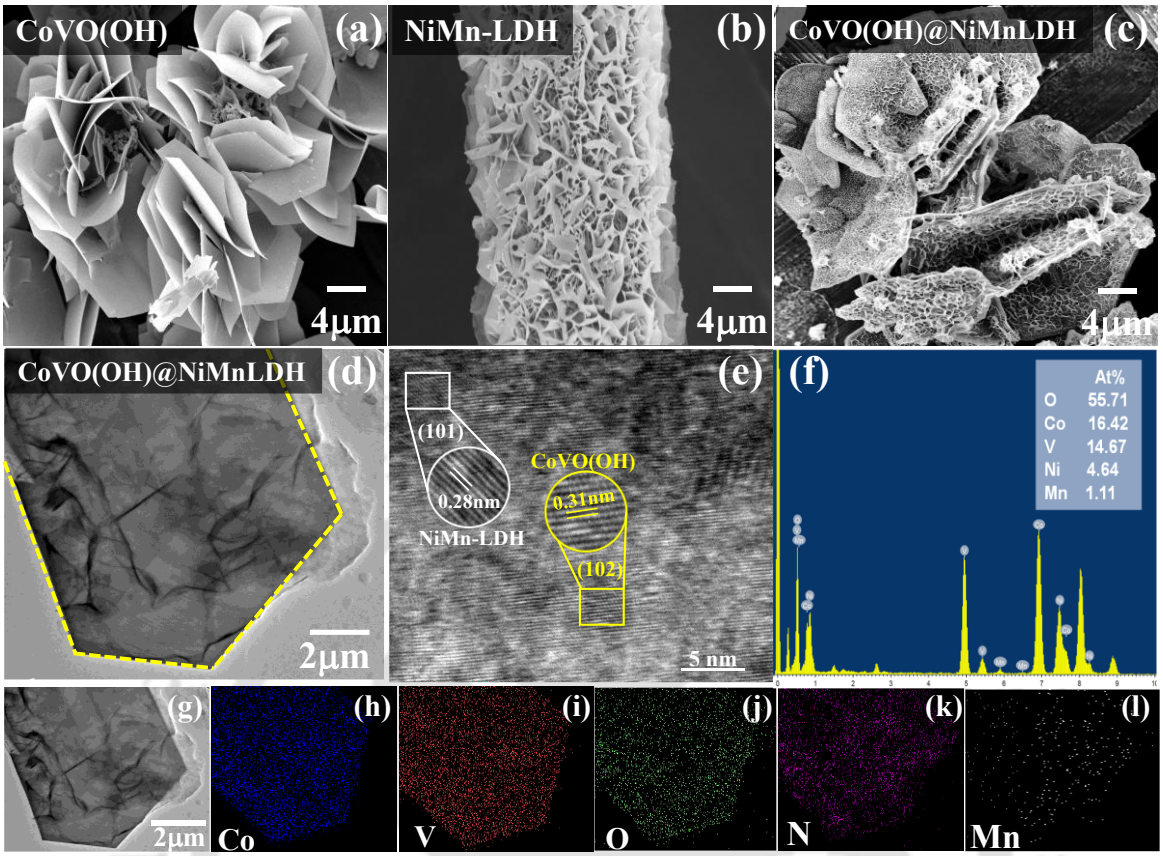

Figure 3.2: FESEM images of (a) hexagonal 2D sheet COV (b) NiMn-LDH nano sheets, (c) NiMn-LDH@COV grown over CP substrate, and (d) FETEM image of the composite, NiMn-LDH@COV, showing the presence of nanosheets over the hexagonal sheet structure.(e)HRTEM image of the composite with *d*-spacing values corresponding to respective planes of individual materials, (f) EDX spectra of NiMn-LDH@COV (g) FETEM image of NiMn-LDH@COV showing the presence of nanosheets over the hexagonal sheet structure (h-l) EDS mapping of composite showing the presence of (e) cobalt, (f) vanadium, (g) oxygen, (h) nickel and (i) manganese.

Morphologies of as-synthesized materials over CP were investigated using FESEM technique. **Figure 3.2a** shows FESEM image of COV/CP, confirming the formation of uniformly distributed hexagonal plate-like structures on the CP substrate. The average plate size of ~12µm exposed a larger surface area for further deposition of NiMn-LDH. The morphology of NiMn-LDH (**Figure 3.2b**) is confirmed by individually growing the same on a CP substrate, where a uniformly grown nanosheet structure has been observed. In the composite, **Figure 3.2c**, there is the presence of hexagonal plates, corresponding to COV, along with nanosheet structures, corresponding to NiMn-LDH,

deposited over its surface, thus increasing the overall surface area, much needed to enhance the active sites for charge storage. The sheet structures of the as-synthesized materials were further confirmed using field emission transmission electron microscopy (FETEM) technique. (**Figure 3.2d**) is the FETEM image of the composite, NiMn-LDH@COV, displaying the uniform deposition of the nanosheet (corresponding to NiMn-LDH) over the exposed surface of hexagonal sheet structure of the COV material. The high-resolution transmission electron microscope (HRTEM) image of the composite was recorded to further validate the presence of NiMn-LDH over the COV surface. shows the HRTEM image with two different lattice fringes. The *d*-spacing value of 0.21nm corresponds to the (102) plane of CoVO (OH) and 0.25nm corresponds to (101) plane of NiMn-LDH.

The scanning transmission electron microscopy energy-dispersive X-ray spectroscopy (STEM-EDX) elemental mapping was recorded for the composite to show the presence of all the elements (**Figure 3.2 h-l**), cobalt, vanadium, oxygen, nickel and manganese in the composite, confirming the homogenous deposition of the LDH over the COV.

3.3.3. Surface area Analysis:

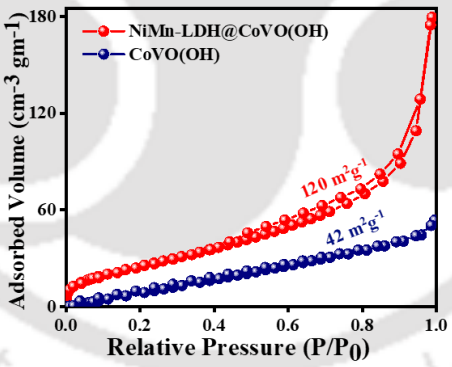

Figure 3.3: N_2 adsorption and desorption curves of bare COV and NiMn-LDH@COV composites.

The adsorption-desorption analysis revealed surface areas of 42 m^2g^{-1} for COV and 120.43 m^2g^{-1} for NiMn-LDH@COV, indicating a significant increase in surface area after NiMn-LDH incorporation, which will provide a better surface for charge storage.

3.3.4. Electronic State Analysis:

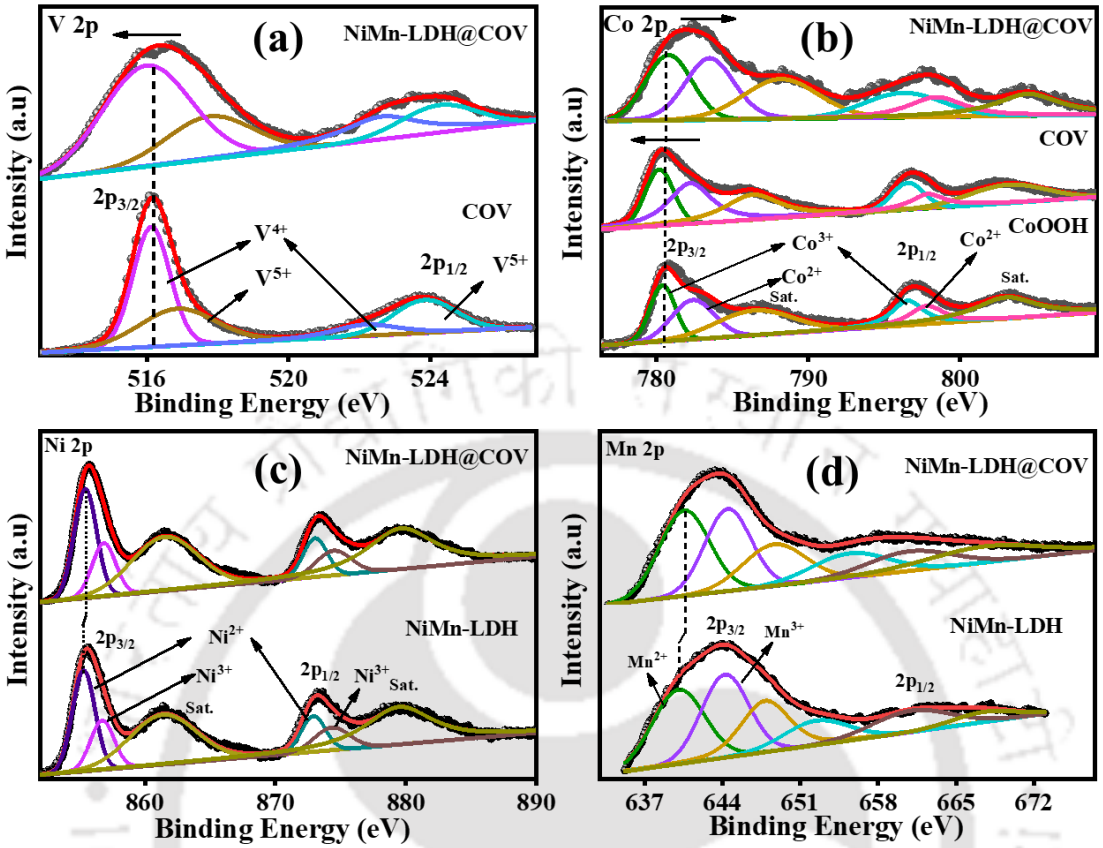

Figure 3.4: (a) V 2p of COV and NiMn-LDH@COV (b) Co 2p of CoOOH, COV and NiMn-LDH@COV and (c) Ni 2p and (d) Mn 2p of NiMn-LDH and NiMn-LDH@COV, respectively.

To investigate the electronic and valence state of elements present in the synthesized material X-ray Photoelectron spectroscopy was utilized. From the core-level V 2p spectra **Figure 3.4a** of COV and NiMn-LDH@COV it is confirmed that Vanadium is present in high valent +4 and +5 oxidation states. **Figure 3.4b** shows Co 2p core level spectra CoO(OH), COV, and NiMn-LDH@COV. In CoO (OH), the $2p_{3/2}$ peak at 780.61 eV and $2p_{1/2}$ peak at 782.46 eV confirms the presence of Co^{3+}, while the $2p_{3/2}$ peak at 796.60 and $2p_{1/2}$ peak at 798.02eV confirms the presence of Co^{2+}. Co $2p_{3/2}$ and Co $2p_{1/2}$ are energetically separated by about 15.9 eV. The shake-up satellite peaks are observed at 786.52 and 803.13 for Co $2p_{3/2}$ and $2p_{1/2}$, respectively. After the incorporation of high valent vanadium into CoO(OH), the valence state of Co shifted from Co^{2+} to Co^{3+} and red-shifted by ~0.23 eV showing strong electronic interaction between Cobalt and vanadium. V^{5+} has a vacant orbital, where there is partial charge polarisation from Cobalt to Vanadium there by increasing the faradic reaction. Again, in the composite NiMn-LDH@COV, Co2p core level spectra show a blue shift in binding energy.

Figure 3.4(c, d) shows Ni and Mn core level 2p spectra, where Ni is in +2 and +3 oxidation states and Mn is in +3 and +4 oxidation states in the composite NiMn-LDH@COV and NiMn-LDH. There is a shift in the peak position of Ni 2p and Mn 2p core-level spectra toward higher binding energy, which indicates good electronic interaction between NiMn-LDH nanosheets and COV hexagonal plates in the composite material.

3.3.5. Electrochemical Analyses:

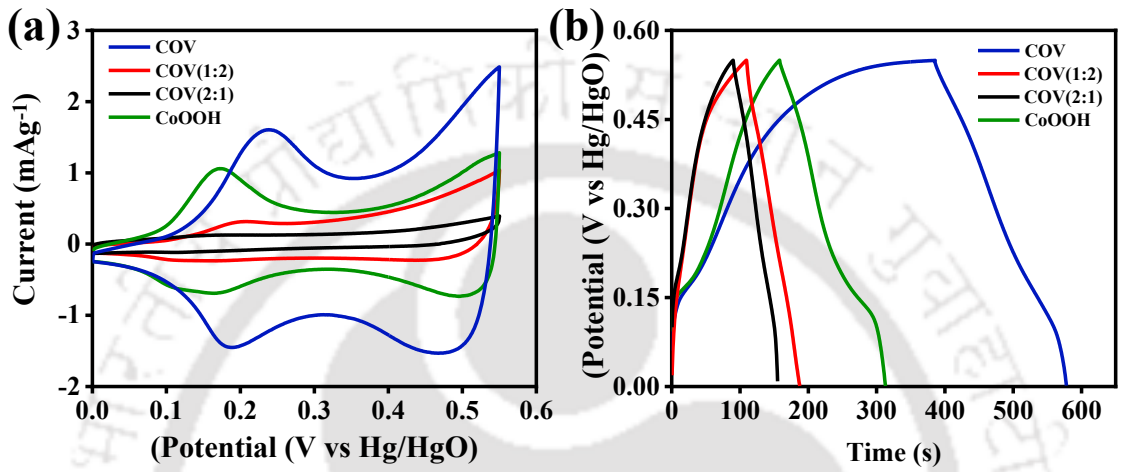

Figure 3.5: Comparative (a) CV analysis 10mV s^{-1} and (b) GCD analysis at 1A g^{-1} of CoVO(OH) with varying Co to V ratio.

The electrochemical activity of the as-synthesized materials was evaluated by cyclic voltammetry (CV) and galvanostatic charge-discharge (GCD) tests using the synthesized electrodes as working electrodes, Hg/HgO (1M KOH) as a reference electrode and platinum as a counter electrode in 1M KOH electrolytic solution. Prior to recording their electrochemical performances, each electrode was subjected to 20 cyclic voltammetric (CV) cycles at a scan rate of 100 mV s^{-1} to stabilize the system by enhancing ion diffusion. Hence, more electrolytic ions reach the electrode-electrolyte interface. The best-performing composite has been optimized using different molar ratios of cobalt and vanadium in the mixed oxyhydroxide material, as shown in **Figure 3.5**. The COV with the molar ratio of 1:1 (Co: V) displayed a larger CV curve area with an extended charge discharge time as compared to other counterparts' indicating its higher specific capacitance value. An optimal balance of Cobalt and vanadium exhibits better electrochemical performance, whereas excessive vanadium content can cause structural collapse and reduced surface area, negatively impacting performance. A lower vanadium content also underperforms, emphasizing the importance of an optimal Co: V ratio for enhanced electrochemical performance. **Figure 3.6a** shows the CV curves of different

electrodes, COV, NiMn-LDH, and NiMn-LDH@COV, measured at a scan rate of 10 mV s^{-1}. The cyclic voltammetric curve of the NiMn-LDH@COV electrode displays the largest integral area of the closed curve and a higher redox potential range, thus depicting its superior specific capacitive behavior compared to its counterparts. This is further supported by the longer charge-discharge time in the GCD analysis in **Figure 3.6b**. The capacitance value for the composite electrode, NiMn-LDH@COV, was found to be 786 C g^{-1}, which is significantly higher than that of the bare NiMn-LDH (284 C g^{-1}) and COV (350 C g^{-1}). **Figure 3.6c** represents the CV curves of the best performing composite electrode, NiMn-LDH@COV, at different scan rates (10 - 100 mV s^{-1}) within the voltage range of -0.1 V − 0.6 V. We observed an increase in the scan rate, and the oxidation and reduction peaks shifted to higher and lower potential, respectively. The shift in potential is attributed to the non-equilibrium dynamics of ion diffusion with respect to that of the increase in sweep rate causing polarization in ion transport, leading to more potential to be given to drive the oxidation and reduction processes.

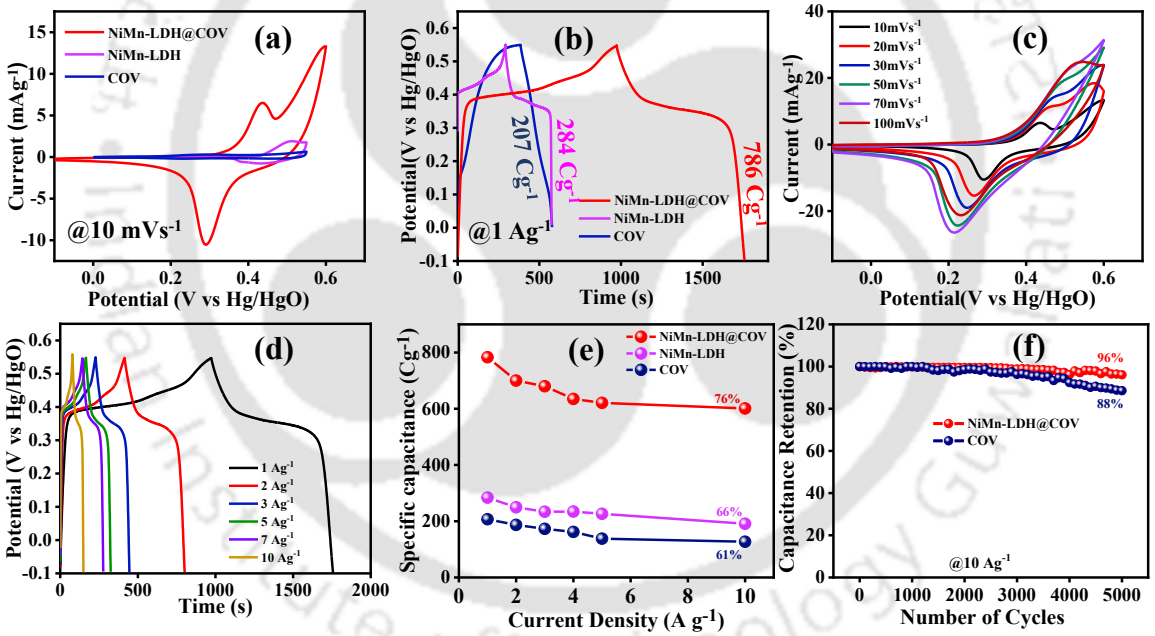

Figure 3.6: Comparative (a) CV at 10mV s^{-1} (b) GCD at 1A g^{-1} plots of the fabricated electrode materials (c) CV plots of the composite, NiMn-LDH@COV/CP, measured at different scan rates (10-100 mV s^{-1}), (d) GCD curves of the composite, NiMn-LDH@COV/CP, measured different current densities, (e) Specific capacitance of different obtained electrodes at various current densities, and (f) long-term cyclic performance of the composite electrode at 10 Ag^{-1} in 1M KOH obtained from GCD curves to depict its high stability.

In addition, a sharp redox peak corresponding to the redox activity of Ni, Mn, and Co is observed. The noticeable peak separation in the redox couple indicates the battery-type

behavior of the composite electrode. In the GCD, obtained at different current density shown in **Figure 3.6d** has a charge-discharge plateau, further indicating a battery-type behaviour of the composite. The incorporation of NiMn-LDH onto the CVO hexagonal sheets led to a ~2-fold enhancement in the specific capacity value. The increment in the C_s is due to the improved surface area (confirmed by BET analyses), which enables the interaction of more electrolytic ions with the increased electroactive species of the electrode material, thereby enhancing the Faradaic process and increasing the capacitance. Moreover, with an increase in the current densities from 1 Ag^{-1} to 10 Ag^{-1}, there was a 76% retention of the specific capacitance, indicating the good charge-discharge rate capability of the composite material.

Further, for practical applications, cyclic stability is an important parameter for measuring the quality of pseudo-capacitors. Herein, we have performed 5000 GCD cycles for the bare COV and composite NiMn-LDH@COV electrodes at 10 Ag^{-1} **(Figure 3.6f)**. The bare COV electrode showed 88% capacitance retention, while the composite electrode showed a higher (96%) retention in capacitance, confirming its high durability and reusability for practical applications.

3.3.6. Electrochemical Impedance Spectroscopy (EIS) Analyses:

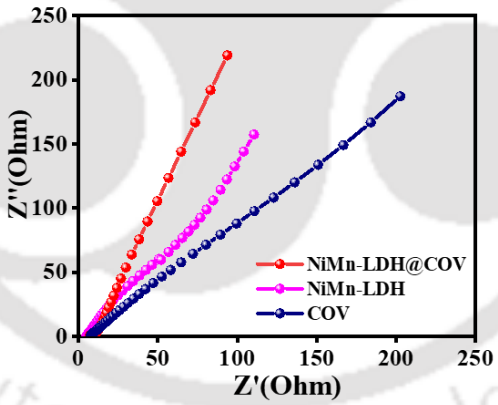

Figure 3.7: Nyquist plot of all the electrodes obtained from EIS measurements for composite NiMn-LDH@COV/CP, along with its pristine COV/CP, and NiMn-LDH/CP.

The electrochemical reaction kinetics at the electrode-electrolyte interface is one of the crucial factors for determining the pseudo-capacitive behaviour of a material. The charge transfer resistance (R_{ct}) at the interface determines the rate of the redox reaction, which was evaluated using electrochemical impedance spectroscopy (EIS) at an open circuit potential (OCP). **Figure 3.7** shows the Nyquist plot of the bare and composite electrodes obtained by the EIS technique. The lower R_{ct} value for the composite, NiMn-LDH@COV, (12 **Ω**),

compared to that of bare COV (43 Ω) and NiMn-LDH (50 Ω) proves the facile charge transfer process occurring at the electrolyte interface during the cyclic redox reactions. The low resistance can also be attributed to the enlarged specific surface area of the composite electrode material and the strong interaction between the nanosheet structures (NiMn-LDH) and hexagonal sheets (COV), accelerating the ion transfer processes. Additionally, the steeper slope at the low-frequency region for the composite confirms its higher capacitive nature due to the lower diffusive resistance of the electrolyte ions.

3.3.7. Charge Storage Mechanism:

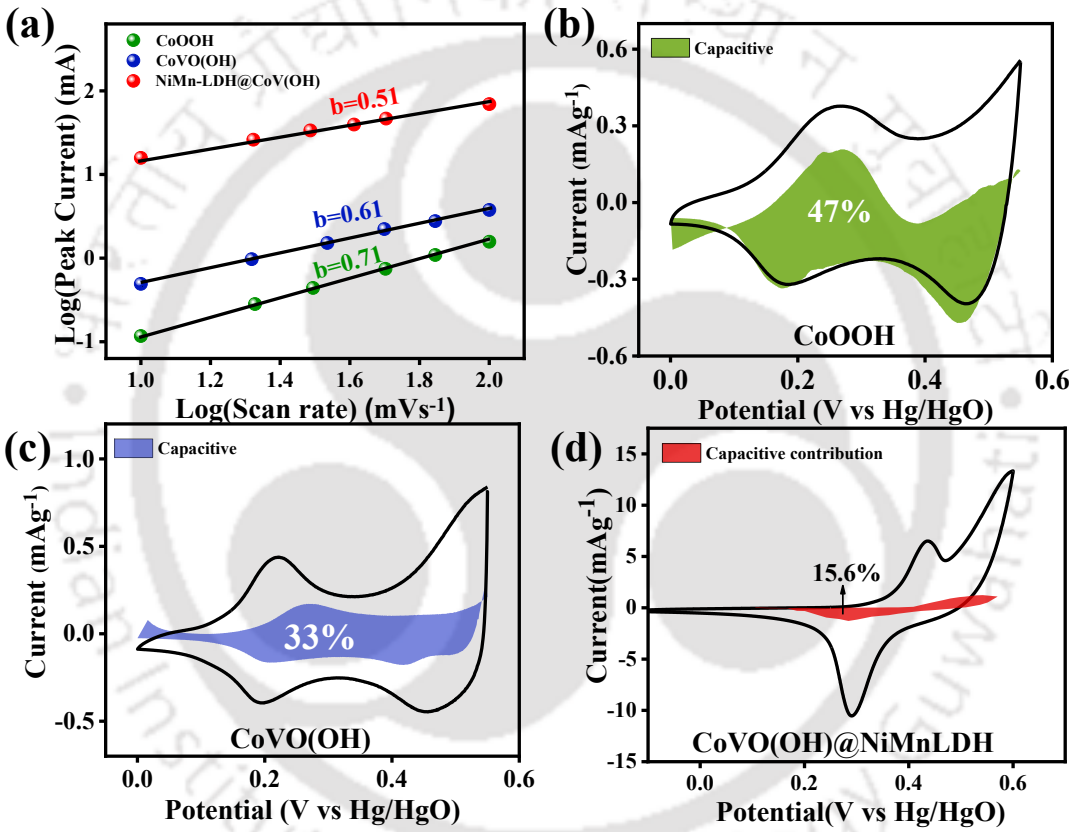

Figure 3.8: (a) The plot of log(*i*) *versus* log(*v*) of CoOOH, bare COV, NiMn-LDH@ CoVO(OH) comparison of capacitive and diffusive controlled contribution in cyclic voltammetry curve at scan rate of 5 mVs^{-1} for (b)CoOOH (c) COV (d) NiMn-LDH@COV, respectively.

To analyse the contribution of redox process vs diffusion, during the charging process and to determine the capacitive behaviour, the value of "*b*" was determined from the CV plots at different scan rates according to the given Eq. ($i=aV^b$). In general, when the value of *b* is equal to 0.5, the electrode materials show battery-like characteristics and for the range of 0.5–1, the electrode materials show capacitance contribution and

diffusion-controlled contribution characteristics. In **Figure 3.8a**, the fitted *b* value of the anodic peak current for CoO(OH) is found to be 0.71. This value decreases to 0.61 after the incorporation of high-valent vanadium, indicating enhanced redox activity. Furthermore, the b value for the composite is 0.51, suggesting battery-type behavior, which is consistent with the CV and GCD analyses. The percentage contributions from capacitive and diffusion-controlled processes in CoO(OH), COV, and NiMn-LDH@COV electrodes at a scan rate of 5 mVs^{-1} were determined using Dunn's method. Based on this analysis, the capacitive contribution decreases from 47% for bare CoO(OH) to 33% after vanadium incorporation, and further drops to 15.6% upon forming the composite with NiMn-LDH, as illustrated in **Figures 3.8(b-d)**. This result indicates a the redox activity CoO(OH) increases as the Vanadium is incorporated and further increases with the composite formation of NiMn-LDH, which is contributing to the battery-type pseudocapacitance charge storage.

3.3.8 Asymmetric Device:

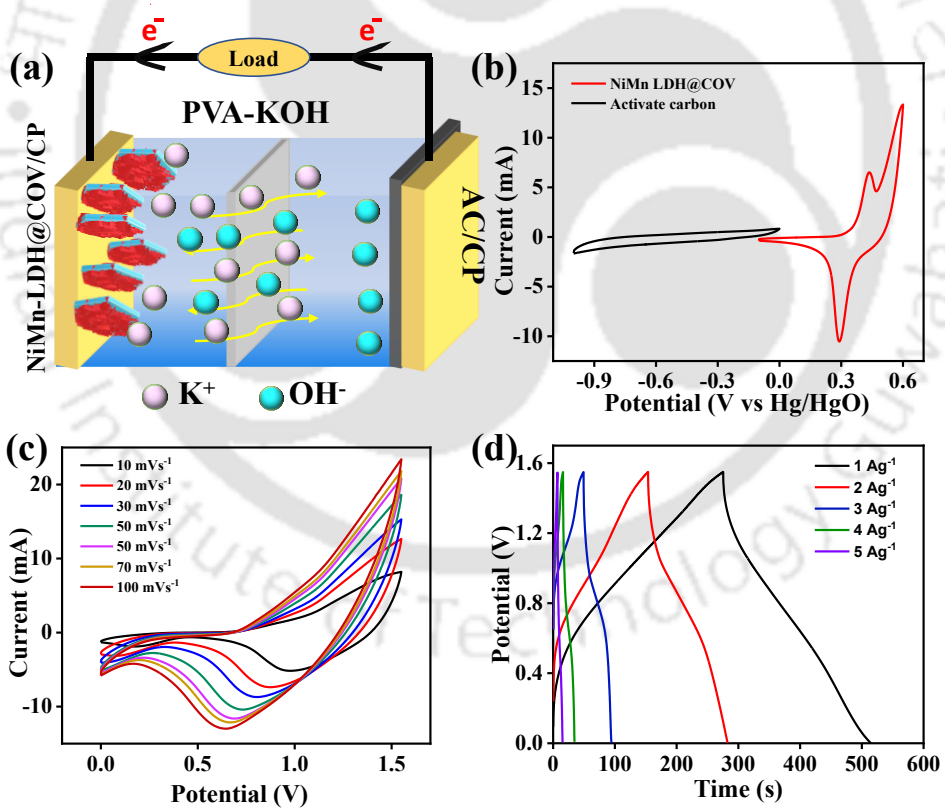

Figure 3.9: :(a) Schematic presentation of ASC tested (b) CV curves of AC and NiMn-LDH@COV/CP electrodes in a three-electrode system with a scan rate of 10 mV s^{-1} (c) CV curve of NiMn-LDH@COV/CP//AC at different scan rate (10-100mV s^{-1} in a two-electrode system) (d) GCD curve in two electrode system at a different current density.

To demonstrate the practicality of the composite material, an asymmetric supercapacitor (ASC) device was constructed with NiMn-LDH@COV/CP as the positive electrode and Activated Carbon (AC) deposited over carbon paper as the negative electrode in 1M PVA-KOH gel electrolyte separator **(Figure 3.9a)**. **Figure 3.9b** represents the CV of AC and composite NiMn-LDH@COV/CP in a three-electrode system, indicating the AC electrode operates in the negative potential range (0 to −1 V), while the NiMn-LDH@COV/CP electrode functions within -0.1 to 0.55 V. This complementary behavior enables an extended operating voltage window of 1.55 V in the asymmetric NiMn-LDH@COV/CP //AC device. **Figure 3.9c** illustrates the CV curves at different scan speeds of the constructed device, indicating the stable operating voltage window of ASC is 0–1.55V. As the scan speed increases, the CV curve profiles remain stable, indicating that the electrode has an outstanding rate capability. Two distinct electrode behaviours, such as an EDLC-type AC and a battery-type NiMn-LDH@COV electrode, are combined and coexist in a balanced manner, as shown by a semi-redox feature in the CV profile. **Figure 3.9d** presents the GCD curve of the ASC device obtained at different current densities (1 to 10 Ag^{-1}) to validate its high efficiency. GCD profile revealed a mixed voltage variation mechanism with a linear variation due to AC and a non-linear variation due to battery type NiMn-LDH@COV and the nearly symmetric charge-discharge profile with minimal IR drop indicates high efficiency. The specific capacitance value obtained at 1A g^{-1} is 147 F g^{-1}, confirming the potential of the composite material to be utilized for practical purposes.

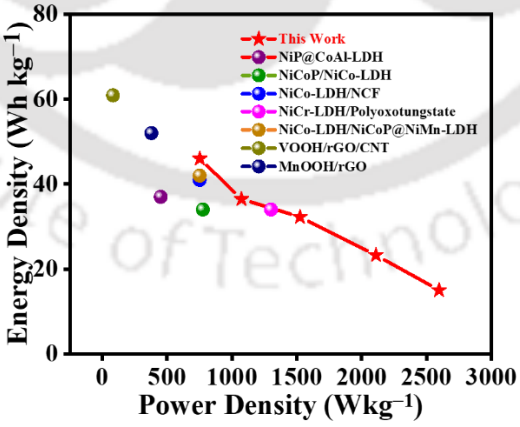

Figure 3.10: Ragone plots related to the energy and power densities.

Furthermore, the Ragone plot of the NiMn-LDH@COV//AC hybrid supercapacitor clarifies the relationship between the energy and power density, as shown in **Figure 3.10**. The energy density and power density of the fabricated device were calculated to be 46 Wh kg^{-1} and 752W

kg^{-1}, at 1 Ag$^{-1,}$ respectively. The hybrid supercapacitor still retained an energy density of 15 W h kg^{-1}, which is superior to that of most of the recently reported devices based on Oxyhydroxide and LDH-based asymmetric supercapacitor devices.[25-31]

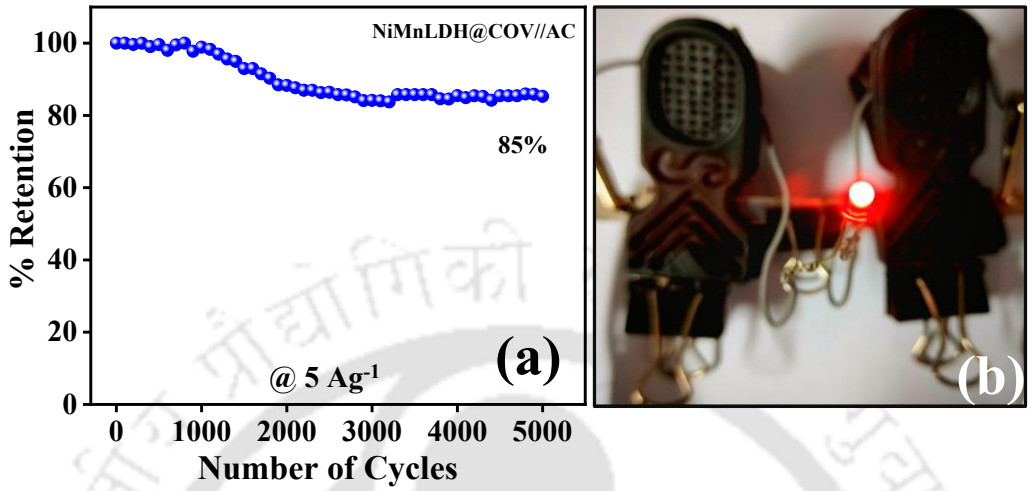

Figure 3.11: (a) long-term cyclic performance of the asymmetric supercapacitor device at 5Ag^{-1} using PVA-KOH electrolyte (b) Digital photograph of LEDs powered by two asymmetric supercapacitor device devices in series connection.

We have also performed 5000 GCD cycles for the asymmetric device, which is showing 85% capacitance retention at 5 Ag^{-1} in 1.5M PVA-KOH gel electrolyte (**Figure 3.11a**). Note that the concentration of electrolyte in the cyclic retention measurements is higher to balance the loss of electrolyte during the device operation. The practical utility of the composite material was demonstrated by utilizing two ASC devices, connected in series, to power an LED light of 3V, as shown in **Figure 3.11b**. Upon charging the devices to 3V, the LED light initially glowed intensely and later gradually dimmed through the discharging process.

3.3.9. Probable mechanism of charge storage:

The pseudo-capacitive behavior of the composite material NiMn-LDH@COV/CP is mainly ascribed to the Faradaic processes of the constituent elements, i.e., the redox cycles in the given potential window. In the potential range of -0.1 V to 0.6 V vs. Hg/HgO reference electrode, the Co, Ni and Mn ions are electrochemically active as all the ions showed both the oxidation and reduction peaks. In the COV, Co ion undergoes the redox reaction contributing to the pseudo-capacitive behaviour, whose activity was enhanced on incorporation of spectator V^{5+} ion to form the bi-metal oxyhydroxide. V^{5+} participates as the spectator ion as it is not showing any

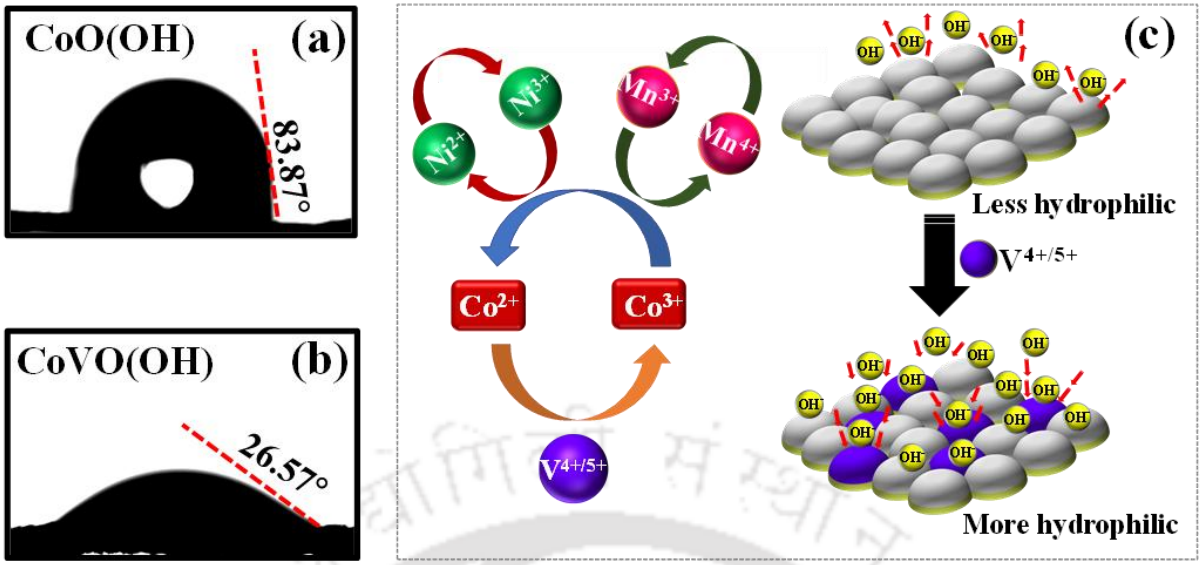

Figure 3.12: Contact-angle measurements of (a) CoO(OH) (b) CoVO(OH) indicating increasing hydrophilicity with incorporation of high valent vanadium (c) Schematic representation of the plausible mechanistic pathway involving the contribution of spectator ion vanadium along with the redox-active ions such as Cobalt, Nickel, and Manganes.

redox behaviour. Also, the V-ion in high oxidation state is known to reduce the adsorption energy of the OH^- ions due to the increased hydrophilicity, confirmed by contact angle measurement **(Figure 3.12 (a,b))**, thus increasing the flux of electrolyte ions into the electrode active sites, thereby increasing the redox capacity of the composite, COV.[32] Further, V^{5+} due to its high oxidation state-induced polarization in the Co – O bond, thereby affecting the oxidation state of cobalt, promoting its Co^{2+}/ Co^{3+} conversion faster, which was also confirmed by XPS. Enhancement in specific capacitance upon deposition of NiMn-LDH is due to the additional redox cycles of Ni (Ni^{2+}/Ni^{3+}) and Mn ($Mn^{3+/}Mn^{4+}$) ions in the composite material. The probable mechanism of storing charge at the electrode/electrolyte interface is given in **(Figure 3.12c)**. Thus, the redox-cycles within the potential window of the composite material, NiMn-LDH@COV, are mutually responsible for the obtained high specific capacitance. Additionally, the 2D nature of the LDH molecule enlarges the active surface area (confirmed from BET analysis) of the composite material, thereby increasing the electroactive sites and facilitating the efficient Faradaic processes of a pseudo-capacitor.

3.4. CONCLUSIONS:

In conclusion, COV hexagonal plates as the core and bimetallic NiMn-LDH nanosheets as the shell were successfully prepared through a simple hydrothermal reaction to synthesize NiMn-LDH@COV/CP composite. The prepared NiMn-LDH@COV/CP has a large specific surface area, which can greatly increase the number of surface-active sites and increase the contact area between the electrode and the electrolyte. At the same time, incorporation of high valent V ion induces more hydrophilicity, promoting the adsorption of the electrolyte/hydroxyl ions on the surface of COV, thereby increasing the redox cycles of Co ion. Further utilization of NiMn-LDH over the surface of CoVO(OH) proved to be a successful strategy in the development of an efficient pseudo-capacitor material. The overall effect of redox cycles of Ni and Mn ions, in addition to that of the Co ions, generated a capacitance value of 786 Cg^{-1} at a current density of $1Ag^{-1}$ with a capacitive retention of 96% upon 5000 GCD cycles, confirming its high activity and durability.

Authors Contribution:

Alpana Sahu conceptualized and performed all the experiments. Alpana Sahu, Peeyush Pandey and Sourav Bhowmick were involved in evaluating the results and manuscript writing. Prof. Mohammad Qureshi overall coordinated for the funding, experiments and manuscript writing.

3.5. REFERENCES:

1. C. Liu, F. Li, L.-P. Ma, H.-M. Cheng, *Advanced Materials* **2010**, 22, E28.
2. S. L. Candelaria, Y. Shao, W. Zhou, X. Li, J. Xiao, J.-G. Zhang, Y. Wang, J. Liu, J. Li, G. Cao, *Nano Energy* **2012**, *1*, 195.
3. Z. Liu, Y. Qiu, L. Cui, R. Zheng, W. Yang, C. J. Barrow, J. M. Razal, J. Liu, *Carbon N Y* **2022**, *189*, 81.
4. M.-S. Balogun, Y. Huang, W. Qiu, H. Yang, H. Ji, Y. Tong, *Materials Today* **2017**, *20*, 425.
5. W. Long, B. Fang, A. Ignaszak, Z. Wu, Y.-J. Wang, D. Wilkinson, *Chem Soc Rev* **2017**, *46*, 7176.
6. Y. Lu, L. Li, D. Chen, G. Shen, *J Mater Chem A* **2017**, *5*, 24981.
7. Q. Chen, Y. Zhao, X. Huang, N. Chen, L. Qu, *J Mater Chem A* **2015**, *3*, 6761.
8. P. Simon, Y. Gogotsi, B. Dunn, *Science (1979)* **2014**, *343*, 1210.
9. T. S. Mathis, N. Kurra, X. Wang, D. Pinto, P. Simon, Y. Gogotsi, *Adv Energy Mater* **2019**, *9*, 1902007.
10. O. Moradlou, H. Ansarinejad, M. Hosseinzadeh, H. Kazemi, *J Alloys Compd* **2018**, *755*, 231.

11. L. Zhang, Q. Ding, Y. Huang, H. Gu, Y.-E. Miao, T. Liu, *ACS Appl Mater Interfaces* **2015**, *7*, 22669.
12. M. Chen, Y. Zhang, Y. Liu, Q. Wang, J. Zheng, C. Meng, *ACS Appl Energy Mater* **2018**, 8b01109.
13. J. Theerthagiri, K. Karuppasamy, C. Justin Raj, G. Maia, M. L. Aruna Kumari, L. John Kennedy, M. K. R. Souza, E. S. F. Cardoso, S. Kheawhom, H.-S. Kim, M. Y. Choi, *Coord Chem Rev* **2024**, *513*, 215880.
14. W. Li, J. Huang, L. Feng, L. Cao, Y. Feng, H. Wang, J. Li, C. Yao, *J Mater Chem A* **2017**, *5*, 20217.
15. Y. Yu, Y. Tan, B. Yang, L. Yuan, X. Shen, X. Hu, *J Power Sources* **2019**, *443*, 227278.
16. J. Hao, W. Wu, Q. Wang, D. Yan, G. Liu, S. Peng, *J Mater Chem A* **2020**, *8*, 7192.
17. C. Justin Raj, B. C. Kim, W.-J. Cho, S. Park, H. T. Jeong, K. Yoo, K. H. Yu, *Journal of Electroanalytical Chemistry* **2015**, *747*, 130.
18. Y. Zhang, L. Li, H. Su, W. Huang, X. Dong, *J Mater Chem A* **2015**, *3*, 43.
19. S. C. Lee, M. Kim, J.-H. Park, E. S. Kim, S. Liu, K. Y. Chung, S. Chan Jun, *J Power Sources* **2021**, *486*, 229341.
20. A. Jouhara, N. Dupré, A.-C. Gaillot, D. Guyomard, F. Dolhem, P. Poizot, *Nat Commun* **2018**, *9*, 4401.
21. J. Yu, Q. Wang, D. O'Hare, L. Sun, *Chem Soc Rev* **2017**, *46*, 5950.
22. C. Qu, B. Zhao, Y. Jiao, D. Chen, S. Dai, B. M. deglee, Y. Chen, K. S. Walton, R. Zou, M. Liu, *ACS Energy Lett* **2017**, *2*, 1263.
23. C. T. Moi, S. Bhowmick, M. Qureshi, *ACS Appl Mater Interfaces* **2021**, *13*, 51151.
24. H. Liang, J. Lin, H. Jia, S. Chen, J. Qi, J. Cao, T. Lin, W. Fei, J. Feng, *J Mater Chem A* **2018**, *6*, 15040.
25. M. Chen, Y. Zhang, Y. Liu, Q. Wang, J. Zheng and C. Meng, *ACS Appl. Energy Mater.,* 2018, 5527−5538.
26. S. Sun, S. Wang, T. Xia, X. Li, Q. Jin, Q. Wu, L. Wang, Z. Wei and P. Wang, *J. Mater. Chem. A*, 2015, 3, 20944.
27. S. Wang, Z. Huang, R. Li, X. Zheng, F. Lu and T. He, *Electrochim. Acta*, 2016, 204, 160.
28. X. Li, H. Wu, A. M. Elshahawy, L. Wang, S. J. Pennycook, C. Guan and J. Wang, *Adv Funct. Mater.,* 2018, 28, 1800036.
29. Y. Liu, Y. Wang, C. Shi, Y. Chen, D. Li, Z. He, C. Wang, L. Guo and J. Ma, *Carbon*, 2020, 165, 129.
30. N. S. Padalkar, S. v. Sadavar, R. B. Shinde, A. S. Patil, U. M. Patil, D. S. Dhawale, R. N. Bulakhe, H. Kim, H. Im, A. Vinu, C. D. Lokhande and J. L. Gunjakar, *J. Colloid Interface Sci.*, 2022, 616, 548.
31. H. Liang, J. Lin, H. Jia, S. Chen, J. Qi, J. Cao, T. Lin, W. Fei and J. Feng, *J. Mater. Chem. A*, 2018, 6, 15040.
32. J. Liu, Y. Ji, J. Nai, X. Niu, Y. Luo, L. Guo, S. Yang, *Energy Environ Sci* **2018**, *11*, 1736.

CHAPTER 4

Capacitive–Diffusion Interplay: Redox-active $Mn_2V_2O_7$ rods integrated with MXene sheets for enhanced charge transfer

A synergistic approach combining capacitive and redox-active materials is employed to develop supercapacitors that effectively bridge the gap between traditional supercapacitors and batteries in terms of their high-power delivery and increased energy density. Here, we have reported MXene with manganese vanadium oxide ($Mn_2V_2O_7$) nanorods to eliminate the limitations, such as restacking of MXenes, which poses a major problem in achieving high conductivity to be used in supercapacitor applications. Formation of pathways for ion migration in $Mn_2V_2O_7$/MXene composite, resulting in increased conductivity, enhanced ion transport capacity and structural stability in aqueous electrolytes leading to superior performance.

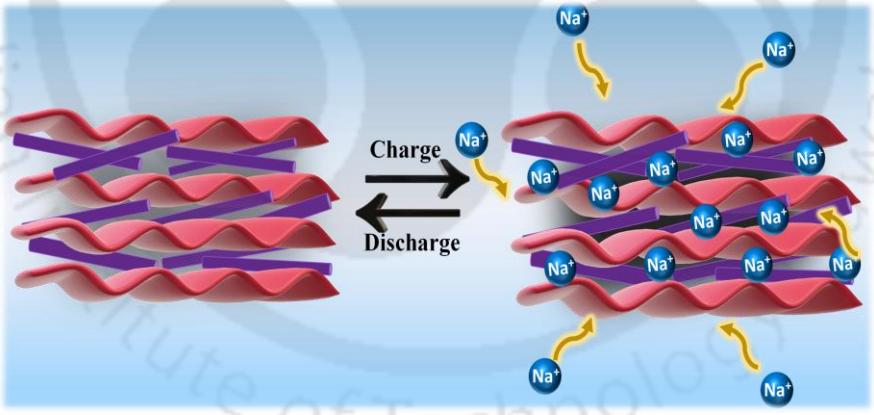

Part of this manuscript has been published in ***Appl. Energy Mater.*** **2024, 15, 6062**

4.1. INTRODUCTION:

Supercapacitors (SCs) have gained–attention over other electrochemical energy storage devices because of their advantages, such as their remarkable energy storage, rapid rate of charge and discharge, and durable cycle performance.[1] Depending on how they store energy, supercapacitors can be categorized as either EDLCs or pseudocapacitors. The charge storage mechanism in EDLC is characterized by the physical adsorption and desorption of charges near the electrode material's surface. In contrast, pseudocapacitors operate through a redox reaction, involving chemical adsorption and desorption on the electrode material's surface, accompanied by electron transfer.[2–5] A recent advancement in energy storage technology is the hybrid supercapacitor battery, harnessing the combined strengths of both supercapacitors and batteries.[6] Research focuses on developing electrode materials with improved energy and power density, cycling stability, and charging/discharging capabilities, often utilizing carbon-based materials and transition metal oxides. This dynamic field promises advancements in flexible and sustainable supercapacitor applications.[7,8]

A significant focus on transition metal oxides (TMOs) due to their exceptional charge-storing capabilities and the ability to tailor micro/nanostructures. Recently, nanostructured materials are highly efficient electrode materials for energy storage devices as they have high surface energy. The elevated surface activity and increased electroactive sites of one-dimensional(1D) materials result in high carrier capacity in addition to providing electron–ion conduction pathways with shorter diffusion lengths. Layered binary metal vanadates have become a group of promising electrode materials for SCs because of their collaborative interaction between vanadium and other metal elements (e.g., CaV_4O_9, Fe_2VO_4, ZnV_2O_4), exhibit synergistic effects that boost ion conductivity and contribute to increased reversible capacities.[9–11] Due to their substantial interlayer spacings, which facilitate rapid ion diffusion channels, these materials have emerged as promising candidates for energy storage electrodes.[12] $Mn_2V_2O_7$, also known as manganese pyrovanadate, features a distinct distorted honeycomb atomic arrangement.[13,14] This structure consists of edge-sharing MnO_6^- octahedra forming layers shared with V_2O_7 groups, resulting in a staggered configuration with linear bridging V-O-V bonds. The β-$Mn_2V_2O_7$ phase showcases honeycomb layers of Mn^{2+} cations separated by VO_4^- groups, allowing for valence state conversion, and contributing to electrochemical energy storage. Despite these advantages, the poor electrical conductivity of manganese and vanadium oxide-based electrodes hampers device performance. To address

this, integrating manganese vanadium oxide composites with highly conductive carbonaceous networks, such as MXene, graphene, or carbon nanotubes, can significantly enhance the overall properties. MXenes are 2D materials, such as Titanium carbide ($Ti_3C_2T_x$), which exhibit excellent pseudocapacitive properties. However, the electrochemical performance of MXene diminishes due to the restacking of sheets of MXene.[15,16] The hindrance caused by stacking impedes the out-of-plane electron transport and increases the distance of ion diffusion within the electrode, ultimately decreasing the electrochemical performance. However, 1D@2D binary transition-metal-oxides/MXene heterostructure materials help in interfacial interaction and improve the overall electrochemical performance. This approach also provides multi-valence rich electroactive sites thereby overcoming the individual shortcomings of the materials of the system.

In this report, we present a simple approach for the straightforward synthesis of $Mn_2V_2O_7$ (MVO) with $Ti_3C_2T_x$ MXene through a hydrothermal method. From the electrochemical measurements, the value of specific capacitance of the MVO/MXene composite was found to be 627F g^{-1} @ 1 A g^{-1} current density with a potential window of 1.0 V To get insight into the kinetic process occurring within the electrodes, we have used DRT to analyse complex impedance spectra and differentiate electrode kinetics based on their relaxation time constant. To evaluate practicality, we constructed an asymmetric supercapacitor device (ASC) with MVO/MXene as the cathode and AC as the anode. The MVO/MXene//AC configuration exhibits remarkable energy storage capabilities, featuring a specific capacitance of 192 F g^{-1} at a current density of 1 A g^{-1}, along with a specific energy density of 65 Wh kg^{-1} and a power density of 1000 W kg^{-1}.

4.2. EXPERIMENTAL SECTION:

4.2.1. Synthesis of MXenes ($Ti_3C_2T_x$):

2D Titanium carbide nanosheets were synthesized by exfoliation of commercially available Ti_3AlC_2 (Merck). The Ti_3AlC_2 powder was treated with 40 % aqueous HF solution for 24 h at 40 ˚C temperature. The resultant suspensions were washed with 5 M HCl solution for 3 times, then with deionized water and ethanol multiple times till the pH of the suspension reached ~6. The clay-like product obtained was subjected to delamination into individual MXene nanosheets through one hour of bath sonication under an argon atmosphere while ensuring the bath temperature stayed below 30°C. Subsequently, the mixture underwent centrifugation at 3500 rpm for 1 hour to gather the delaminated MXene.

4.2.2. Synthesis of $Mn_2V_2O_7$/MXenes composite:

For the preparation of $Mn_2V_2O_7$/MXenes, different concentrations of the MXene (20 mg ml^{-1}) is dispersed in 15 mL of an aqueous solution containing 3 mM of $(CH_3COO)_2Mn.\ 4H_2O$ by ultrasonication for 20 min. To allow impregnation of the MXene to Mn solution, the suspension was put for 30 min under magnetic stirring. A 15 mL aqueous solution containing 3 mM NH_4VO_3 with different concentrations of CTAB (0, 2 mM), was then gradually added to the agitated suspension at 80 °C. This mixture was stirred for 30 min and then for a hydrothermal reaction at 180 °C for 12 h. Then, the product was washed, filtered, and vacuum-dried at 80 °C for approximately 10 h.

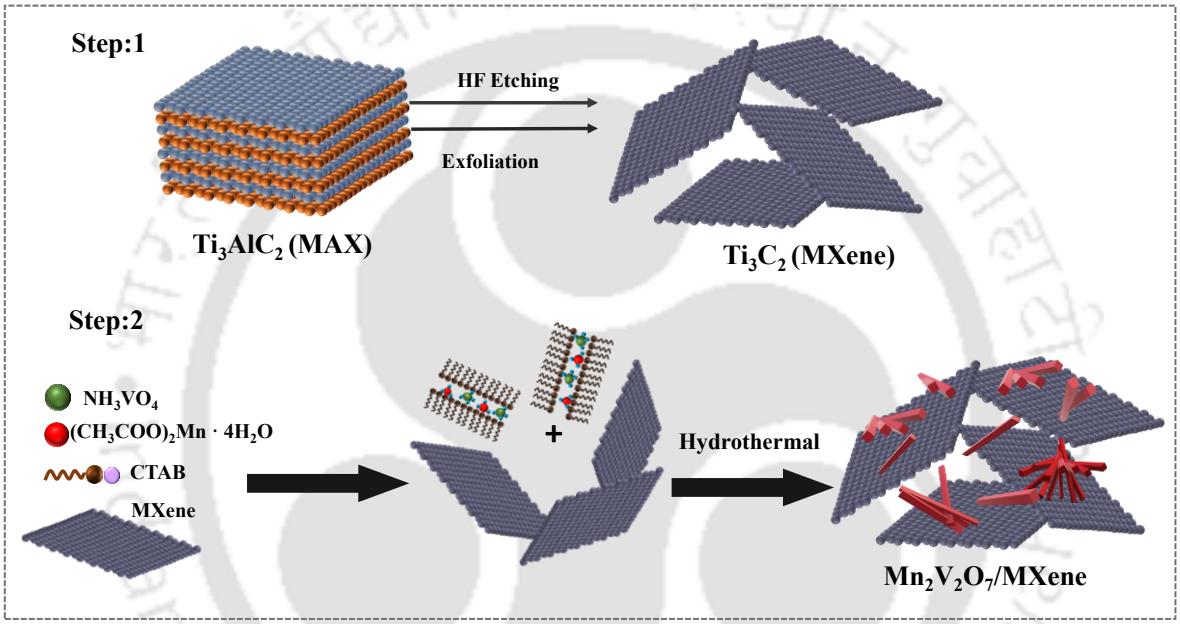

Scheme 4.1: (a) Schematic of synthesis procedure in 2 steps, etching and delamination MAX phase to form MXene (Step 1) and hydrothermal synthesis of $Mn_2V_2O_7$/MXene composite (Step 2)

4.3. RESULTS AND DISCUSSION:

4.3.1. Phase and Structural Analysis

The crystal structure and purity of different phase compositions for the prepared MXene, MVO, and MVO/MXene were examined by X-ray diffraction (XRD) analysis **Figure 4.1a** displays the XRD patterns of Ti_3AlC_2 and $Ti_3C_2T_x$ where the characteristic peaks of Ti_3AlC_2 are observed at 9.5°, 19.1°, 34°, 38.8°, 41.7°, and 60.2°, aligning with previously reported data.[17] Following the etching process, the Ti_3AlC_2 peaks disappear, with new peaks appearing at 7.57°, 29.5°, and 60.8°, while the characteristic $Ti_3C_2T_x$ peak is observed at 7.57°, indicating phase

transformation. **Figure 4.1b** shows diffraction peaks aligned to the monoclinic phase of standard literature (JCPDS Card no. 73–1806) of the MVO material. The emergence of the (002) peak of MXene along with MVO peaks in the hybrid of MVO/MXene suggests the formation of composite material. The (002) plane of MXene is observed at 7.1°, which is further left-shifted from the bare MXene, indicating an expansion in interlayer spacing attributable to the inclusion of MVO within the MXene layers.

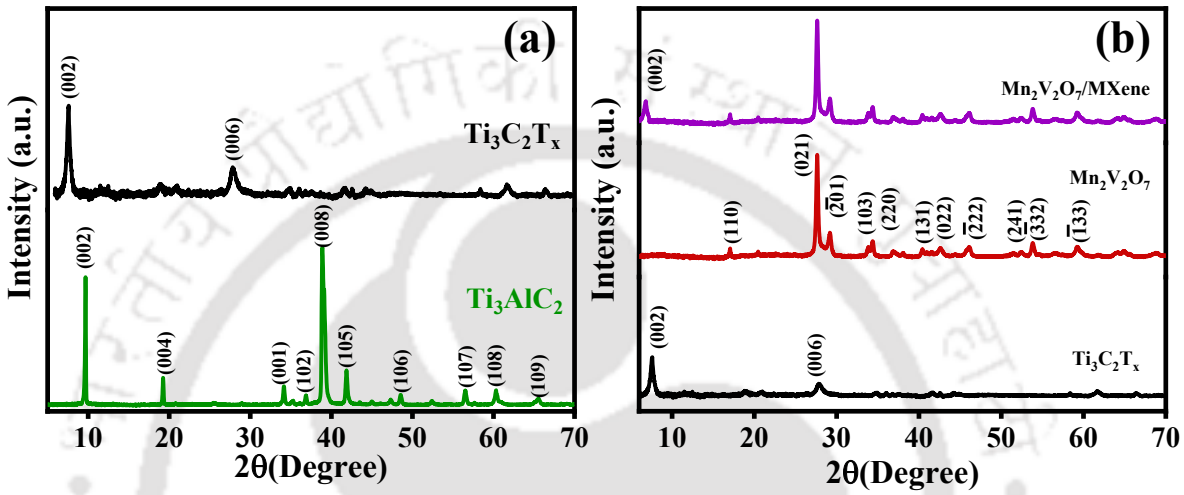

Figure 4.1: Powder XRD of (a)Ti_3AlC_2 phase(green) and $Ti_3C_2T_x$ (Black), (b)$Mn_2V_2O_7$ (Maroon), $Mn_2V_2O_7$/MXene (purple)

4.3.2. Morphological Analysis:

The morphology of the synthesized material was examined using a FESEM analysis. MAX phase shows the dense, layered structure with tightly stacked layers and after selective etching of the Al-layer, the structure evolves into a delaminated, accordion-like morphology of MXenes as shown in **Figure 4.2(a,b)** respectively. The FESEM images of the MVO samples are presented, illustrating variations in morphology in response to the usage of CTAB. In the absence of CTAB, MVO exhibited aggregated brick-like structures, approximately 400 nm in size (**Figure 4.2c**). However, upon the introduction of CTAB, the MVO morphologies transformed into elongated bundled nanorods, with diameters ranging from 20 to 50 nm, as depicted in **Figure 4.2d**. The surfactant CTAB serves as a structure-directing agent, playing a crucial role in governing the nucleation and growth of the samples. CTAB is helpful to decrease the surface tension of the solution, thereby lowering the energy needed for the formation of a new phase. CTAB is an ionic compound that completely ionizes into CTA^+ with a long hydrophobic tail, whereas Mn and V precursors get hydrolyzed to form corresponding growth

units of Mn and V hydroxylate ion pairs. There will be a coulombic attraction between the oppositely charged CTA^+ and metal hydroxylate.

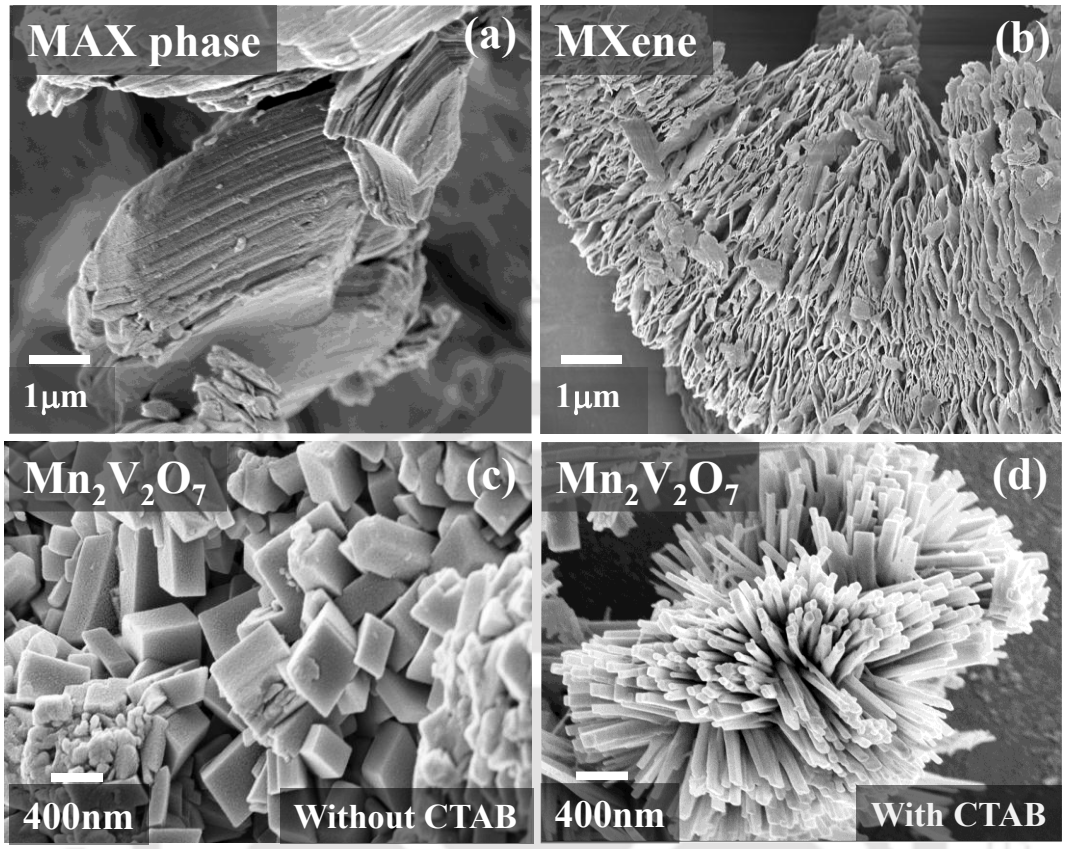

Figure 4.2: FESEM image of (a) Ti_3AlC_2 before etching showing a bulk layered structure (b) $Ti_3C_2T_x$ after etching, indicating the delaminated layered structure, FESEM image of $Mn_2V_2O_7$ (c) Without use of CTAB, (d) With use of CTAB.

As the surfactant molecules depart, $Mn–V–OH^-$ is carried away in the form of ion pairs. Throughout the crystallization process, surfactant molecules function as both growth controllers and agglomeration inhibitors, facilitating the formation of rod-shaped $Mn_2V_2O_7$.[18,19] The rod-shaped MVO was selected for further analysis in electrochemical energy storage applications, as its reduced size offers a higher surface area, thereby enhancing charge storage capabilities. Similarly, **Figure 4.3a** shows the FESEM image of the composite where MVO rods get channelized into the MXene sheets. Further, the composite formation was analyzed using the FETEM technique (**Figure 4.3b**), which shows the presence of MVO rods over MXene sheets. For a more detailed analysis of composite, **Figure 4.3c** displays a high-resolution transmission electron microscopy (HRTEM) image. The lattice fringes were found to exhibit an interplanar spacing of d=0.98 nm which corresponds to the (002) plane of MXene

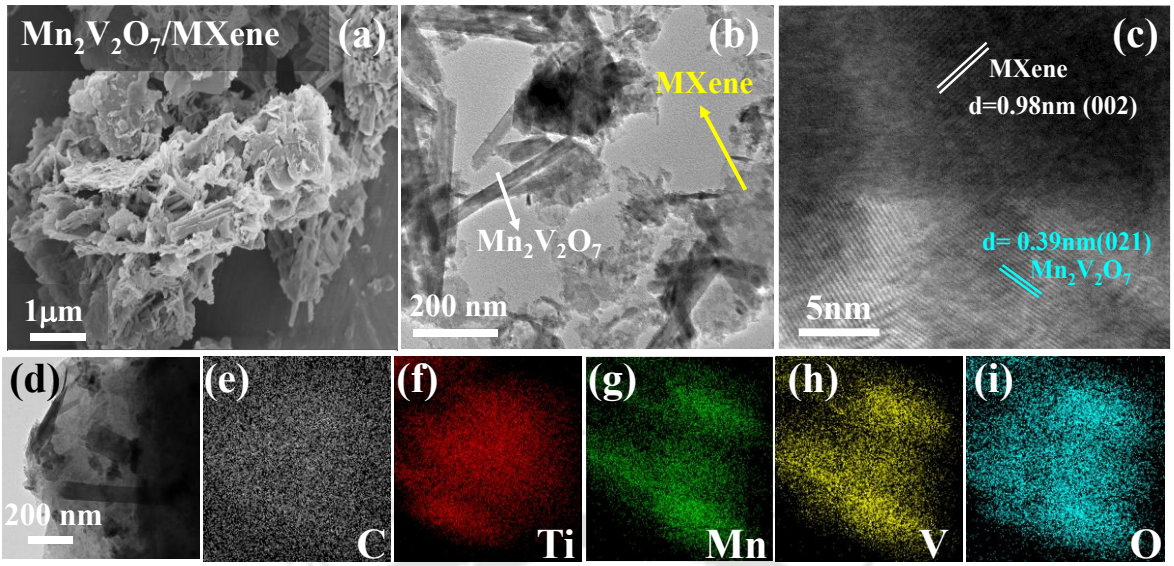

Figure 4.3: (a) FESEM and (b)FETEM image of $Mn_2V_2O_7$/MXene composite, (c) HRTEM image of $Mn_2V_2O_7$/MXene, EDS elemental mapping of $Mn_2V_2O_7$/MXene (d) showing the presence of (e) carbon (f) titanium (g) manganese (h) vanadium (i) oxygen.

and d=0.39 nm which corresponds to (021) of MVO respectively, further confirming the composite formation. The homogenous elemental distribution of Ti, C, Mn, V, and O in the composite (**Figure 4.3d**) was further visualized by HAADF-STEM characterization as shown in **Figure 4.3(e-i)**.

4.3.3. Surface area Analysis:

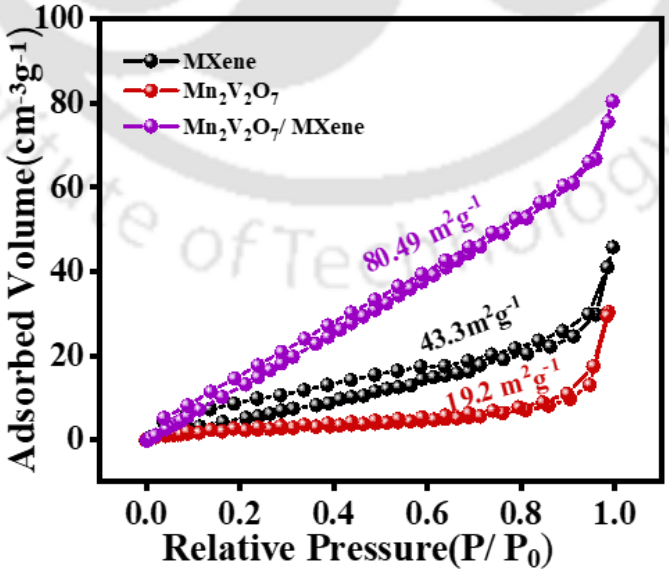

Figure 4.4: N_2 adsorption and desorption curves of MXene, $Mn_2V_2O_7$, $Mn_2V_2O_7$/MXene.

The N_2 adsorption-desorption of pristine MVO and MVO/MXene material in **Figure 4.4** reveals that, compared to pure MVO (19.2 m^2g^{-1}), the MVO/MXene had a greater BET surface area of 80.49 m^2g^{-1}. Thus, an increase in surface area provides more active sites for electrochemical reactions to occur which further facilitates charge transfer by improving ion adsorption and promoting catalytic activity.

4.3.4. Electronic State Analysis:

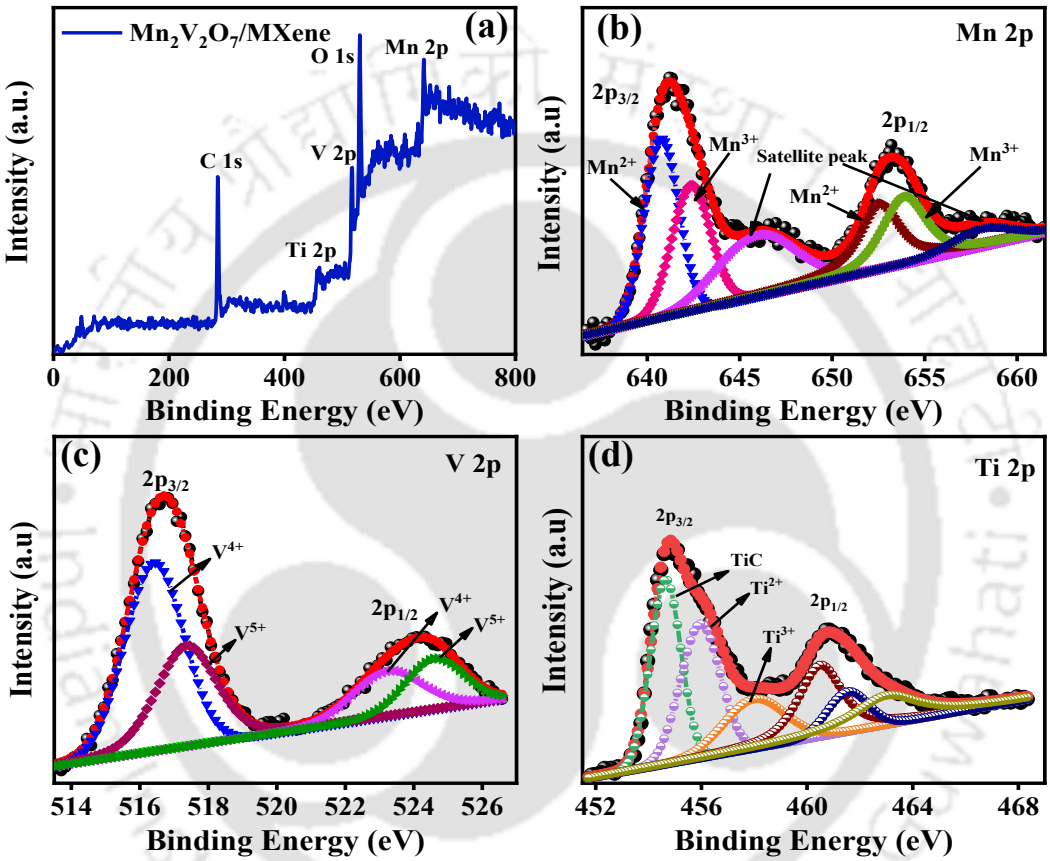

Figure 4.5: (a) XPS survey spectra, High-resolution XPS spectra of (b) Mn 2p and (c) V 2p (d) Ti 2p of MVO/MXene

X-ray photoelectron spectroscopy (XPS) was used to understand the electronic interactions among the elements present in the composite, MVO/MXene. The survey spectrum indicated the presence of Mn, V, O, Ti, and C elements **(Figure 4.5a)**. A doublet with peaks positioned at 642.5 and 654 eV is for the Mn $2p_{3/2}$ and Mn $2p_{1/2}$ respectively in **Figure 4.5b**. The binding energy separation of 11.8 eV confirms the Mn^{2+} state, and it is identified by peaks position at 653.6 and 641.8 eV, for the Mn^{3+} is confirmed by the peaks at 655.6 and 644.16 eV. In a similar manner, **Figure 4.5c** with two peaks at 516.6 eV and 524.3 eV of V 2p, represents the splitting of V $2p_{3/2}$ and V $2p_{1/2}$ states, respectively. On deconvoluting, the two peaks are arising with

oxidation states V^{4+} and V^{5+}, which confirms the multiple oxidation states of V in $Mn_2V_2O_7$. **Figure 4.5d** shows the six distinct peaks of $2p_{1/2}$ and $2p_{3/2}$ doublets observed in the Ti 2p spectra correspond to the Ti-C-T_x bonding (453.7 eV and 461.8 eV), the peaks appearing at 455.96, 459.09,462.32 and 463.8 eV can be attributed to Ti (II)-O, Ti (III)-O bonding environment. From the XPS analysis, we can conclude that redox-active Mn, V, and Ti are present in the MVO/MXene composite which can participate in pseudocapacitive charge storage.

4.3.5. Electrochemical Analyses:

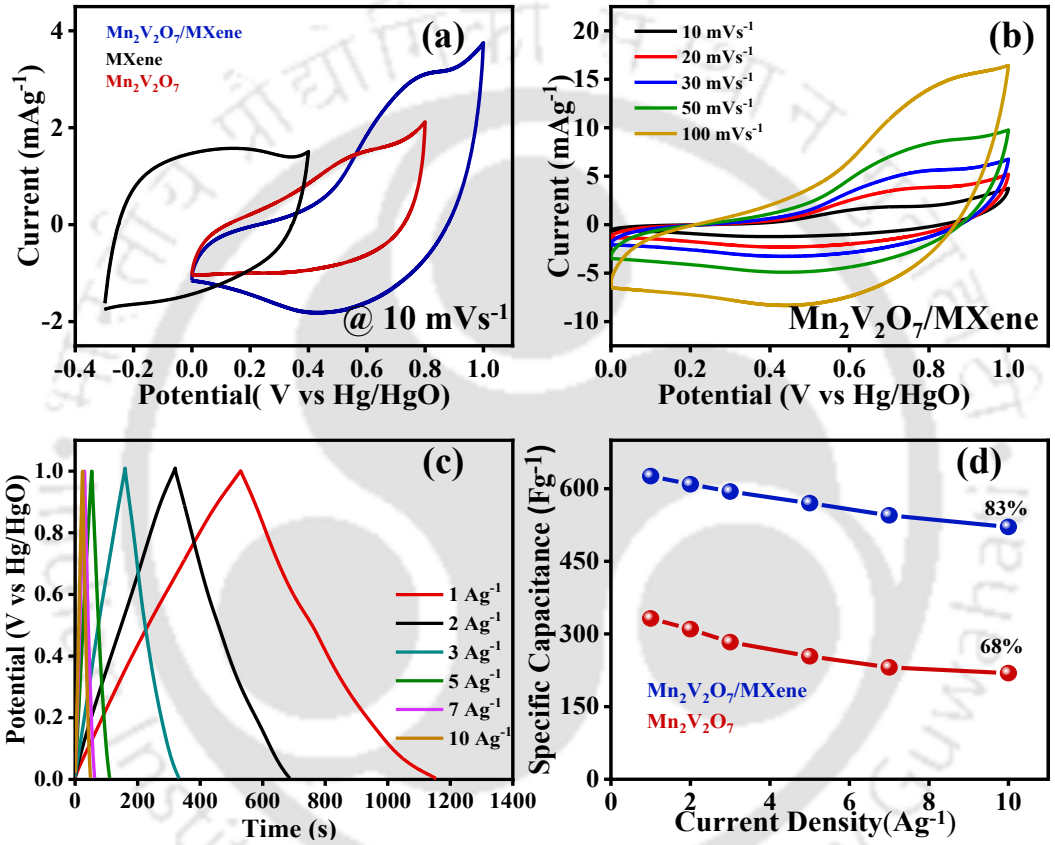

Figure 4.6: (a) Comparative CV analysis of $Mn_2V_2O_7$, MXene and $Mn_2V_2O_7$/MXene at scan rate of 10 mV s^{-1} (b) CV curves of the $Mn_2V_2O_7$/MXene electrode from 10 to 100 mVs^{-1} (c) GCD curves of the $Mn_2V_2O_7$/MXene electrode from 1 to 10 Ag^{-1} (d) Specific capacitance values of the electrodes at various current densities showing composite has a better rate capability.

To analyse the electrochemical performance of the synthesized MVO/MXene, MVO and MXene were assessed in a 1M Na_2SO_4 electrolyte solution in a three-electrode system, employing CV, GCD, and EIS. **Figure 4.6a** shows the comparison of CV curves of MXene, MVO, and MVO/MXene at different scan rate of 10 mV s^{-1} with their respective potential

window. The results indicate that compared to bare counterparts, the MVO/MXene electrode's CV curves form the larger integral areas of the closed curves, indicating the superior specific capacitive behaviour of electrode. **Figure 4.6b** shows the quasi-rectangular CV curves of the MVO/MXene electrode at various scan rates with a redox hump confirming the surface-controlled pseudocapacitive character of the composite material. Upon increasing scan rate, the current density is increasing and the redox peaks move towards higher and lower potential respectively (10 to 100 mV s^{-1}). A decrease in current values at a reduced scan rate is primarily attributed to the formation of a thicker diffusion layer on the electrode surface, which hinders the movement of electrolytes toward the electrode. Conversely, at higher scan rates, the diffusion layer is unable to expand extensively on the electrode surface which allows for increased electrolyte flux, leading to an enhancement in current.[20]

The specific capacitance of the synthesized electrode materials was determined by analysing their GCD curves at mass-normalized current densities. **Figure 4.6c** shows the GCD of the composite material where different current densities were applied with a voltage window of 0-1.0 V. The discharge profiles at different current densities indicate a decrease in discharge time, attributed to accelerated ion transfer at the electrode-electrolyte interface and reduced effective surface area utilization. The specific capacitance of the MVO/MXene and MVO electrode was obtained from the discharge profile of the GCD curve and the specific capacitance of the MVO/MXene electrode (627 Fg^{-1} and capacity 172 mA h g^{-1}) is found to be better than that of the bare MVO (332 Fg^{-1} and capacity 92 mA h g^{-1}) at 1 Ag^{-1}. We have calculated the specific capacitance at different current densities and the rate capability of the MVO/MXene composite is 83%, whereas for MVO electrode can retain 68% at 10A g^{-1} **(Figure 4.6d)**. The enhanced specific capacitance observed in the MVO/MXene composite can be attributed to the development of the formation of a well-organized matrix within the MXene. This structure facilitates enhanced ion transport by shortening the diffusion paths for ions. Additionally, the increased surface area resulting from the unique layered matrix of MXene combined with MVO enables efficient adsorption and desorption of Na^+ ions onto the surface.[21,22]

4.3.6. Electrochemical Impedance Spectroscopy (EIS) Analyses followed by Distribution of relaxation times (DRT):

To investigate interfacial charge transfer at the electrode-electrolyte interface, impedance spectroscopy analysis was conducted within the 0.1 Hz to 100 kHz range of frequency at an open circuit potential (OCP), as depicted in the Nyquist plot **(Figure 4.7a)**. The value of charge transfer resistance (R_{ct}) values was calculated by fitting the Nyquist plots to an electrical circuit. The R_{ct} value for the MVO/MXene composite (7.23 Ω) is lower, as compared to bare MVO (32.1 Ω) and MXene (29 Ω), which confirms the facile charge-transfer processes occurring at the electrode/electrolyte interface during the electrochemical reactions. Furthermore, the larger surface area of the composite provides additional active sites for electrochemical reactions, thereby facilitating rapid charge transfer.

EIS yields complex impedance data encompassing overlapping of processes such as ion transport from/to electroactive sites, ion diffusion, and charge transfer processes having different dynamics and they manifest themselves at different frequencies, which potentially allows their differentiation. However, extensive overlap in these time constants hinders the resolved interpretation of dynamic events in terms of their time scales. Utilizing the DRT methodology enables the determination of time scales required for the system to transition between equilibrium states at a specific frequency. This approach reveals distinct chemical processes aligned with various relaxation times.[23]

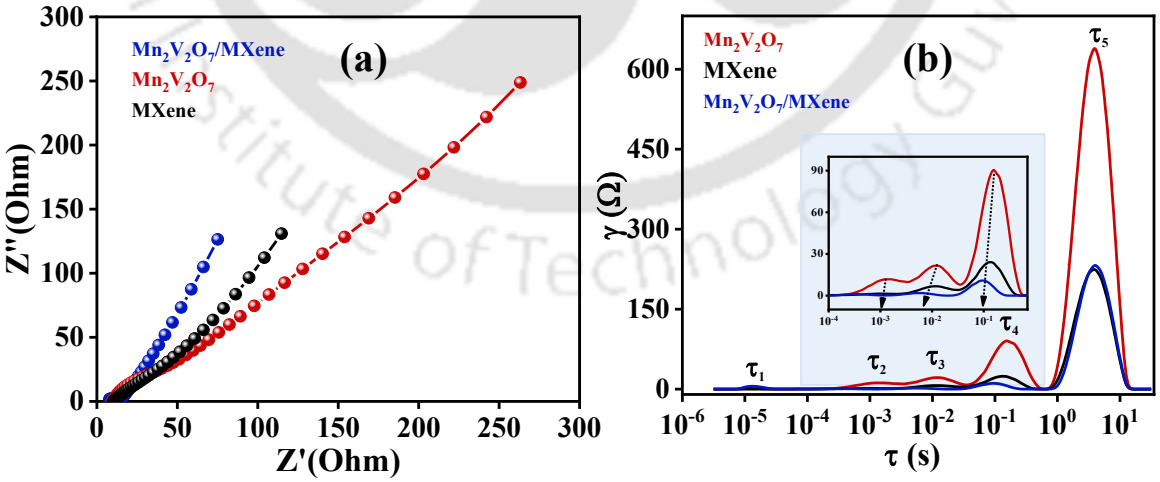

Figure 4.7: (a) Nyquist plot of all the electrodes obtained from EIS, (b) Distribution of relaxation time plot obtained from EIS (inset showing τ_2, τ_3, and τ_4 peaks)

Table 1: Represents the calculated resistance of each electrode:

System	τ_1 Resistance(Ω)	τ_2 Resistance(Ω)	τ_3 Resistance(Ω)	τ_4 Resistance(Ω)	τ_5 Resistance(Ω)
$Mn_2V_2O_7$	4.54×10^{-7}	1.8910^{-4}	0.0105	0.205	48
MXene	8.06×10^{-7}	4.78×10^{-5}	0.00142	0.17137	11.1
$Mn_2V_2O_7$/MXene	**6.5×10^{-9}**	**2.63×10^{-6}**	**1.701×10^{-5}**	**6.02×10^{-4}**	**9.8**

Figure 4.7b illustrates the DRT profile featuring four peaks labelled as τ_1 in the high-frequency region, τ_2, τ_3, τ_4 are in the intermediate frequency region, and τ_5 lie in the low-frequency region. For the composite τ_1 peak area is increasing which is ascribed to the cumulative interfacial resistance occurring either at the interface of the current collector and the material or within the layers of the material. Further, it is observed that the intensity of peaks (τ_2, τ_3, and τ_4) of MVO/MXene is notably smaller (with lower resistance values) compared to that of bare electrodes, suggesting that both the charge transfer processes are more efficient for MVO/MXene (**inset Figure 4.7b**). Further for the composite MVO/MXene the peak τ_5 resistance is 9.8 Ω which is less than bare MVO indicating faster ion diffusion within the matrix. Moreover, shifts of τ_2, τ_3, and τ_4 peaks toward the high-frequency region, along with a lower τ value, signify an improvement in the electrochemical activity of the processes. These results are further supported by the resistance values of each peak provided in Table 1. The resistance values of composite for each process are found to be lower as compared to bare MXene and $Mn_2V_2O_7$, which confirms the enhancement of the charge transfer process significantly. These findings validate that the integration of MVO into MXene constructs pathways for ion migration, promoting greater interaction between electrolyte ions and electrode surfaces. Consequently, this facilitates increased specific capacitance, significantly boosting the overall energy storage capacity of the supercapacitor.[24]

4.3.7. Charge Storage Mechanism:

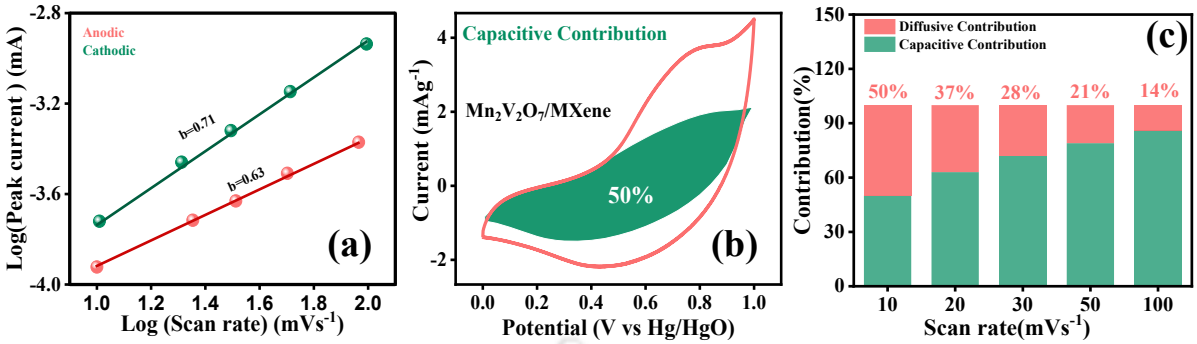

Figure 4.8: (a) Logarithmic relationship between the peak current density and scan rate, (b) Segregation of capacitive and diffusion-controlled area of $Mn_2V_2O_7$/MXene at a scan rate of 10 mVs^{-1}, (c) Segregation of both capacitive and diffusion contribution at different scan rates of the $Mn_2V_2O_7$/MXene at different scan rates (10-100 mV s^{-1}).

To evaluate the contribution of capacitive versus diffusion processes in the charging-discharging cycles, the value '*b*' was calculated from the cyclic voltammetry (CV) plots at different scan rates using the equation (5). The fitted *b* value of the anodic and cathodic peak current for MVO/MXene is found to be 0.71 and 0.63, indicating surface-controlled pseudo capacitance **(Figure 4.8a)**. We have further analyzed the contributions of capacitive and diffusion towards the total specific capacitance of MVO/MXene by using a modified power-law equation expressed in eqn.[25,26] In **Figure 4.8b**, the capacitive and diffusion-controlled regions in the CV curves of MVO/MXene at 10 mV s^{-1} are displayed, revealing a capacitive-controlled contribution of 50%. **Figure 4.8c** displays a comparative bar graph representation of the diffusive and capacitive contributions at various scan rates of 10–100 mV s^{-1}. The bar graph demonstrates that charge storage mechanism of the electrode was significantly influenced by the scan rates. With the increase in the scan speed from 10 to 100 mVs^{-1} the capacitive percent gradually increased from 50% to 86%, while the diffusive percent decreased from 50% to 14%. This suggests that at the lower scan rate electrode has adequate time to go through Faradic redox reactions, producing a greater diffusion percentage. While at the higher scan rate, the diffusion of ions is faster, it effectively imposes a time constraint on ion migration and ions choose to physically adsorb at the electrode/electrolyte interface, leading to a reduction in the diffusion contribution. Despite that, at each scan rate, a higher proportion of capacitive contribution and diffusive contribution was calculated, revealing that the physical adsorption of charges at the electrode/electrolyte interface, providing a predominantly surface-controlled-pseudocapacitive contribution to the overall electrode performance.[27,28] The

incorporation of pseudocapacitive MVO with MXene nanosheets, exhibiting characteristics like surface controlled pseudocapacitance, holds significant promise for swift intercalation/deintercalation processes and surface diffusion of Na^+ ions. The composite architecture, comprising MVO rods and MXene sheets, offers an abundance of active sites conducive to both faradaic and non-faradaic reactions.[29,30] The subsequent equations delineate the probable surface-controlled pseudocapacitive charge storage mechanisms occurring within the MVO/MXene electrode material throughout the reversible charging and discharging cycles.[31]

$$Mn_2V_2O_7 + xNa^+ + xe^- \leftrightarrow Na_xMn_2V_2O_7 \text{ (Faradic component)} \quad ....(4.1)$$

$$Mn_2V_2O_7 + xNa^+ + xe^- \leftrightarrow (Mn_2V_2O_7)^{x-} - xNa^+_{surface} \text{ (non-faradic component)} \quad ....(4.2)$$

$$Ti_3C_2T_x + xNa^+ + xe^- \leftrightarrow (Ti_3C_2T_x)\text{-}xNa^+ \text{ (faradic component)} \quad ....(4.3)$$

$$Ti_3C_2T_x + xNa^+ + xe^- \leftrightarrow (Ti_3C_2T_x)^{x-}\text{-}xNa^+_{surface} \text{ (non-faradic component)} \quad .... (4.4)$$

4.3.8. Asymmetric Device:

The asymmetric supercapacitor (ASC) was configured with activated carbon (AC) as the negative electrode, and the active material MVO/MXene as the positive electrode within a PVA-Na_2SO_4 gel electrolyte. **Figure 4.9a** depicts the assembly of the ASC device with an optimized mass ratio for both positive and negative electrodes. **Figure 4.9b** shows the operational potential window of AC was investigated in the negative potential range of -1 to 0 V through CV and MVO/MXene has a potential window of 0-1.0V and together they are giving a potential window of 2V which was employed for subsequent electrochemical analyses of the ASC assembly. **Figure 4.9c** shows the CV curves at different scan rates of the assembled device showing the stable working voltage window of 0–2.0 V and a symmetric CV profile with increasing scan speed, signify the excellent rate capability of the electrode. **Figure 4.9d** depicts the GCD tests conducted on the device across a range of current densities from 1 to 10 A g^{-1} exhibit an almost linear increase and decrease of voltage over time. Additionally, the symmetrical charging-discharging profile, without much of an iR drop, robustly underscores the exceptional electrochemical performance of the MVO/MXene//AC asymmetric supercapacitor assembly.

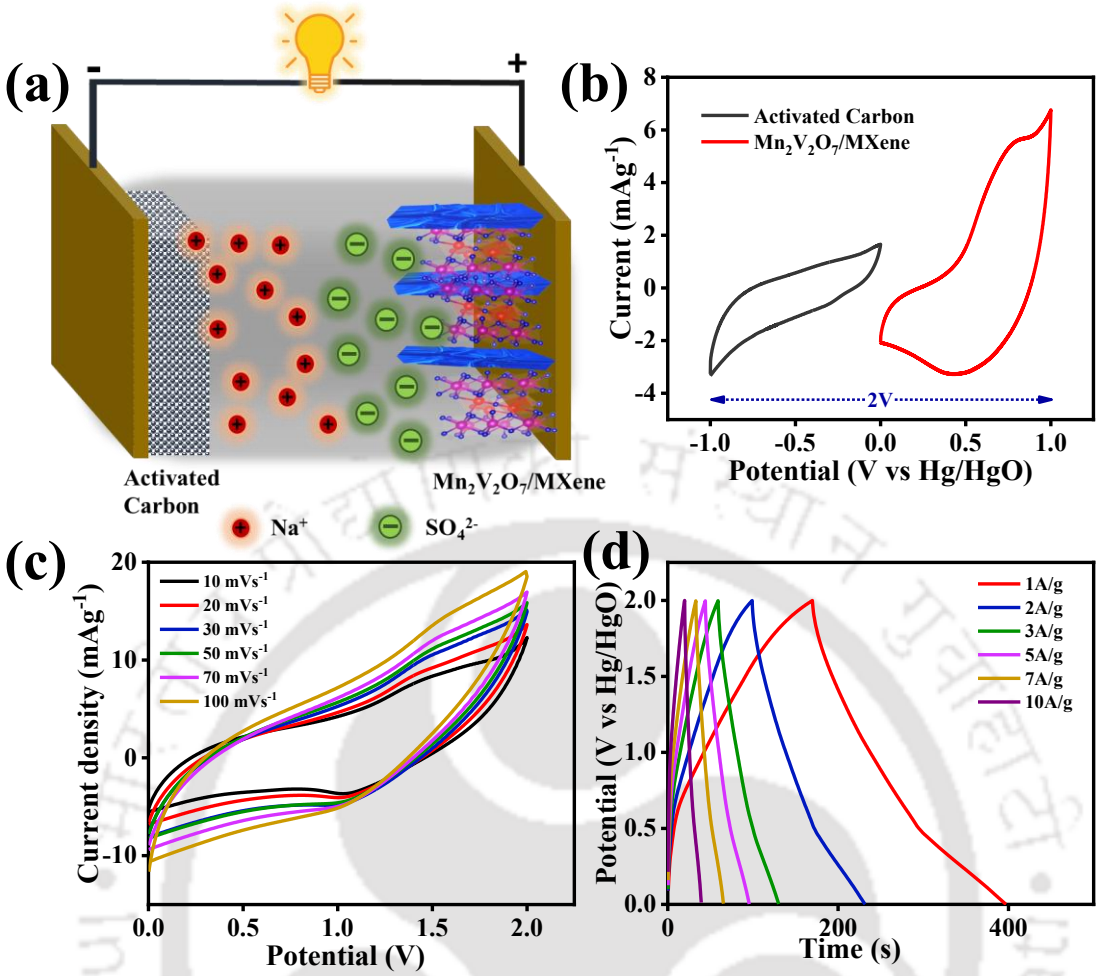

Figure 4.9: (a) Schematic presentation of the ASC tested (b) CV curves of AC and $Mn_2V_2O_7$/MXene electrodes in a three-electrode system with a scan rate of 10 mV s^{-1}. (c) CV curves of $Mn_2V_2O_7$/MXene//AC with varying scan rate 10–100 mV s^{-1}. (d) GCD curves for the two-electrode system at the indicated current densities.

The specific capacitance of ASC calculated from the GCD curves achieves a high value of 118 F g^{-1} at 1 A g^{-1}. Further, the device can give an energy density of 65 Wh kg^{-1} at a power density is 1000 W kg^{-1}. **Table 4.1**. depict the comparison table of specific energy densities and specific power densities for the MVO/MXene//AC asymmetric supercapacitor (ASC), where the energy density is superior to that of most of the previously reported devices based on MXene, and other transition metal oxide compounds.

Table 4.1: Comparative study of ASC devices with reported literatures:

Electrode material	Voltage Window (V)	Electrolyte	Energy Density (Wh kg^{-1})	Power density (Wh kg^{-1})	Reference
$Mn_2V_2O_7$/MXene//AC	**2 V**	**1M Na_2SO_4**	**65 Wh/kg**	**1000 W/kg**	**This Work**
$Mn_2V_2O_7$//AC	1.6	3M KOH	36.8	1564	32
MnO_2/MXene	0.85	0.2M KOH	29.58	749.92	33
V_2O_5–ECF//ECF	2	6M LiCl	22.3	1500	34
V_2O_5/MXene	1.2	1M H_2SO_4	20.83	374.94	35
Ni^{2+}-doped $(NH_4)_2V_3O_8$@Ni foam//AC	1.5	2 M KOH	20.1	752	36
$ZnCo_2O_4$/MXene//AC	1.6	3 M KOH	15.6	551.1	37
MXene/$NiCo_2S_4$ //AC	2	7 M KOH	72.82	635	38
Mn−V−O@C//graphene hydrogel	1.9	1M K_2SO_4	37.77	900	39
Hexagonal WO_3–Ti_3C_2	-	0.5 M H_2SO_4	9.32	960	40
1T-VS_2/MXene//MXene	1.6	1M K_2SO_4	41.13	793.50	41

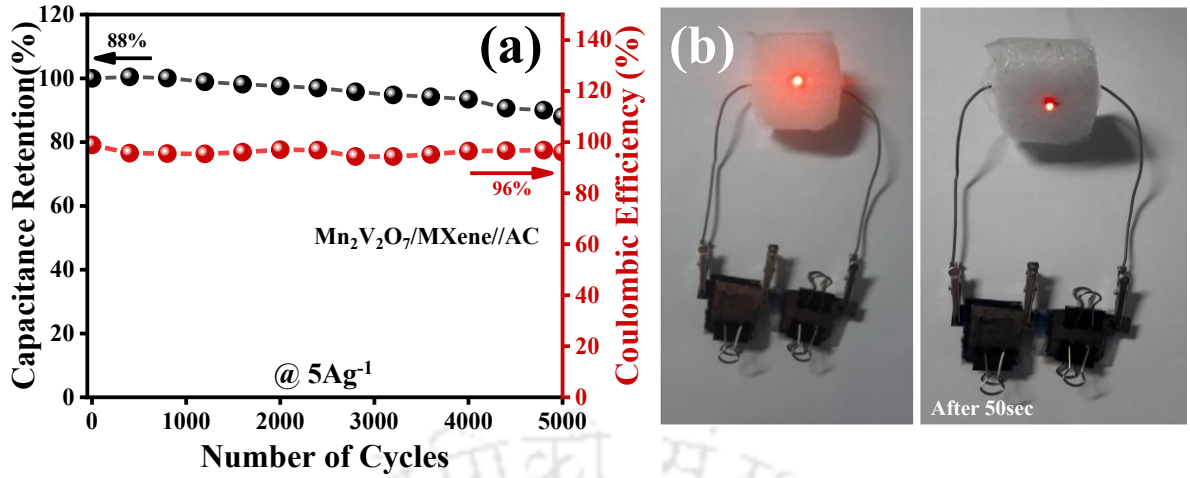

Figure 4.10: (a) Long-term cycling performance and Coulombic efficiency of the two-terminal device at 10 A g^{-1} using 1 M PVA-Na_2SO_4 electrolyte. (b)Practical demonstration of the device $Mn_2V_2O_7$/MXene//AC glowing LED light of 3V

In addition to its remarkable power capability, the MVO/MXene//AC ASC demonstrates excellent cycling stability within the substantial voltage window of 0–2.0 V. In **Figure 4.10a**, the capacitance retention of the device is presented after 5000 cycles of charge-discharge at a current density of 5 A g^{-1}. After 5,000 cycles, approximately 88% of the initial capacitance was retained, and the Coulombic efficiency remained at 96%, demonstrating superior stability. Lastly, as illustrated in **Figure 4.10b**, the practicality of the MVO/MXene//AC device for real-time applications was assessed by connecting two devices in series and charging them to 3 V to illuminate a red light-emitting diode (LED) bulb. As the current is gradually consumed, the brightness of the bulb diminishes. The red bulb illuminated brightly and dimmed after 50 seconds. All the results provide valuable insights into the promising potential of the assembled MVO/MXene//AC future energy storage applications.

4.4. CONCLUSIONS:

This study explores the synthesis of a composite material by incorporating manganese vanadium oxide nanorods into $Ti_3C_2T_x$ MXene via a cost-effective hydrothermal route. The resulting $Mn_2V_2O_7$/MXene composite exhibits enhanced performance in a 1 M Na_2SO_4 electrolyte, demonstrating increased conductivity, electron/ion transport capacity, and structural stability. The $Mn_2V_2O_7$/MXene achieves a high specific capacitance of 627 F g^{-1} at 1A g^{-1}. When assembled into a device ($Mn_2V_2O_7$/MXene//AC), it provides a voltage window of 2 V, delivering a specific energy of 65 Wh kg^{-1} at a power density of 1000 W kg^{-1}. This research contributes to the development of supercapacitors that overcome the gap between

conventional supercapacitors and batteries, offering a balance between high power delivery and increased energy storage capacity. The results indicate that the newly developed hybrid materials could serve as promising alternatives for high-performance energy storage devices in the future.

Authors Contribution:

Alpana Sahu conceptualized the study, conducted all experiments, analyzed the results, and wrote the manuscript. Anjana Singha evaluated the results and provided guidance. Mohammad Qureshi evaluated the results and oversaw the overall coordination of the experiments, funding, and manuscript writing.

4.5. REFERENCES:

1. G. Wang, L. Zhang, J. Zhang, *Chem. Soc. Rev.* **2012**, *41*, 797.
2. M. Naguib, M. Kurtoglu, V. Presser, J. Lu, J. Niu, M. Heon, L. Hultman, Y. Gogotsi, M. W. Barsoum, *Adv. Mater.* **2011**, *23*, 4248.
3. Z. Yu, C. Li, D. Abbitt, J. Thomas, *J. Mater. Chem. A* **2014**, *2*, 10923.
4. M. F. El-Kady, Y. Shao, R. B. Kaner, *Nat. Rev. Mater.* **2016**, *1*, 16033.
5. V. Augustyn, P. Simon, B. Dunn, *Energy Environ. Sci.* **2014**, *7*, 1597.
6. J. Tang, R. R. Salunkhe, J. Liu, N. L. Torad, M. Imura, S. Furukawa, Y. Yamauchi, *J Am. Chem. Soc.* **2015**, *137*, 1572.
7. X. Lang, A. Hirata, T. Fujita, M. Chen, *Nat. Nanotechnol.* **2011**, *6*, 232.
8. T. E. Balaji, H. Tanaya Das, T. Maiyalagan, *ChemElectroChem* **2021**, *8*, 1723.
9. D. Majumdar, M. Mandal, S. K. Bhattacharya, *ChemElectroChem* **2019**, *6*, 1623.
10. D. Xia, S. Xu, W. Wang, D. Wang, M. Wu, F. Gong, *Chem. Commun.* **2020**, *56*, 8043.
11. F. K. Butt, M. Tahir, C. Cao, F. Idrees, R. Ahmed, W. S. Khan, Z. Ali, N. Mahmood, M. Tanveer, A. Mahmood, I. Aslam, *ACS Appl. Mater. Interfaces* **2014**, *6*, 13635.
12. H. Huang, L. Wei, T. Tian, T. Cao, F. Cheng, Z. Chen, Z. Yang, B. Ge, M. Tian, W. Zhang, M. Niederberger, *Energy Storage Mater.* **2022**, *47*, 579.
13. D. Merum, R. R. Nallapureddy, M. R. Pallavolu, T. K. Mandal, R. R. Gutturu, N. Parvin, A. N. Banerjee, S. W. Joo, *ACS Appl. Energy Mater.* **2022**, *5*, 5561.
14. Z. Chen, Y. Peng, F. Liu, Z. Le, J. Zhu, G. Shen, D. Zhang, M. Wen, S. Xiao, C.-P. Liu, Y. Lu, H. Li, *Nano Lett.* **2015**, *15*, 6802.
15. J. Zhou, B. Liu, L. Zhang, Q. Li, C. Xu, H. Liu, *J Mater. Chem. A* **2022**, *10*, 24896.
16. M. Tomy, A. Ambika Rajappan, V. VM, X. Thankappan Suryabai, *Energy & Fuels* **2021**, *35*, 19881.
17. K. R. G. Lim, M. Shekhirev, B. C. Wyatt, B. Anasori, Y. Gogotsi, Z. W. Seh, *Nature Synthesis* **2022**, *1*, 601.
18. S. P. Ghaemi, S. M. Masoudpanah, S. Alamolhoda, *J. Energy Storage* **2023**, *67*, 107635.
19. S. Ohkoshi, Y. Tsunobuchi, T. Matsuda, K. Hashimoto, A. Namai, F. Hakoe, H. Tokoro, *Nat. Chem.* **2010**, *2*, 539.

20. A. Sarkar, A. K. Singh, D. Sarkar, G. G. Khan, K. Mandal, *ACS Sustain. Chem. Eng.* **2015**, *3*, 2254.
21. M. R. Lukatskaya, O. Mashtalir, C. E. Ren, Y. Dall'Agnese, P. Rozier, P. L. Taberna, M. Naguib, P. Simon, M. W. Barsoum, Y. Gogotsi, *Science* **2013**, *341*, 1502.
22. H. Zhang, B. Farhadi, K. Wang, X. Xing, Y. Zhu, X. Guo, K. Wang, S. Liu, *Chem. Eng. J.* **2024**, *479*, 147293.
23. Y. Lu, C.-Z. Zhao, J.-Q. Huang, Q. Zhang, *Joule* **2022**, *6*, 1172.
24. A. K. Tomar, T. Kshetri, N. H. Kim, J. H. Lee, *Energy Storage Mater.* **2022**, *50*, 86.
25. M. Naguib, R. A. Adams, Y. Zhao, D. Zemlyanov, A. Varma, J. Nanda, V. G. Pol, *Chem. Commun.* **2017**, *53*, 6883.
26. D. Sarkar, D. Das, S. Das, A. Kumar, S. Patil, K. K. Nanda, D. D. Sarma, A. Shukla, *ACS Energy Lett* **2019**, *4*, 1602.
27. Y. Tian, C. Yang, Y. Tang, Y. Luo, X. Lou, W. Que, *Chem. Eng. J.* **2020**, *393*, 124790.
28. O. Capron, R. Gopalakrishnan, J. Jaguemont, P. Van Den Bossche, N. Omar, J. Van Mierlo, *Materials* **2018**, *11*, 176.
29. N. Jabeen, A. Hussain, Q. Xia, S. Sun, J. Zhu, H. Xia, *Adv. Mater.* **2017**, *29*, 1700804.
30. M. Samir, N. Ahmed, M. Ramadan, N. K. Allam, *ACS Sustain. Chem. Eng.* **2019**, *7*, 13471.
31. B. Ranjan, D. Kaur, *Small* **2023**, 20, 2307723.
32. V. Sethuraman, R. D. Kumar, A. Prabhakaran, P. Rajkumar, K. Diwakar, M. Senthilkumaran, M. Saravanan, R. Sasikumar, K. Aravinth, P. Ramasamy, R. Manigandan, *J Energy Storage* **2022**, *55*, 105553.
33. M. Mahmood, A. Rasheed, I. Ayman, T. Rasheed, S. Munir, S. Ajmal, P. O. Agboola, M. F. Warsi, M. Shahid, *Energy & Fuels* **2021**, *35*, 3469.
34. L. Li, S. Peng, H. Bin Wu, L. Yu, S. Madhavi, X. W. (David) Lou, *Adv Energy Mater* **2015**, *5*, 1500753.
35. W. Luo, Y. Sun, Z. Lin, X. Li, Y. Han, J. Ding, T. Li, C. Hou, Y. Ma, *J Energy Storage* **2023**, *62*, 106807.
36. Q. Zhou, Y. Gong, J. Lin, *Appl Surf Sci* **2018**, *439*, 33.
37. H. Wang, Y. Zhang, E. Guo, C. Hu, Q. Lu, M. Wei, J. Ma, C. Si, *New Journal of Chemistry* **2022**, *46*, 4385.
38. Y. Li, P. Kamdem, X.-J. Jin, *Dalton Transactions* **2020**, *49*, 7807.
39. M. Samir, N. Ahmed, M. Ramadan, N. K. Allam, *ACS Sustain Chem Eng* **2019**, *7*, 13471.
40. S. B. Ambade, R. B. Ambade, W. Eom, S. H. Noh, S. H. Kim, T. H. Han, *Adv Mater Interfaces* **2018**, *5,* 1801361.
41. A. Sharma, P. Mane, B. Chakraborty, C. S. Rout, *ACS Appl Energy Mater* **2021**, *4*, 14198.

CHAPTER 5

Boron and Oxygen-Coordinated Heterostructures: Interface-Driven Electronic Reconfiguration for high-performance supercapacitors

In this chapter, we have utilized the electron deficiency of boron, arising from its vacant p-orbital, which readily interacts with the lone pair electrons of oxygen, enhancing electron delocalization and electrical conductivity. Such interactions are leveraged to improve the performance of supercapacitor electrodes. This chapter has two parts: Chapter 5 and Chapter 6, and both chapters we have utilize different Boron and oxygen-containing 2D materials for supercapacitor applications.

CHAPTER 5a

Metal-free Borophene/rGO composite with Dirac semi-metallicity for high-performance supercapacitors

Borophene, a unique semi-metallic Dirac material with exceptional mechanical and electronic properties, has gathered increasing attention in electronics. Both theoretical and experimental studies confirm its excellent performance in energy storage applications. However, borophene requires conductive substrates for stability, which limits its potential for energy storage applications. To address this, a strategy for fabricating flexible and conductive rGO-supported borophene supercapacitor electrodes is proposed, featuring a layered assembly of borophene nanosheets sandwiched between rGO layers. This architecture effectively prevents the self-restacking of rGO nanosheets, leading to a significant increase in the interlayer spacing of 5.75 Å between rGO and borophene, which promotes the rapid diffusion of electrolyte ions and makes more electroactive sites accessible for electrochemical storage.

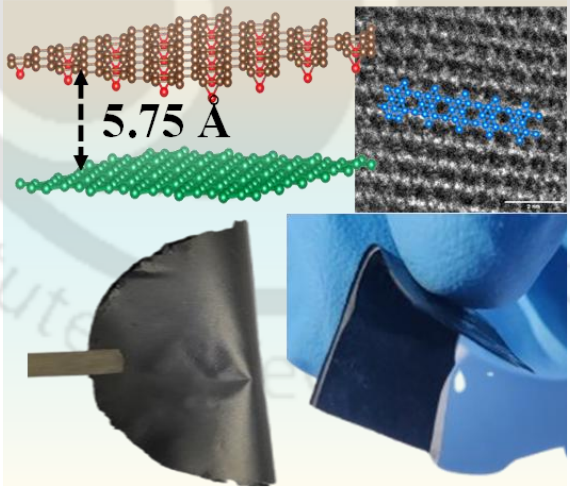

Part of this manuscript has been published in ***Nano Lett.*, 2025, 25, 5019**

5a.1. INTRODUCTION:

The emergence of supercapacitors is renowned for their exceptional performance characteristics, including rapid charge/discharge cycles, high power densities, and extended cycling life, which position them as leading candidates for energy storage applications.[1,2] The electrode plays a prominent role in storing charges in supercapacitors and it includes advanced materials in the range of 0D, 1D, 2D, and 3D.[3,4]Among these materials, 2D materials have gained interest in the supercapacitor field due to their larger surface area, mechanical flexibility, and exciting electronic properties[5,6]. 2D materials such as graphene,[7] arsenene,[8] tellurene,[9] phosphorene[10], bismuthene[11], and borophene[12] have been utilized for their unique properties, including minimal thickness and a surface-dominated structure, which maximize the surface-to-bulk ratio and accessible active sites for enhanced ion adsorption/desorption and electrochemical performance. Borophene, a single-atom-thick boron layer, stands out for its exceptional mechanical strength, flexible structure, and tunable optical and electrical properties, making it a leading choice for electrode applications. [13–15] It demonstrates remarkable electronic mobility (280,000 $cm^2V^{-1}s^{-1}$), superconductivity, high thermal conductivity (233.3 $Wm^{-1}K^{-1}$), impressive elasticity with Young's modulus of 398 N m^{-1}, anisotropic mechanics, and unique structural characteristics.[16,17] Boron can form three-centre-two-electron bonds, enabling it to generate a wide variety of atomic clusters. In the β_{12} phase of borophene, the atomic arrangement forms ridgelines, essentially chains of atoms with strong bonding leading to an extensive overlap of atomic orbitals, particularly p_z orbitals to, enhance electron delocalization for increased electron density. [18,19] A high electron density near the Fermi level promotes metallic conductivity, ensuring efficient charge transport, a critical feature for energy storage applications. Along with this, it shows a high theoretical capacitance of 400 Fg^{-1} which is four times that of graphene 2D nanosheets stands out as an exceptional candidate for supercapacitor electrodes, benefiting from their metallic properties.[20] All these remarkable characteristics position borophene as a promising material, inspiring analyses of its structure and potential applications in various fields, including energy storage.

Borophene faces structural instability due to the absence of one electron required to form sp^2 hybridization, which poses experimental challenges for creating freestanding Borophene electrodes.[21] Tai et al. successfully synthesized atomically thin 2D boron films on copper foils using chemical vapor deposition at low pressures.[22] Abdi et al. successfully synthesized borophene using a chemical vapor deposition (CVD) method, resulting in a supercapacitor with

a remarkable capacitance of 350 Fg^{-1}.[23] However, the reported literature suffers from scalability issues owing to the use of tedious fabrication protocols for their widespread application in energy storage and other domains. Despite these obstacles, Li et al. made a significant breakthrough by utilizing a sonication-assisted liquid phase exfoliation technique on bulk boron [24]. This method produced few-layer boron sheets suitable for large-scale production while exhibiting excellent stability and making them promising for high-performance supercapacitor electrodes with impressive electrochemical performance.

The production and scalability of freestanding borophene are hindered by its intrinsic reactivity to oxidation and degradation, compromising quality and stability at larger sizes. In this study, we address these limitations by hybridizing borophene with highly capacitive reduced Graphene oxide (rGO) to fabricate a flexible, freestanding electrode. The interlayer gap of 5.75 Å between rGO and borophene promotes enhanced electrolyte ion diffusion, improving access to electroactive sites, reflected in the excellent electrochemical performance. The rGO/Borophene **(rGO/Bp)** flexible electrode delivers a specific capacitance of 328 Fg^{-1} at 1 Ag^{-1}, with 98% capacitance retention after 10,000 cycles. Electrochemical impedance spectroscopy (EIS) data were also analyzed using Distribution of Relaxation Time (DRT) measurements to confirm the superior charge transfer kinetics of the rGO/Bp composite. The assembled symmetric supercapacitor achieves an impressive energy density of 23 $Whkg^{-1}$ and maintains stable energy output even under various bending angles. This novel approach leverages unique properties of borophene, including its superior electronic density of states (DOS) and semi-metallic characteristics, to enhance the overall capacitance and energy output of the electrode.

5a.2. EXPERIMENTAL:

5a.2.1. Synthesis of Borophene:

80 mg of boron powder was taken and dispersed in 80 mL of N, N-DMF and put for a solvothermal reaction in a 100mL reactor for 12h at 200 °C. The dispersion underwent probe sonication in an ice bath, employing an ultrasonic frequency of 20 kHz and an output power of 60 W for 4h. The resultant solution was centrifuged at 2500 rpm for 30 min and the supernatant was collected and dried to get exfoliated boron sheets.

5a.2.2. Synthesis of rGO:

Graphene Oxide (GO) was synthesized using the modified Hummer's method.[25] In a typical synthesis, graphite powder (1 g) and sodium nitrate (0.748 g) were added to concentrated

H_2SO_4 (74.8 mL) and kept stirring over 1 h in an ice bath followed by slow addition of $KMnO_4$ (4.5 g). The mixture was kept stirring for another 2 h. The mixture was kept under stirring for 7 days at 35 °C. After that, H_2SO_4 (140 mL 5 wt%) was added to it and the temperature was raised to 98 °C with another 2 h of stirring. The temperature was then brought down to room temperature, followed by the addition of H_2O_2 (1.88 mL 48 wt% aqueous solution) and stirred for 2 h. The precipitate obtained was dissolved in aqueous solution of 3 wt% H_2SO_4/0.5 wt% H_2O_2 (400 mL) and sonicated for 1 h. The solution mixture was then centrifuged and sonicated to remove impurities, and a similar technique was followed with 3 wt% HCl solution.[26] Then, it was dispersed in DMF (0.5mg/mL) to reduce GO and refluxed for 2 hours at 150 °C.

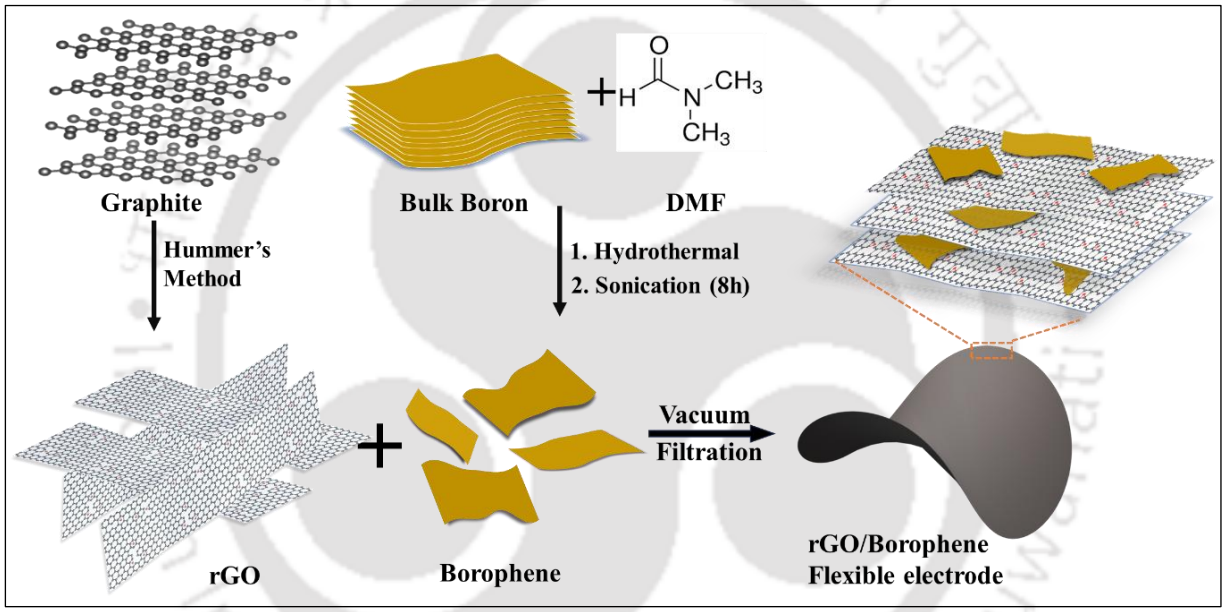

Scheme 5a.1: Illustrating rGO was prepared by the Hummers method, oxidising graphite to Graphene oxide and then chemically reducing graphene oxide in DMF to get rGO; Borophene nanosheets (NSs) were synthesized via a solvothermal-assisted sonication, and the rGO/Borophene composite was synthesized via a vacuum filtration to get a free-standing electrode.

5a.2.3. Fabrication of Working Electrode:

Different ratios of as-synthesized Borophene to rGO are dispersed in DMF and it was ultrasonicated at 90 W with a frequency of 40kHz for 1 h. Then it was vacuum filtered through a polytetrafluoroethylene (PTFE) membrane (pore size: 5µm) followed by drying in an oven at 70 °C for 2 h. The oven-dried freestanding r-GO/Borophene (rGOB) membrane was peeled

off from the PTFE membrane. Different ratios of r-GO/Borophene electrodes were denoted as rGOB11, rGOB12, and rGOB13. In the main manuscript, we have detailed the optimal performing ratio, designated as rGOB11, which is referred to here as the rGO/Borophene(**rGO/Bp)** composite.

5a.2.4. Computational details:

In this work, all the calculations are performed by the projector augmented wave potential method based on DFT as implemented in the VASP code.[27–29] The Perdew–Burke–Ernzerhof (PBE) exchange-correlation function was employed at the level of Generalized Gradient Approximation (GGA).[30] The kinetic energy cut-off of 500 eV for the plane-wave expansion is found to be sufficient. The Monkhrost-Pack method is used to sample the *k* points in the Brillouin zone. The initial structure with supercell 3x3 for borophene and 5x2 for Graphene oxide is employed to obtain the most stable heterostructure and all the surface slabs were modeled with a 20.00 Å vacuum layer along the Z-axis. The Brillouin zone of the supercell is sampled with the M-packed grid of 3x3x1 which is used for optimization. The electronic density was converged with a 10^{-5} eV total energy threshold, and the structures were optimized until the maximum force on any ion was less than 0.001 eV/Å. After geometry optimization, a M-packed grid of 7x7x1 and LORBIT=11 tag was used to generate the density of state analysis. For the density of states visualizations, vaspkit was used to analysis the results.[31]

5a.2. RESULTS AND DISCUSSION:

5a.2.1. Characterisation of Borophene:

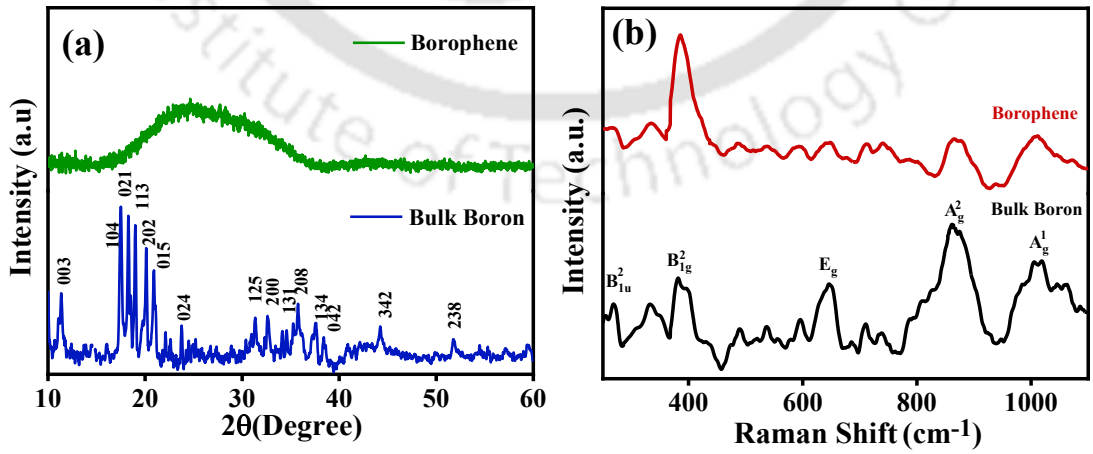

Figure 5a.1:(a) PXRD pattern (b) Raman spectra of bulk Boron and exfoliated Borophene

Borophene nanosheets (NSs) were synthesized via a solvothermal-assisted sonication technique, as illustrated in **Scheme 5a.1**. **Figure 5a.1a** shows the XRD pattern of bulk boron powder with a β-rhombohedral phase as per the standard literature (JCPDS card no. 00-031-0207). However, after sonication, the crystalline XRD patterns observed in the bulk boron transition to an amorphous hump in borophene sheets as the sonication process disrupts the long-range crystalline order of the lattice, breaking down the material into thinner borophene layers.[32] Additionally, we have done the Raman measurements to confirm the phase formation. Notably, the Raman spectra of both bulk boron and borophene exhibit six predominant peaks at 271, 388, 646, 846, and 1020 $cm^{-1,}$ which align well with the reported vibrational modes of the β12 borophene phase, as shown in **Figure 5a.1b.** Accordingly, the strong peak at 271 cm^{-1} is ascribed to the out-of-plane bending vibration mode B_{1u}^2 of the β12 phase, and the other peaks at 388, 646, 846.8, and 1020 cm^{-1} are respectively indexed as the B_{1g}^2, E_g, A_g^2, and A_g^1, modes, resulting from the in-plane stretching modes of the β12 phase. Notably, the characteristic A_g^2 (846.8 cm^{-1}) and A_g^1 (1020 cm^{-1}) Raman modes are associated with B–B bond vibrations and exhibit a relatively reduced intensity in borophene compared to bulk boron. This reduction provides strong evidence for the successful formation of the borophene phase, indicating structural modifications inherent to its 2D nature.[33,34]

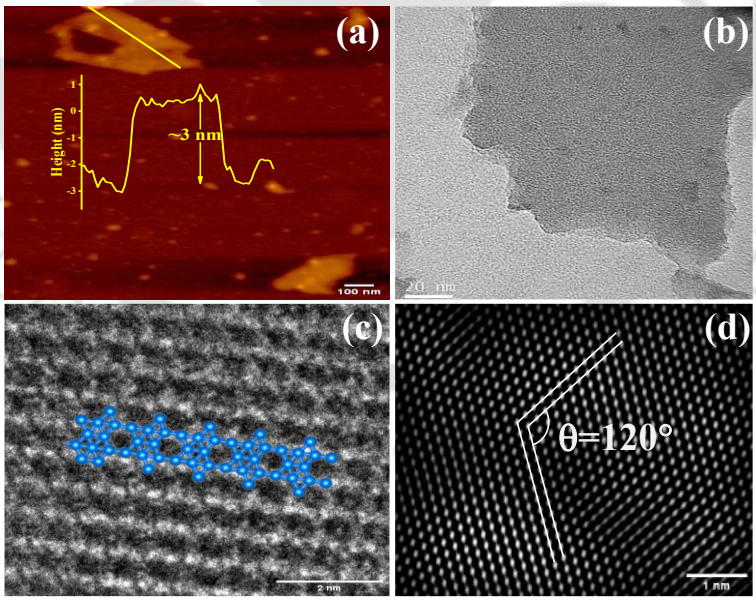

Figure 5a.2:(a) AFM image of few layers of borophene with a nanoscale thickness (b) FETEM image of borophene (c) Honeycomb lattice of borophene (d) corresponding fast Fourier transform pattern of image (c), EDS elemental mapping of (g) borophene showing the presence of (h) Boron (i) Oxygen (j) Nitrogen

The broadening and slight shifts of these peaks, compared to bulk boron, further suggest the transition to a 2D structure with nanoscale thickness. The result of atomic force microscopy (AFM) analysis demonstrates few-layer thickness of borophene amounting to the roughness of ~ 3 nm, confirming its ultrathin 2D nanostructure **Figure 5a.2a**. Further structural insights were obtained through FETEM, which revealed a few-layer borophene nanosheets formed due to sonication-induced exfoliation of bulk borophene due to the disruption of van der Waals forces **Figure 5a.2b.** High-resolution TEM imaging revealed lattice fringes with a d-spacing of 0.51nm, suggesting the existence of localized crystalline regions within the thin-layered borophene structure (inset **Figure 5a.2b**).[35] Furthermore, as shown in **Figure 5a.2c,** the 2D borophene sheet exhibits a hexagonal honeycomb lattice with a well-defined planar periodicity and a unit cell intersection angle (θ) of ~120° (**Figure 5a.2d)**, indicating a structured arrangement within the borophene material.[36]

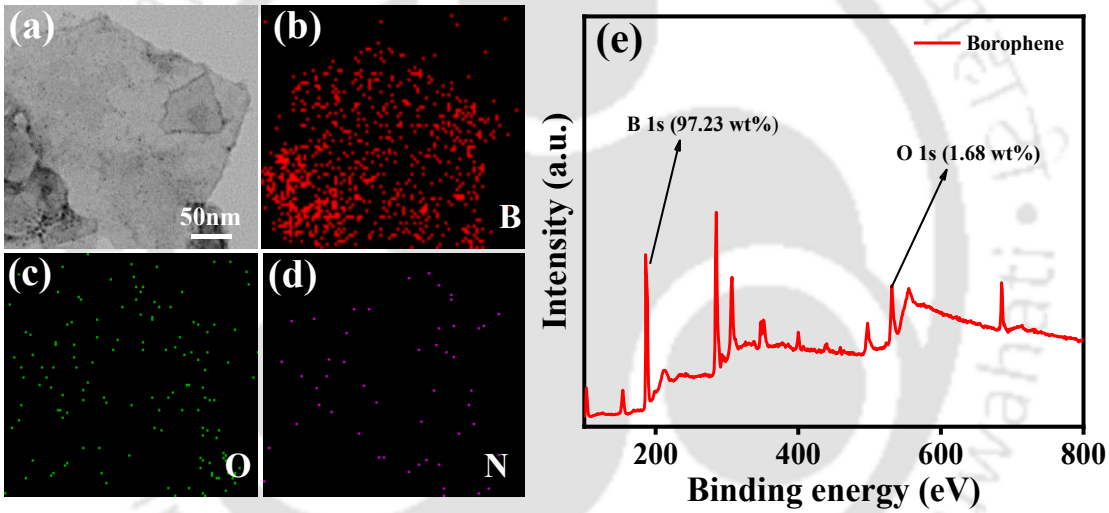

Figure 5a.3: EDS elemental mapping of (a) borophene showing the presence of (b) Boron (c)Oxygen(d) Nitrogen (e) XPS survey spectra of borophene.

Figure 5a.3(a-d) shows the EDX elemental mapping of DMF-exfoliated B sheets of **Figure 5a.1g,** indicating a homogeneous distribution of B with a few amount of N and O. The detected oxygen and nitrogen likely originate from surface oxidation and residual solvent interactions rather than representing bulk impurities. The analysis of the XPS survey spectra**5a.3(e)**, calculated using the atomic sensitivity factor of each element, confirms a boron concentration of 98.2%, with only minor amounts of oxygen (1.68%) and nitrogen (1.09%). This composition indicates that the material is predominantly borophene.

5a.2.2. Characterisation of rGO/Borophene composite:

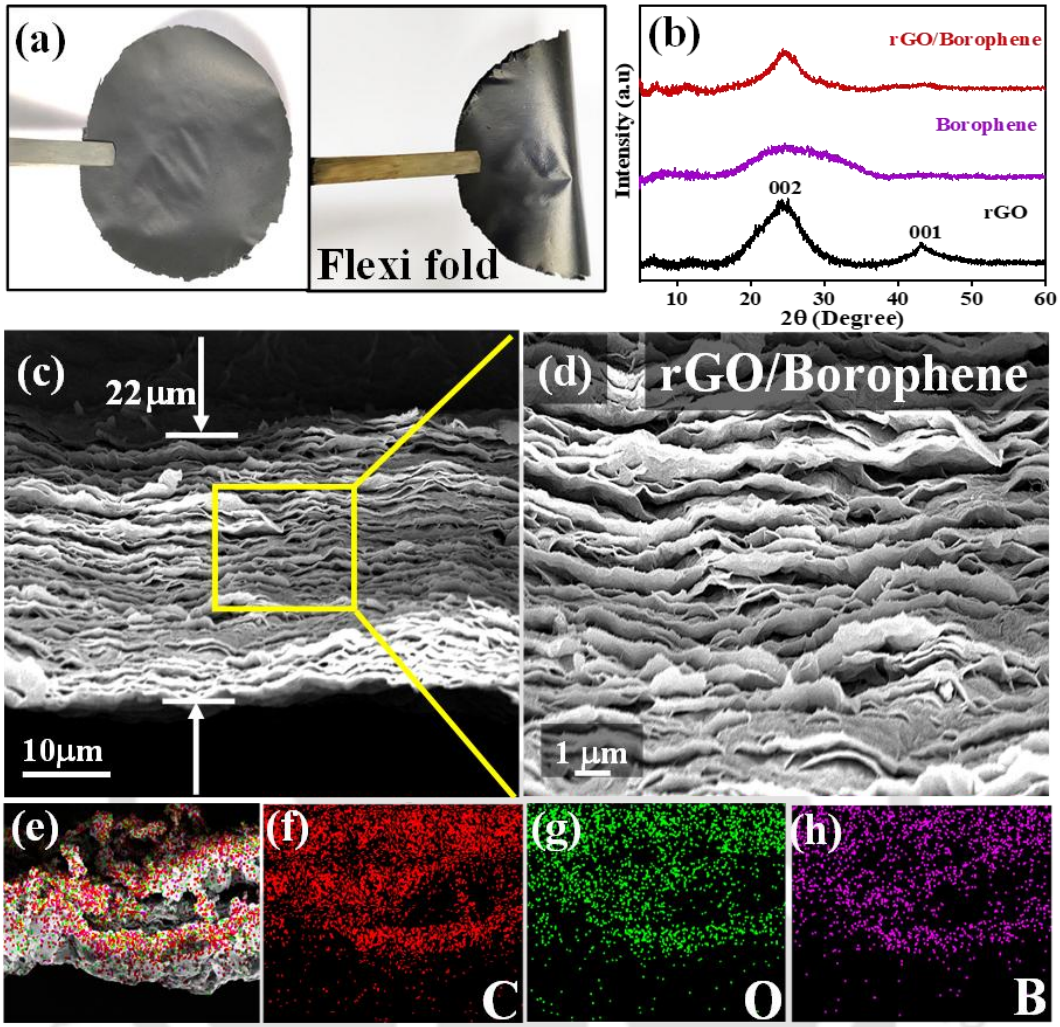

Figure 5a.4:(a) Photographic images of the hybrid film under flexible geometrical configuration (b) XRD pattern of rGO, Borophene, and rGO/Borophene, Cross-Sectional FESEM image of rGO/Borophene 2D hybrid electrode (c) at low resolution (d) at high resolution, FESEM-EDX mapping of image (e) showing the presence of individual elements, i.e.(f) Carbon, (g) Oxygen, (h) Boron.

The rGO/Bp composite was synthesized using a solution-based assembly approach as illustrated in **Scheme 5a.1**. rGO was prepared by chemically reducing graphene oxide in DMF, while borophene nanosheets (NSs) were obtained through solvothermal-assisted sonication. The borophene NSs were dispersed into the rGO suspension under continuous sonication, followed by vacuum filtration, aligning the sheets into a tightly packed rGO/Bp layered structure. This process enabled synergistic interactions by bringing the rGO and borophene sheets into close proximity, as shown in **Figure 5a.4a**, highlighting the structural flexibility of

the freestanding electrode without any signs of damage. The crystal structures of rGO, borophene, and the composite were analyzed via XRD where rGO showed a characteristic diffraction peak at 2θ = 24.5° (002), while borophene NSs displayed a broad amorphous hump. The XRD pattern of the rGO/borophene composite displayed diffraction features corresponding to both rGO and borophene, confirming the successful integration of both materials **Figure 5a.4b**. The cross-sectional views of the hybrid film reveal that integrating borophene into the rGO matrix does not disrupt the intrinsic architecture of the rGO assembly. **Figure 5a.4c**. Instead, the borophene and rGO nanosheets are found to be forming a continuous and well-ordered layered structure throughout the hybrid film as can be observed in **Figure 5a.4d**. The orderly stacking of the material suggests a synergistic interaction between the two materials, contributing to the overall structural integrity and performance of the hybrid electrode. This interaction promotes adhesion and stabilization, enhancing structural integrity, preventing restacking, and optimizing charge transport, which in turn improves the electrochemical performance of the hybrid electrode. Meanwhile, the elemental characterization of rGO/Bp, performed by Energy-dispersive X-ray (EDX) spectroscopy mapping, shows that the B, C, and O elements are uniformly distributed, demonstrating that Borophene nanosheets homogeneously anchor onto the rGO surface **Figure 5a.4(e-h)**.

5a.2.3. Surface Area Analysis:

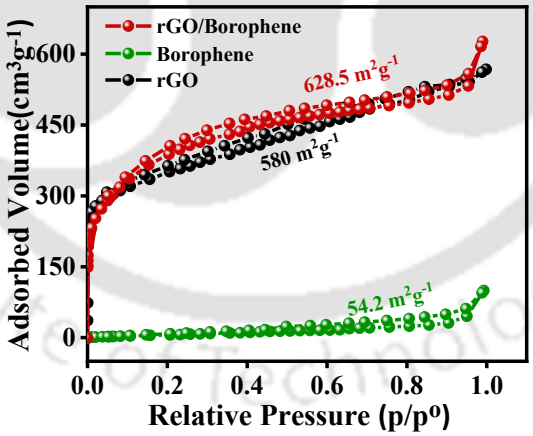

Figure 5a.5: BET nitrogen adsorption isotherm plot of bare Borophene, rGO and rGO/Borophene

The BET measurements are conducted to evaluate the specific surface area of the synthesized materials. The rGO/Bp hybrid (**Figure 5a.5**) exhibits a specific surface area of approximately 628.5m^2g^{-1} which is higher than borophene (54.2m^2g^{-1}) and rGO(580m^2g^{-1}). This significant increase in surface area highlights the enhanced exposed surface area of the composites.

5a.2.4. Electronic State Analysis:

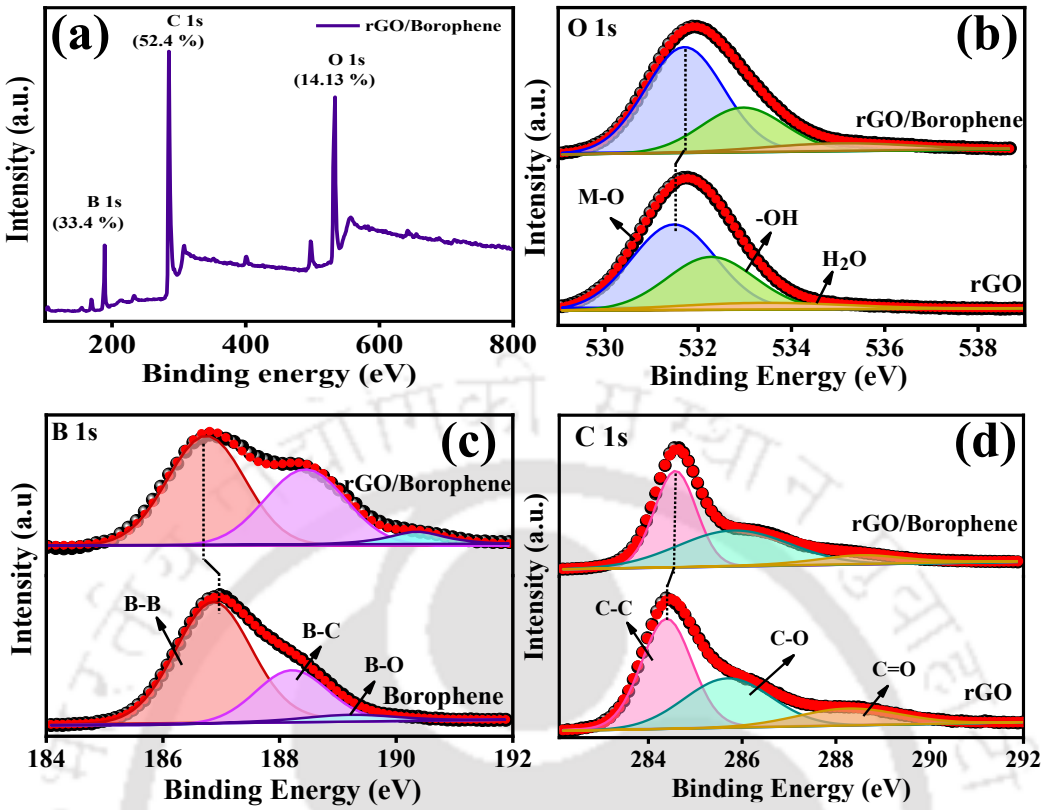

Figure 5a.6: (a) XPS survey spectra of rGO/Bp composite electrode indicating the %age of each element, High resolution XPS spectra of (b) O 1s (c) B 1s (d) C 1s showing synergistic interaction between rGO and Borophene.

X-ray photoelectron spectroscopy (XPS) was used to analyse the chemical state and electronic interactions among the materials. **Figure 5a.6a** displays the survey spectra of rGO/Bp, revealing the presence of B, C, and O elements, with concentrations of 33.4%, 14.13%, and 52.4%, respectively. **Figure 5a.6b** presents the O 1s spectrum, deconvoluted into three peaks: 531.7 eV, associated with lattice oxygen in the composite and corresponding to M–O bonding; 532.9 eV, related to OH^- ions; and 535.03 eV, corresponding to adsorbed water molecules on the surface. The O 1s core-level spectra of rGO/Bp show a shift towards the higher binding energy by ~0.3 eV compared to pure rGO, indicating a strong electronic interaction between the rGO and borophene hybrid. **Figure 5a.6c** illustrates the XPS B 1s spectrum for bare borophene and the rGO/borophene composite. The high-resolution B 1s spectrum shows three distinct peaks attributed to B–B, B–C, and B–O bonds.[37] The deconvoluted peaks shift to lower binding energies by ~0.5eV in the rGO/Bp composite compared to borophene alone, indicating stronger integration of boron atoms with the rGO

matrix, resulting in more robust B–C, and B–O interactions. The core-level XPS spectrum of C 1s for the rGO/Bp nanocomposite is shown in **Figure 5a.6d.** The deconvoluted peak at 284.5 eV corresponds to the C–C bond of rGO, while residual oxygen is evidenced by peaks at 285.5 eV and 288.5 eV, attributed to C–O and C=O bonds, respectively. In the composite, the C 1s peak shifts to a higher binding energy compared to bare rGO, suggesting an increased electron density over the carbon atoms. The shifts in the B 1s and O 1s spectra suggest electronic changes that increase electron density around the carbon atoms, as reflected by changes in the C 1s binding energy. This redistribution of electrons, as evidenced by the shift in binding energy, creates partial charge polarization, enhancing interfacial interactions between rGO and borophene.

5a.2.5. Electrochemical Analyses:

The electrochemical characterization has been evaluated in a three-electrode setup in 1M KOH basic medium using Hg/HgO as the reference electrode and Platinum as the counter electrode. Different ratios of Borophene and rGO (1:1, 1:2,1:3) have been taken to investigate the potential electrochemical performance. At a scan rate of 10mV s^{-1}, the CV curve (**Figure 5a.7**) of the rGOB11 hybrid film had a large integrated area as compared to its other composite ratios rGOB12 and rGOB13, including a longer charge-discharge time. Increasing borophene concentration beyond the optimal level may disrupt the layered architecture, hinder ion transport and reducing supercapacitor performance. In this chapter, we have detailed the optimal performing ratio, designated as rGOB11, which is referred to here as the rGO/Borophene**(rGO/Bp)** composite.

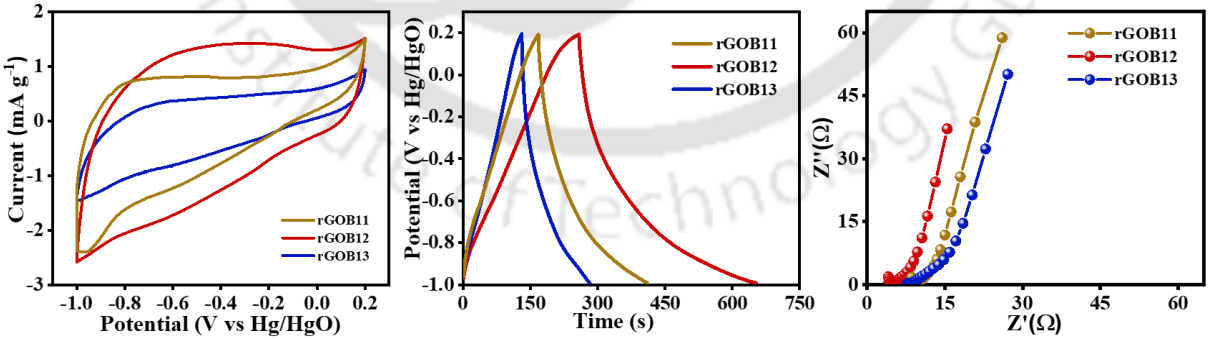

Figure 5a.7: Comparison of (a) CV curves at 10 mVs^{-1} (b) GCD at 1 Ag^{-1} and (c) Nyquist plot composite rGO/Bp taking rGO and Borophene in different ratios.

As shown in **Figure 5a.8a** the CV curves of both electrodes at a scan rate of 10 mVs^{-1} reveal that the rGO/Bp hybrid film exhibits a significantly larger integrated area than bare rGO,

indicating an enhanced electrochemical performance. Similarly, GCD measurements (**Figure 5a.8b**) further confirm that the rGO/Bp electrode displaying a prolonged discharge time at 1 Ag^{-1}, corresponding to a high specific capacitance of 328 $Fg^{-1,}$ which is four times higher that of rGO (82 F g^{-1}). CV analysis of the rGO/Bp electrode (**Figure 5a.8c**) at 10–100 mVs^{-1} shows a quasi-rectangular profile, indicating a charge storage mechanism combining electrical double-layer capacitance and reversible faradaic reactions. This is attributed to the high surface area of rGO/Bp, enabling ion adsorption and desorption, while oxygen functional groups enhance pseudocapacitance.[38] In **Figure 5a.8d** GCD curves exhibit symmetric profiles across 1–10 A $g^{-1,}$ reflecting high reversibility and low resistive losses. The specific capacitance drops from 328 Fg^{-1} at 1 Ag^{-1} to 168 Fg^{-1} at 10 $Ag^{-1,}$ maintaining 50.7% of its original value, showing good rate capability and effective charge transport in the hybrid electrode.

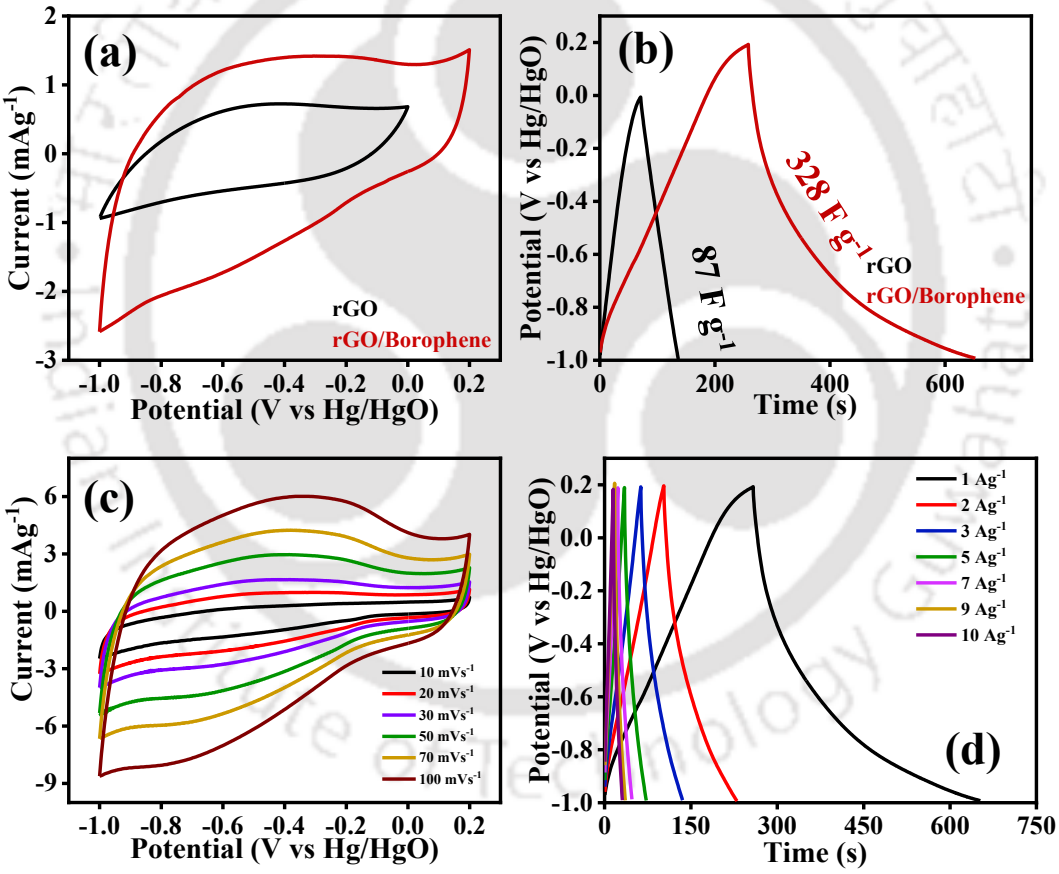

Figure 5a.8: Comparison of (a) CV curves at 10 mVs^{-1} (b) GCD at 1 Ag^{-1} of pristine rGO and the rGO/Bp (c) CV curves of the rGO/Bp electrode from 10 to 100 mVs^{-1} (d) GCD curves of the rGO/Bp electrode from 1 to 10 Ag^{-1}.

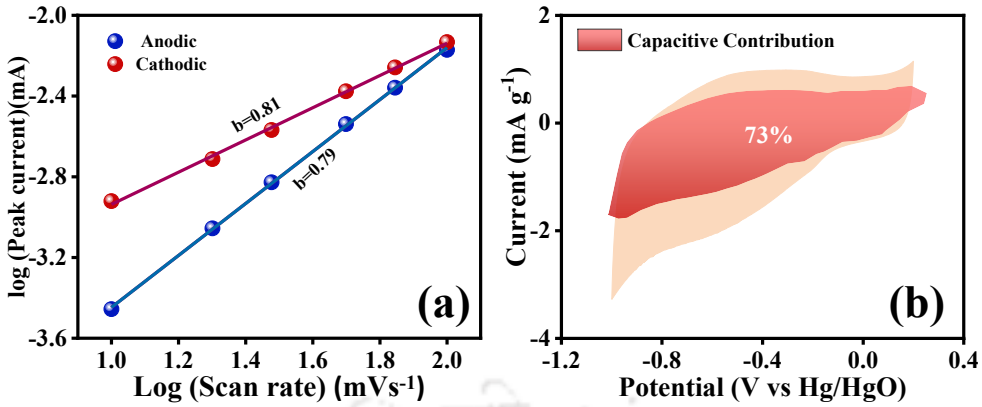

Figure 5a.9: (a) the relationship between peak current density and sweep rate for rGO/Bp (b) capacitive controlled contribution at a sweep rate of 10 mVs^{-1} of rGO/Bp

The charge storage mechanism of the rGO/Bp electrode was examined by assessing the contributions of capacitive and diffusion-controlled processes. The parameter b, calculated from CV plots using the equation $i = av^b$, showed values of 0.81 for the anodic process and 0.79 for the cathodic process, indicating a dominant capacitive contribution with a minor diffusion-limited faradaic component **(Figure 5a.9a)**. The quantitative current contribution from surface-capacitive and diffusive-faradaic mechanisms can be deconvoluted from the total current using Dunn's method. Notably, the capacitive kinetics contribute a significant 73% of the total voltammetric current at 10 mVs^{-1} as shown in **Figure 5a.9b**. This surface-dominated capacitive charge storage property further explains the high-rate performance of the rGO/Bp electrode.

5a.2.6. Electrochemical Impedance Spectroscopy Analyses followed by Distribution of relaxation time:

EIS was performed to analyse charge-discharge dynamics, as shown in the Nyquist plot as shown in **Figure 5a.7a**. In the low-frequency region, both rGO/Bp and rGO exhibit a near-vertical line, indicating capacitive behavior, with the rGO/Bp electrode displaying a steeper slope, signifying enhanced capacitance. In the high-frequency region, the rGO/Bp composite shows a lower charge transfer resistance (R*ct*) than rGO, suggesting improved charge transfer efficiency. To further elucidate the electrochemical processes, DRT analysis was employed, identifying time constants and refining kinetic interpretations. The observed relaxation time and its charge transfer processes in the system correlated to different electrochemical phenomena such as interfacial contact, charge transfer resistance, and diffusion characteristics

within the electrolyte/electrode interface.[39] Deconvoluting the EIS spectra using DRT revealed multiple peaks in the γ(Ω) versus τ(s) plot, corresponding to distinct kinetic processes involved in the charge-discharge mechanism, and the area under the peak represents the total polarization resistance of a specific process.

Figure 5a.7b illustrates the DRT profile featuring four peaks, where:

τ_1: interfacial contact/conductivity of rGO/Borophene

τ_2, τ_3: charge transfer process associated with the electrolyte

τ_4: diffusion processes of the electrolyte

Table 5a.1: Represents the calculated resistance of each electrode:

Materials	τ_1 Resistance (Ω)	τ_2 Resistance (Ω)	τ_3 Resistance (Ω)	τ_4 Resistance (Ω)
rGO	2.73×10^{-7}	3.80×10^{-4}	0.01374	13.48
rGOB/Bp	1.54×10^{-7}	8.8×10^{-6}	3.52×10^{-4}	3.74

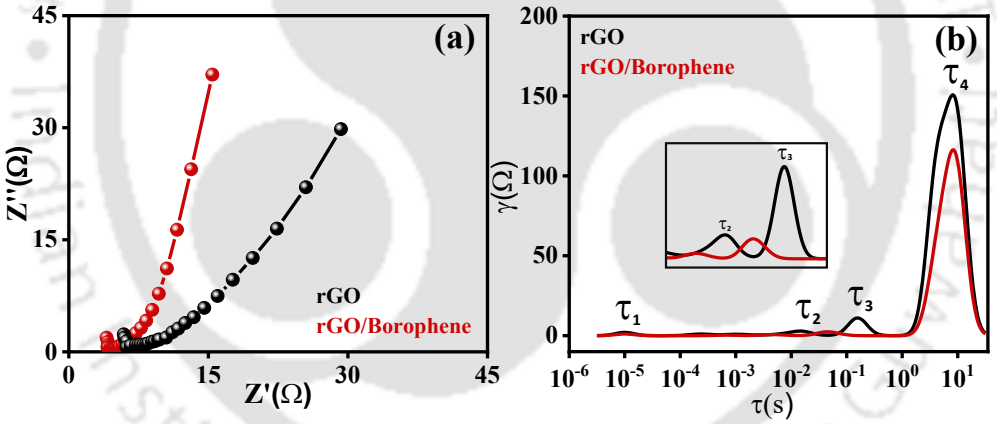

Figure 5a.10: (a) Nyquist plot of all the electrodes obtained from EIS (b) Distribution of relaxation time curve of rGO/Bp hybrids and rGO (inset showing enlarged image of τ_2, τ_3 peak)

Table 5a.1 presents the resistance values associated with different electrochemical processes. Notably, the rGO/Bp composite exhibits significantly lower resistance across these processes compared to bare rGO, indicating improved electrical and ionic transport properties. This enhancement is particularly evident in the faster relaxation times observed for charge transfer processes (τ_2, τ_3), suggesting more efficient interfacial charge transfer and reduced ion diffusion resistance **(Figure 5a.10b)**. These findings demonstrate that the rGO/Bp composite

facilitates enhanced ion transport dynamics, ultimately leading to superior electrochemical performance.

5a.2.7. Symmetric Supercapacitor:

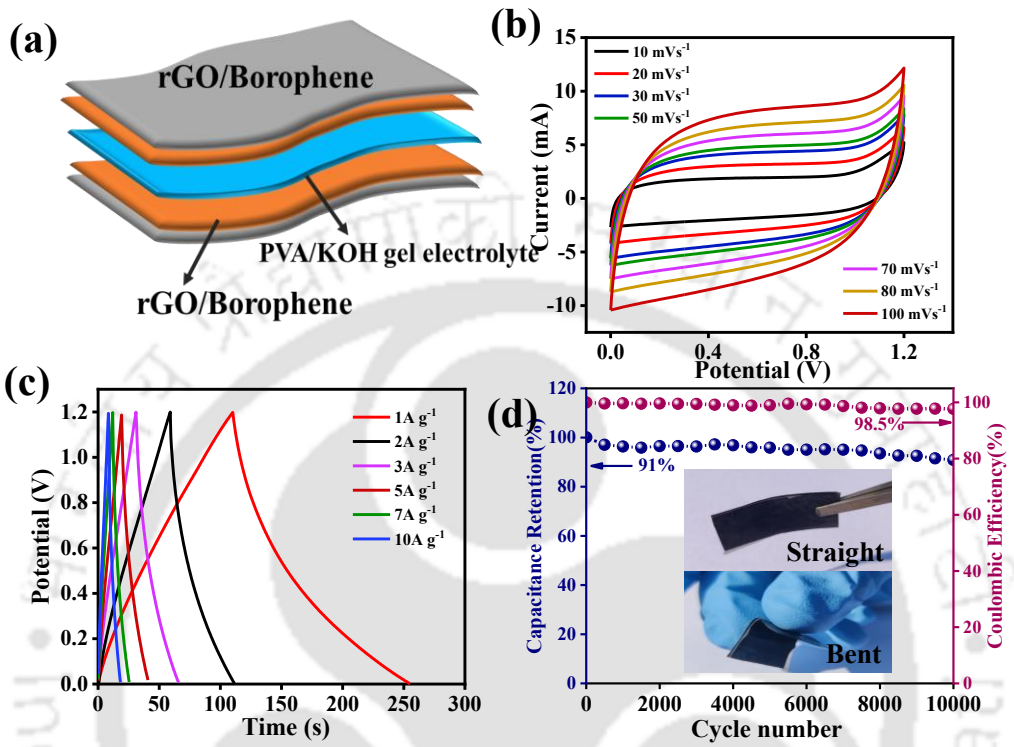

Figure 5a.11: (a) Schematic presentation of the device tested (b) CV curves of the rGO/Bp//rGO/Bp device from 10 to 100 mVs^{-1} (c) GCD curves of the rGO/Bp//rGO/Bp device from 1 to 10 Ag^{-1} (d) CV (e) GCD curve at different bending angles of rGO/Bp//rGO/Bp FSSc indicating constant energy output in different bending angle (f) Long-term cycling performance and Coulombic efficiency of the two-terminal device at 10 Ag^{-1} using 1 M PVA-KOH electrolyte (Photographic image of FSS)

Flexible symmetric supercapacitors (FSSs) have gained significant attention in energy storage and conversion due to their exceptional flexibility and excellent cycling stability. To showcase the practicality of the composite material, FSS device was constructed. The synthesized electrode gives a potential window ranging from −1.0 V to 0.2 V, which offers both positive and negative potential. Therefore, a FSS was developed with identical mass loading on both electrodes to evaluate the practical applicability of the rGO/Bp hybrid material. A gel electrolyte composed of polyvinyl alcohol (PVA) and potassium hydroxide (KOH) was

employed to fabricate the symmetric semi solid-state flexible device as shown in **Figure 5a.11a**. **Figure 5a.11b** illustrates the CV curves at different scan speeds of the constructed device, indicating the stable operating voltage window of FSS is 0–1.2V. As the scan speed increases, the CV curve profiles remain stable, indicating that the electrode has outstanding rate capability. **Figure 5a.11c** presents the GCD measurements of the device at current densities ranging from 1 Ag^{-1} to 10 Ag^{-1}, exhibiting a linear and symmetrical charge-discharge profile over time with minimal iR drop, reflecting high efficiency and excellent charge retention. The specific capacitance of the device calculated from the GCD curves achieves a high value of 121.6 Fg^{-1} at 1 Ag^{-1}. The FSS achieved an energy density of 24.3 Wh kg^{-1} at 0.6 kW kg^{-1}, retaining 17.6 Wh kg^{-1} of energy density even at a high-power density of 6.5 kW kg^{-1}. **Table 5a.2** compares the rGO/Bp//rGO/Bp device with other Boron and rGO-based supercapacitors, highlighting its superiority over previously reported materials. The fabricated device was bent at various angles (0°, 45°, 90°, and 180°) to evaluate its electrochemical performance under significant mechanical deformation, **Figure 5a.11(d-e)**. In **Figure 5a.11f**, the capacitance retention of the device is presented as a function of cycle number for 10000 charge-discharge cycles at a current density of 10Ag^{-1}. After 10000 consecutive cycles, approximately 91% of its initial capacitance was retained, and the Coulombic efficiency remained at 98.5%, demonstrating superior stability.

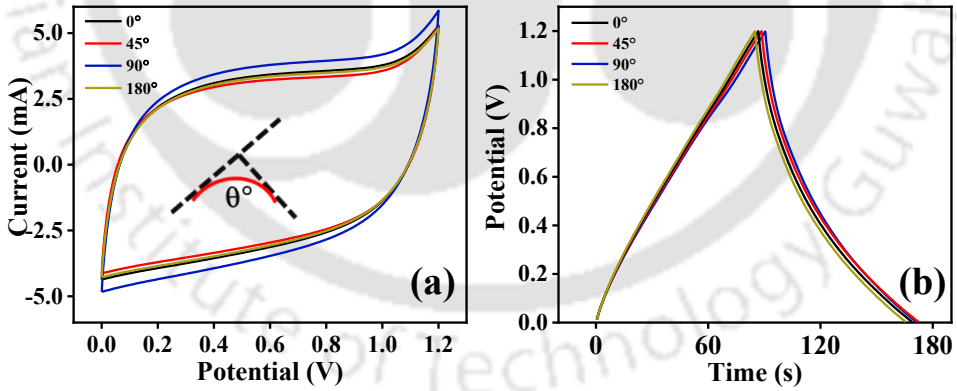

Figure 5a.12: (a) CV (b) GCD curve at different bending angles of rGO/Bp//rGO/Bp FSSc

The fabricated device was bent at various angles (0°, 45°, 90°, and 180°) to evaluate its electrochemical performance under significant mechanical deformation. The corresponding CV and GCD plots were recorded at different bending angles, and the results revealed no noticeable change in the device's performance. The device could bend up to 180° without compromising its physical integrity or operational efficiency.

Table 5a.2: Comparative study of SSCs devices with recently reported literature:

Electrode material	Capacitance (Fg^{-1})	Electrolyte	Energy Density ($Whkg^{-1}$)	Power density (Wkg^{-1})	Reference
rGO/Borophene// rGO/Borophene	**121.6 F g^{-1} @ 1A g^{-1}**	**1M KOH**	**24.3**	**600**	**This Work**
BGH//BGH(Borophene Graphene Hydrogel)	193 @ 0.5 Ag^{-1}	2M KOH	36.77	585.5	40
Borophene/MXene// Borophene/MXene	375 @ 1 Ag^{-1}	2M H_2SO_4	53.3	12,000	41
Few layers of boron	147.6 @0.3 A g^{-1}	1-butyl-3-methylimidazolium hexafluorophosphate	46.1	478.5	42
Nb_2CTx/rGO	26 @ Ag^{-1}	1M H_2SO_4	6	635	43
PANI/rGO//PANI/rGO	79.71 @ 1 Ag^{-1}	1 M H_2SO_4	5.09	147.53	44
N,P co-doped graphene	45@ 0.5 Ag^{-1}	6M KOH	8.17	162	45
Black Phosphorus/$Ti_3C_2T_X$	-	1 MH_2SO_4	6.39	111.24	46
Lig/SWCN/$HrGO_{al}$	222 @ 1 Ag^{-1}	1MH_2SO_4	8.23	125	47
$Ni_3(BO_3)_2$NSs@Ti// AC	86 @ 0.5 Ag^{-1}	6 M KOH	30.6	400	48
P,B doped rGO	103@ 1 Ag^{-1}	1M H_2SO_4	12.48	394	49

5a.2.8. Theoretical Calculations and mechanistic insights to charge storage:

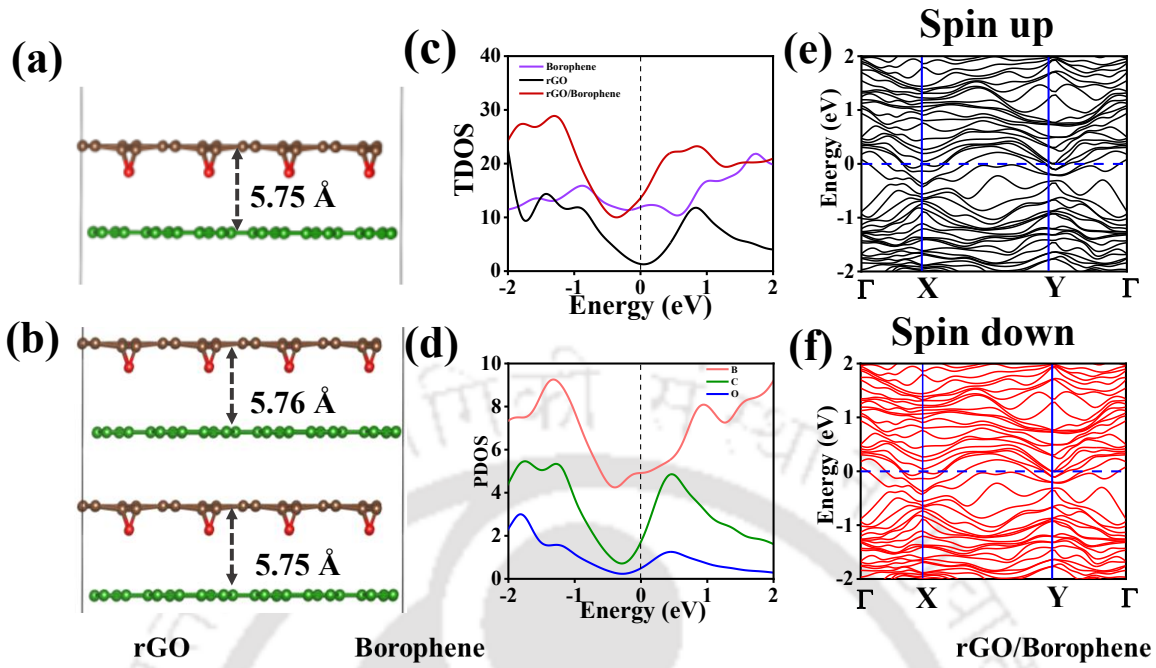

Figure 5a.12: (a) Hetero-layer structure of (a) borophene with rGO (one layer for both) (b) structure of borophene with rGO (two layers for both). (c) PDOS (d) TDOS for Borophene with rGO for the structure shown in Spin-polarized electronic band structure of rGO/Borophene for structure (a), (e) spin-up and (f) spin-down band structure.

We have performed DFT calculations to confirm the experimental findings and investigate the underlying mechanisms behind the enhanced capacitance observed in the rGO/Bp hybrid electrode. The heterostructure, comprising a rhombohedral β12-borophene and rGO layer as shown in **Figure 5a.12a**, was constructed, and optimized. After optimization, the bond lengths for B–B, and C–C in the heterostructure were found to be 1.68 Å and 1.45 Å, respectively, with an interlayer spacing of 5.75 Å. The relatively large interlayer distance observed in this structure, compared to other reported borophene/graphene composites, is attributed to the presence of epoxy oxygen, which induces charge repulsion.[50] When examining a four-layer β12-B/rGO configuration, the interlayer distance remained unchanged at 5.75Å, suggesting that this spacing distance is optimal for the β12-B and rGO heterostructure as shown in **Figure 5a.12b**. The 5.75Å (0.57 nm) interlayer spacing effectively suppresses restacking while maintaining the diffusion channels and ensuring sufficient ion accessibility, which maximizes capacitance in supercapacitor applications.[51]

The electronic properties of electrode materials are crucial for charge storage, as they determine electron availability and mobility. In **Figure 5a.12c** PDOS analysis shows that boron in the rGO/Bp composite contributes more significantly near the Fermi level than carbon or oxygen, indicating its key role in enhancing charge storage. TDOS calculations confirm that borophene has a higher DOS near the Fermi level than rGO, suggesting superior intrinsic conductivity. The composite retains the semi-metallic characteristics of borophene while exhibiting an improved DOS, enhancing its electronic properties as shown in **Figure 5a.12d**. Additionally, the composite shows increased electron density at the valence band edge, providing a greater number of accessible states for electron occupancy near the Fermi level, allowing electrons to participate in charge storage processes more readily.[52,53] We have carried out band structure calculations using the hetero-layer structure. A high-symmetry k-point path is chosen to examine the band dispersion characteristics near the Fermi level in the composite system. The spin-up and spin-down band structures are shown in **Figure 5a.12 (e-f)**, respectively. The computed spin-polarized band structure calculations of the Hetero-layer structure of borophene with rGO demonstrate the Dirac cone nature near the Fermi level irrespective of the spin counterpart. These findings reinforce our analysis and emphasize the potential influence of electronic interactions between borophene and graphene oxide.

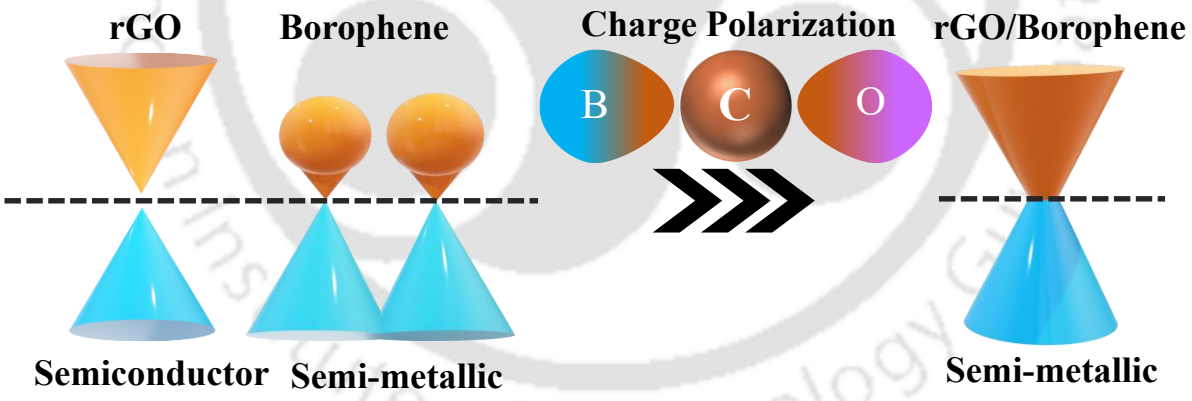

Figure 5a.13 Schematic diagram illustrating the regulation of the rGO semiconductor band edge properties through the integration of borophene, a Dirac material with high electrical conductivity, and the electrochemical benefits of the resulting rGO/borophene semi-metallic composite.

Based on the combined studies, a probable mechanism is schematically shown in **Figure 5a.13**. This figure illustrates the orbital interactions between B, C, and O atoms in the rGO/Bp composite, which modify its electronic properties and enhance charge storage performance.

The semi-metallic Dirac nature of borophene, combined with the semiconducting properties of rGO, synergistically gives rise to a composite with enhanced semi-metallic characteristics, resulting in superior performance.

5a.3. CONCLUSIONS:

In conclusion, the performance of rGO/borophene composite electrodes in supercapacitors is enhanced using Dirac semi-metallic borophene. The addition of borophene nanosheets to rGO improves ion diffusion and charge transfer, achieving a specific capacitance of 328 F g^{-1} at 1 A g^{-1} in 1 M KOH, which is nearly four times higher than that of rGO alone. The flexible supercapacitor reaches 121.6 F g^{-1} at 1 A g^{-1} and retains 91% of its capacitance after 10,000 cycles. DFT analysis reveals semi-metallic characteristics of composite, which increase electron density near the Fermi level and facilitate efficient energy storage. These findings underscore the viability of rGO/borophene composites in advancing flexible and efficient energy storage devices.

Author Contributions:

Alpana Sahu conceptualized and conducted the experiments, analyzed the results, and wrote the manuscript. Partha Pratim Borah and Kalishankar Bhattacharyya performed DFT calculations for DOS analysis. Mohammad Qureshi conceptualized and coordinated the experiments, evaluated the results, secured funding, and contributed to manuscript writing.

Acknowledgments:

I acknowledge Dr. Kalishankar Bhattacharyya and his student Partha Pratim Borah for doing the theoretical calculation; Dr. H.S.S. Ramakrishna Matte and Vijaya Kumar (CeNS Bangalore) for HRTEM analysis.

5a.4. REFERENCES:

1. L. Kou, T. Huang, B. Zheng, Y. Han, X. Zhao, K. Gopalsamy, H. Sun, C. Gao, *Nat. Commun.* **2014**, *5*, 3754.
2. J. A. Rogers, T. Someya, Y. Huang, *Science* **2010**, *327*, 1603.
3. S. Kumar, G. Saeed, L. Zhu, K. N. Hui, N. H. Kim, J. H. Lee, *Chemical Eng. J.* **2021**, *403*, 126352.
4. T.-H. Gu, N. H. Kwon, K.-G. Lee, X. Jin, S.-J. Hwang, *Coord. Chem. Rev.* **2020**, *421*, 213439.
5. Q. Fu, X. Bao, *Chem. Soc. Rev.* **2017**, *46*, 1842.

6. R. R. Nair, P. Blake, A. N. Grigorenko, K. S. Novoselov, T. J. Booth, T. Stauber, N. M. R. Peres, A. K. Geim, *Science* **2008**, *320*, 1308.
7. Y. Bin Tan, J.-M. Lee, *J Mater. Chem. A* **2013**, *1*, 14814.
8. S. Dongre S, S. R, C. Hunsur Ravikumar, L. C, R. G. Balakrishna, *Adv. Mater Interfaces* **2022**, *9*, 200442.
9. E. Liu, A. Negm, M. M. R. Howlader, *Mater. Today Energy* **2021**, *20*, 100625.
10. L. Li, Y. Yu, G. J. Ye, Q. Ge, X. Ou, H. Wu, D. Feng, X. H. Chen, Y. Zhang, *Nat. Nanotechnol.* **2014**, *9*, 372.
11. P. Sujita, S. Vadivel, S. Wacławek, B. Paul, *Inorg. Chem. Commun.* **2024**, *167*, 112739.
12. H. Li, L. Jing, W. Liu, J. Lin, R. Y. Tay, S. H. Tsang, E. H. T. Teo, *ACS Nano* **2018**, *12*, 1262.
13. M. Bhavyashree, S. R. Rondiya, K. Hareesh, *RSC Adv.* **2022**, *12*, 12166.
14. X. Liu, Z. Zhang, L. Wang, B. I. Yakobson, M. C. Hersam, *Nat. Mater.* **2018**, *17*, 783.
15. Y. Huang, S. N. Shirodkar, B. I. Yakobson, *J. Am. Chem. Soc.* **2017**, *139*, 17181.
16. K. I. Bolotin, K. J. Sikes, Z. Jiang, M. Klima, G. Fudenberg, J. Hone, P. Kim, H. L. Stormer, *Solid State Commun.* **2008**, *146*, 351.
17. T. Cheng, H. Lang, Z. Li, Z. Liu, Z. Liu, *Phy. Chem. Chem. Phy.* **2017**, *19*, 23942.
18. H. Zhang, Y. Xie, Z. Zhang, C. Zhong, Y. Li, Z. Chen, Y. Chen, *J Phys. Chem. Lett.* **2017**, *8*, 1707.
19. F. Ma, Y. Jiao, G. Gao, Y. Gu, A. Bilic, Z. Chen, A. Du, *Nano Lett.* **2016**, *16*, 3022.
20. C. Zhan, P. Zhang, S. Dai, D. Jiang, *ACS Energy. Lett.* **2016**, *1*, 1241.
21. G. H. Gupta, S. Kadakia, D. Agiwal, T. Keshari, S. Kumar, *Mater. Adv.* **2024**, *5*, 1803.
22. G. Tai, T. Hu, Y. Zhou, X. Wang, J. Kong, T. Zeng, Y. You, Q. Wang, *Angewandte Chemie International Edition* **2015**, *54*, 15473.
23. Y. Abdi, A. Mazaheri, S. Hajibaba, S. Darbari, S. J. Rezvani, A. Di Cicco, F. Paparoni, R. Rahighi, S. Gholipour, A. Rashidi, M. M. Byranvand, M. Saliba, *ACS Mater. Lett.* **2022**, *4*, 1929.
24. H. Li, L. Jing, W. Liu, J. Lin, R. Y. Tay, S. H. Tsang, E. H. T. Teo, *ACS Nano* **2018**, *12*, 1262.
25. W. S. Hummers, R. E. Offeman, *J. Am. Chem. Soc.* **1958**, *80*, 1339.
26. W. S. Hummers, R. E. Offeman, *Preparation of Graphitic Oxide*, **1958**.
27. G. Kresse, J. Hafner, *Phys. Rev. B* **1993**, *47*, 558.
28. G. Kresse, J. Furthmüller, *Phys. Rev. B* **1996**, *54*, 11169.
29. G. Kresse, D. Joubert, *Phys. Rev. B* **1999**, *59*, 1758.
30. J. P. Perdew, K. Burke, M. Ernzerhof, *Phys. Rev. Lett.* **1996**, *77*, 3865.
31. V. Wang, N. Xu, J.-C. Liu, G. Tang, W.-T. Geng, *Comput. Phys. Commun.* **2021**, *267*, 108033.
32. K. Zielinkiewicz, E. Mijowska, *Sustainable Materials and Technologies* **2024**, *39*, e00860.
33. S. Sheng, J.-B. Wu, X. Cong, Q. Zhong, W. Li, W. Hu, J. Gou, P. Cheng, P.-H. Tan, L. Chen, K. Wu, *ACS Nano* **2019**, *13*, 4133.

34. Z. Wu, G. Tai, R. Liu, C. Hou, W. Shao, X. Liang, Z. Wu, *ACS Appl. Mater. Interfaces* **2021**, *13*, 31808.
35. S. T.E., D. T. Tran, S. Jena, Y. Bai, S. Prabhakaran, D. H. Kim, N. H. Kim, J. H. Lee, *Chemical Engineering Journal* **2024**, *481*, 148266.
36. H. Lin, H. Shi, Z. Wang, Y. Mu, S. Li, J. Zhao, J. Guo, B. Yang, Z.-S. Wu, F. Liu, *ACS Nano* **2021**, *15*, 17327.
37. T. Wu, X. Wu, L. Li, M. Hao, G. Wu, T. Zhang, S. Chen, *Angewandte. Chemie.* **2020**, *132*, 24008.
38. W. Shao, Z. Wu, Y. Liu, G. Tai, *Chemical Engineering Journal* **2024**, *500*, 157258.
39. Y. Lu, C.-Z. Zhao, J.-Q. Huang, Q. Zhang, *Joule* **2022**, *6*, 1172.
40. O. P. Nanda, C. Y. Kong, S. Badhulika, *ACS Appl Energy Mater* **2024**, *7*, 7844.
41. S. T.E., D. T. Tran, S. Jena, Y. Bai, S. Prabhakaran, D. H. Kim, N. H. Kim, J. H. Lee, *Chemical Engineering Journal* **2024**, *481*, 148266.
42. H. Li, L. Jing, W. Liu, J. Lin, R. Y. Tay, S. H. Tsang, E. H. T. Teo, *ACS Nano* **2018**, *12*, 1262.
43. K. Nasrin, M. Arunkumar, N. Koushik Kumar, V. Sudharshan, S. Rajasekar, D. Mukhilan, M. Arshad, M. Sathish, *Chemical Engineering Journal* **2023**, *474*, 145505.
44. H. H. Hsu, A. Khosrozadeh, B. Li, G. Luo, M. Xing, W. Zhong, *ACS Sustain. Chem. Eng.* **2019**, *7*, 4766.
45. K. Xia, Z. Huang, L. Zheng, B. Han, Q. Gao, C. Zhou, H. Wang, J. Wu, *J. Power Sources* **2017**, *365*, 380.
46. Q. Tang, Y. Zhang, X. Zhu, Y. Wang, Z. Man, C. Yang, J. Xu, G. Wu, W. Lu, *Adv. Funct. Mater* **2024**, 2410005.
47. Z. Peng, C. Yu, W. Zhong, *ACS Appl Mater Interfaces* **2022**, *14*, 17739.
48. X. Sun, K. Zhao, Z. Liu, Z. Feng, Z. Wang, L. Cui, J. Liu, *J Energy Storage* **2022**, *55*, 105763.
49. S. Surya, A. Pandurangan, R. Govindaraj, *J Energy Storage* **2024**, *86*, 111319.
50. J. Yu, M. Zhou, M. Yang, Q. Yang, Z. Zhang, Y. Zhang, *ACS Appl. Energy Mater.* **2020**, *3*, 11699.
51. J. Yan, C. E. Ren, K. Maleski, C. B. Hatter, B. Anasori, P. Urbankowski, A. Sarycheva, Y. Gogotsi, *Adv Funct. Mater.* **2017**, *27*, 701264.
52. P. A. Shinde, N. R. Chodankar, H.-J. Kim, M. A. Abdelkareem, A. Al Ghaferi, Y.-K. Han, A. G. Olabi, K. Ariga, *ACS Energy Lett.* **2023**, *8*, 4474.
53. I. Hussain, M. Z. Ansari, C. Lamiel, T. Hussain, M. S. Javed, T. Kaewmaraya, M. Ahmad, N. Qin, K. Zhang, *ACS Energy Lett.* **2023**, *8*, 1887

CHAPTER 5b

Homo-interface engineering of O-Doped and B-Doped graphitic carbon nitride composite for energy storage

Utilizing the intrinsic electric field of a p–n junction electrode, which enhances charge transport at the interface, this paper presents a novel method for improving electrochemical energy storage. This study presents the rational design of a heterostructure electrode material that consists of n-type oxygen-doped g-C_3N_4 (O: g-C_3N_4) nanosheets combined with p-type boron-doped g-C_3N_4 (B:g-C_3N_4) hollow nanotubes, resulting in a well-defined homo-interface (p–n) junction. The unique hollow tubular morphology of B:g-C_3N_4 coupled with the layered structure of O:g-C_3N_4, affords a high surface area and short ion diffusion paths. The redistribution of charge within the p-n junction leads to the formation of space-charge regions and an internal electric field, which promotes charge transfer and subsequently increases intrinsic activity.

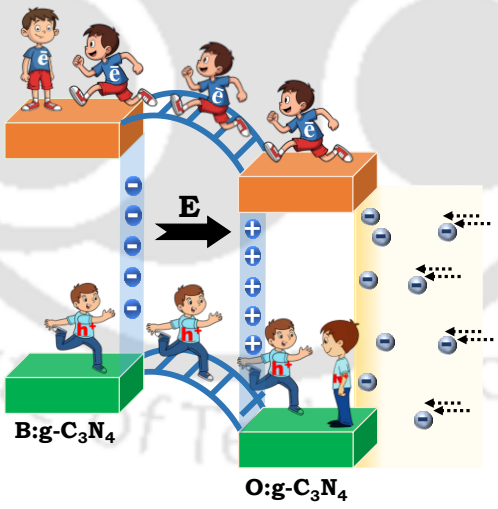

5b.1. INTRODUCTION:

Growing energy demand requires devices that combine high energy and power density, long cycle life, and rapid performance.[1]An electrochemical supercapacitor stands out for its significantly higher energy density compared to conventional capacitors and a power density higher than that of traditional batteries, resulting in fast charge–discharge capability and a long cycle life.[2–4] However, supercapacitor performance largely depends on the electrochemical properties of the electrode materials, such as electrical conductivity, accessible active sites, and efficient ionic transport within the electrolyte that directly affect the cell voltage, energy and power output.[5,6] To enhance the energy and power density of a typical supercapacitor, various material engineering strategies such as elemental doping, defect engineering, morphology tuning, and interface design[7] have been employed.[7–10] Among these, junction engineering has gained attention for its ability to create an internal, built-in electric field that promotes charge separation, electron/ion transport, thereby improving conductivity and boosting charge storage performance.[11] In this regard, 2D materials and associated morphological heterostructures, modulated with *p-n* junction strategies, show promise for high-performance energy storage. For instance, Hussain *et al.* proposed a heterojunction between 1D *p*-type CuO and 3D *n*-type Zn–In–S was formed with a remarkable performance and improved conductivity.[12] Bai *et al.* developed a g-C_3N_4/Co_3O_4 *p–n* junction electrode delivering 1519.5 mF cm^{-2} at 1.5 mA cm^{-2}, yet the symmetric CoCN//CoCN device achieved only 12.9 Wh kg^{-1}, highlighting the fact that even in heterojunction designs, charge transport and energy density are still constrained by the low intrinsic conductivity of g-C_3N_4.[13] Similarly, Hong *et al*. synthesized B-doped g-C_3N_4 quantum dots modified with $Ni(OH)_2$ nanoflowers with enhanced structural and electronic properties with a *p-n* junction, delivering high capacitance and excellent cycling stability, illustrating the effectiveness of g-C_3N_4-based composites in boosting supercapacitor performance.[14]However, in some heterojunctions, interfacial mismatch and lattice distortion raise contact resistance and block ion diffusion, reducing capacitance, energy, and power density.[15,16] Therefore, designing junction architectures with interfacial compatibility and efficient charge-transfer pathway is critical. In this context, homojunction engineering offers a distinct advantage over heterojunction, where both regions are made from the same host material with differently doped atoms, inherently providing better structural stability, reduced interfacial resistance, and simpler synthesis protocols.[17] Li *et al.* reported a 1T@2H MoS_2 homojunction by a Te-assisted thermal treatment, achieving high conductivity (0.0357 kΩ·cm) and capacitance 1053.8 F g^{-1} with an excellent cycling stability.

This work highlights how phase-engineered homojunctions can enhance charge transport and electrochemical performance.[18]

Building on this concept, engineering g-C_3N_4-based homojunctions by integrating domains with distinct dopant compositions or structural order holds significant potential for overcoming its intrinsic conductivity limitations and achieving higher capacitance and stability in supercapacitors. g-C_3N_4, a low-cost, metal-free, and chemically stable 2D electrode material with a ~2.7 eV bandgap, has attracted attention for its adjustable bandgap, tunable morphology, and environmental benignity, making it suitable for energy storage.[19–21] To enhance the charge storage of g-C_3N_4, different strategies such as composite formation, elemental doping, and nano-structural modification have been adopted.[22] Doping alters its electronic configuration, enhancing charge carrier mobility and surface reactivity.[23] Various non-metal dopants such as oxygen, sulphur, phosphorus, nitrogen, carbon, and boron-doped g-C_3N_4 have been reported to tailor its physicochemical characteristics.[24–28] Among these, dopants like boron and oxygen are particularly effective due to their comparable atomic size, which leverages chemical compatibility and strong bonding with g-C_3N_4 effectively tuning to material properties. Boron contributes an empty p-orbital to the conjugated system, while oxygen donates lone pair electrons that enhance electron delocalization and improve electrical conductivity.[29–31] In addition, modifying the morphology into nanostructures such as tubes, wires, rods, and spheres is more efficient than bulk materials, owing to their high surface area, which helps overcome the low practical surface area and provides more active sites for energy storage.[32,33]

Considering the above discussion, herein we fabricate a homojunction consisting of *p*-type B-doped g-C_3N_4 **(B:g-C_3N_4)** hollow nanotubes decorated on *n*-type O-doped g-C_3N_4 **(O:g-C_3N_4)** nanosheets to maximize electrochemical performance. Firstly, doping alters the electronic structure of g-C_3N_4 by decreasing the band gap, where **O:g-C_3N_4** and **B:g-C_3N_4** exhibit a narrower band gap of 2.6 eV and 2.3 eV, respectively. Secondly, morphological modification of **B:g-C_3N_4** into hollow nanotubes, combined with the sheet-like structure of **O:g-C_3N_4**, provides a larger active surface area and short ion diffusion pathways. Thirdly, the formation of a *p–n* junction facilitates electron transfer by creating a built-in electric field at the interface, thereby enhancing the synergistic interaction between **B:g-C_3N_4** and **O:g-C_3N_4**. The resulting **B:g-C_3N_4/O:g-C_3N_4** composite electrode delivers a high specific capacitance of 366 F g^{-1} at a current density of 1 A g^{-1}. For practical application, an asymmetric supercapacitor device (**B:g-C_3N_4/O:g-C_3N_4// AC**) is assembled, achieving an energy density of 24 Wh kg^{-1} at

a power density of 700 W kg^{-1}. The device retains 83% of its specific capacitance and maintains a coulombic efficiency of 100% after 20,000 GCD cycles, demonstrating excellent electrochemical stability. This work highlights the potential of *p–n* junction engineering to improve the energy storage properties of electrode materials.

5b.2. EXPERIMENTAL:

5b.2.1. Synthesis of O-doped g-C_3N_4:

For the synthesis of O:g-C_3N_4, we first prepared bulk g-C_3N_4 powder. To achieve this, 3 g of melamine was calcined at 550°C for 3 hours, the obtained product was then ground into a fine powder and further calcined at 500°C for 1 hour to obtain exfoliated g-C_3N_4. For the oxygen doping process, we employed a microwave synthesis method. In this process, 200 mg of g-C_3N_4 was dispersed in 5 mL of 30% H_2O_2 solution in a 25 mL beaker. The mixture was then irradiated with a 350 W microwave for 30 minutes.

5b.2.2. Synthesis of B-doped g-C_3N_4:

Boric acid was used as a boron dopant for the synthesis of B:g-C_3N_4. 3 g of melamine was dissolved in 30 ml of ethylene glycol to make a saturated solution. 60 ml of 0.1 M HNO_3 was then added to the prepared solution. After stirring for 10 min, the mixture was washed with ethanol and dried at 60 °C. A boric acid to obtained melamine adduct at different ratios was dissolved in 30 mL of water and stirred for 3 hours, followed by overnight drying at 70°C. The resulting powder was then transferred to an alumina crucible and calcined at 550°C for 4 hours in an argon (Ar) atmosphere. After cooling to room temperature, the powder was ground into a fine form and designated as B: g-C_3N_4.

5b.2.3. Synthesis of B-doped g-C_3N_4 and O doped g-C_3N_4 composite:

The composite B:g-C_3N_4 /O:g-C_3N_4 was prepared using an electrostatic self-assembly approach. Initially, both O:g-C_3N_4 and B:g-C_3N_4 exhibited negative zeta potentials of −22 mV and −18 mV, respectively. B:g-C_3N_4 (100 mg) was dispersed in 5 mL of 1 M HCl and stirred overnight at room temperature for complete protonation, resulting in a surface potential shift to +10 mV. To fabricate the B:g-C_3N_4 /O:g-C_3N_4 composite, B:g-C_3N_4 and O:g-C_3N_4 were mixed in different ratios, sonicated for 1 hour, and then centrifuged, washed, and dried to obtain the final composite.

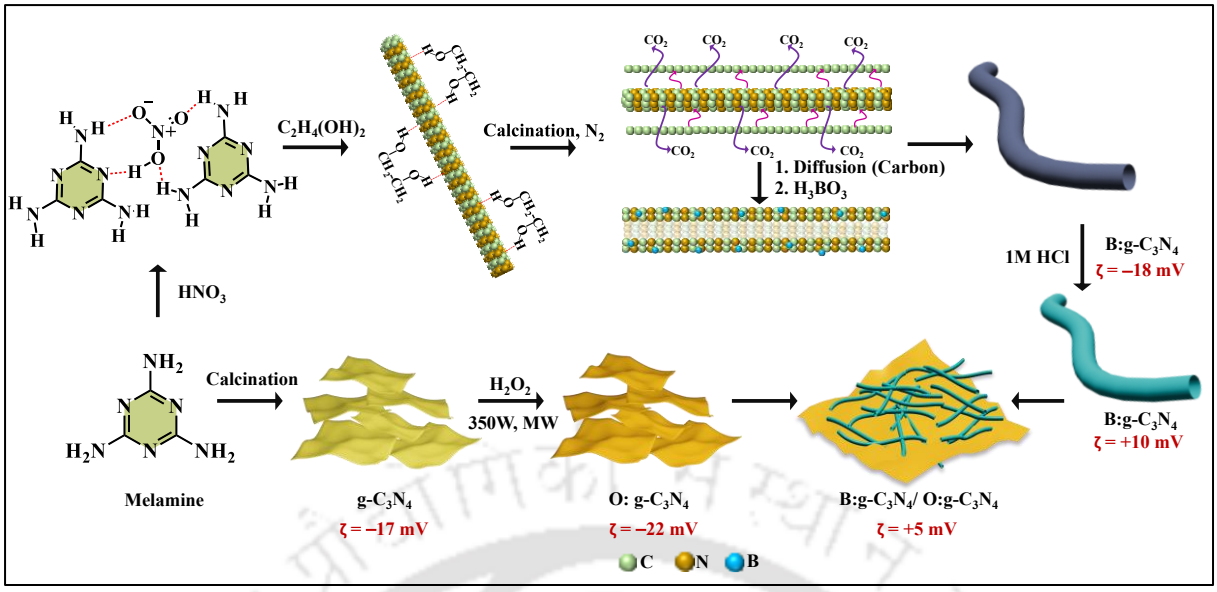

Scheme 5b.1: Schematic illustration of the synthesis routes for B:g-C_3N_4, O:g-C_3N_4, and the B:g-C_3N_4/O:g-C_3N_4 composite. O:g-C_3N_4 is prepared via a microwave-assisted synthesis using H_2O_2 as the oxygen dopant, followed by calcination. B:g-C_3N_4 is synthesized through direct calcination using boric acid as the boron dopant, with ethylene glycol (EG) serving as a structure-directing agent. EG facilitates the inward diffusion of carbon during calcination, leading to the formation of a hollow tubular structure. After this, the homojunction B:g-C_3N_4/O:g-C_3N_4 composite is fabricated via an electrostatic self-assembly approach.

5b.3. RESULTS AND DISCUSSION:

5b.3.1. Morphological Analysis:

Scheme 5b.1 illustrates step-by-step synthesis of O:g-C_3N_4/B:g-C_3N_4 homojunction composite. Initially, O:g-C_3N_4 is prepared from bulk g-C_3N_4 (GCN) using a microwave-assisted method, while B : g-C_3N_4 is synthesized through a calcination process. During the synthesis of O:g-C_3N_4, a mixture of GCN and an oxygen-rich precursor, H_2O_2 is exposed to microwave irradiation, leading to rapid heating, promoting uniform doping of oxygen atoms into the GCN framework.[34] Additionally, the zeta potential value of GCN (−17 mV) is shifted to −22 mV after oxygen doping, further confirming the incorporation of oxygen atoms, which leads to a more negative surface charge. Meanwhile, B:g-C_3N_4 nanotubes with varying B and N contents are synthesized through a modified pyrolysis approach. The tubular structure of B:g-C_3N_4 is formed by treating melamine with HNO_3 in the presence of ethylene glycol (EG), followed by an annealing process. In the first step, the addition of HNO_3 leads to the

protonation of the amine and triazine nitrogen groups in melamine, making it chemically more reactive and less

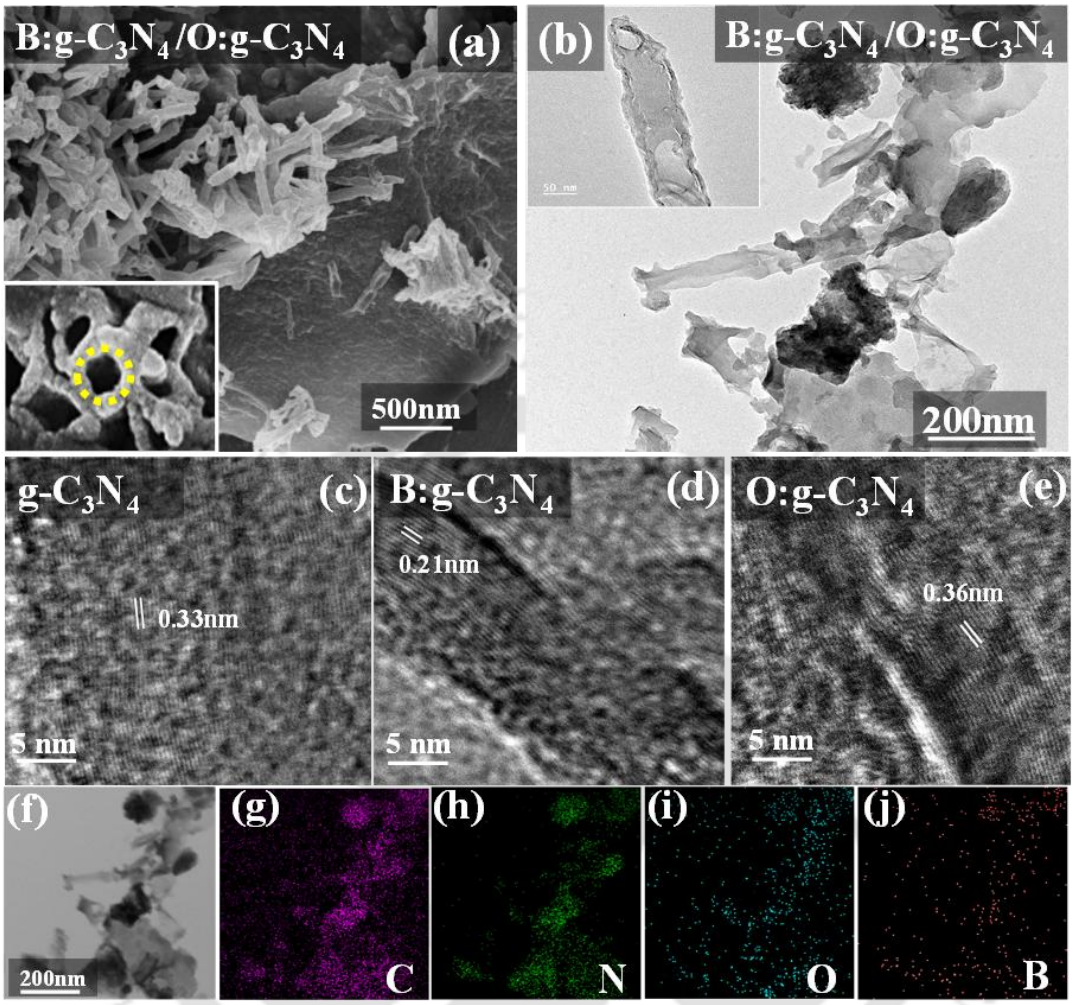

Figure 5b.1: (a) FESEM and (b) FETEM image of B:g-C_3N_4 /O:g-C_3N_4 showing O:g-C_3N_4 sheets with B:g-C_3N_4 nanotubes (inset showing tubular B:g-C_3N_4 with a diameter of 70-80 nm) (c) High resolution TEM analysis of (c) g-C3N4 (d) B:g-C_3N_4 (e) O:g-C_3N_4 showing change in the interplanar spacing after B and O doping, STEM EDX elemental mapping of (f) indicating presence of (g) Carbon (h) Nitrogen (i) Oxygen (j) Boron

stable. In the next step, EG initiates the polymerization with the activated melamine, guiding the formation of tubular structures. EG not only acts as a directing agent but also provides an additional carbon source, stabilizing the morphology during the heating process. During the annealing process, thermal decomposition of EG generates carbon species, which diffuse outward from the inner region of the forming structure. The outward carbon diffusion as CO_2 is counterbalanced by the inward diffusion of EG, and this contributes towards a hollow tubular

morphology.[33] In this process, boric acid serves as a boron source, enabling effective doping into the GCN framework by incorporating boron atoms into its structure during pyrolysis.[35] Subsequent treatment of B:g-C_3N_4 with 1M HCl protonates surface nitrogen species, inducing a positive surface charge, whereas O:g-C_3N_4 exhibited a negative surface charge, facilitating a non-covalent interaction between the two materials and promoting their self-assembly into the B:g-C_3N_4/O:g-C_3N_4 composite.

FESEM reveals the morphology of B:g-C_3N_4, O:g-C_3N_4, and B:g-C_3N_4/O:g-C_3N_4 composite. B:g-C_3N_4 has a nanotube-like morphology, which distinguishes it from the typical sheet-like structure observed in O:g-C_3N_4. This morphology is also retained in the composite, where B:g-C_3N_4 nanotubes are distributed over the O:g-C_3N_4 sheets **(Figure 5b.1a)**, indicating the successful formation of the B:g-C_3N_4 /O:g-C_3N_4 composite. The distribution of B:g-C_3N_4 nanotubes in the composite was further confirmed from FETEM images **(Figure 5b.1b).** Remarkably, the composite consists of nanotubes with diameters ranging from 70–80 nm that are distributed over the surface of O:g-C_3N_4. Such an orientation of B:g-C_3N_4 nanotubes over the O:g-C_3N_4 surface is crucial for maintaining a high electrical connection between B:g-C_3N_4 and O:g-C_3N_4. The hollow structure of nanotubes and nano-sheets contributes to a high surface area and accessible active sites, making the composite highly suitable for electrochemical energy storage. Doping-induced structural changes in GCN have been analysed through high-resolution transmission electron microscopy (HRTEM). Pristine GCN exhibits an interplanar spacing of 0.33 nm, corresponding to the (002) plane. After B-doping, the spacing decreases to 0.21 nm, whereas O-doping increases the interplanar spacing to 0.36 nm, as shown in **Figure 5b.1(c-e)**. These observations from HRTEM are consistent with the XRD results, further validating the structural modifications induced by B and O doping. The scanning transmission electron microscopy (STEM) elemental mapping confirms the uniform distribution of B, C, N, and O across the hybrid (**Figure 5b.1(f-j)**), suggesting the homogeneous distribution of B:g-C_3N_4 and O:g-C_3N_4 in the composite.

5b.3.2. Phase and Structural Analyses:

To investigate the structural changes resulting from B and O doping in GCN, XRD analysis is performed. **Figure 5b.2a** shows that bulk GCN exhibits a (100) peak at 13.2°, corresponding to the in-plane structural packing of the heptazine network, while the (002) peak at 27.75° indicates a well-defined layered structure. **Figure 5b.2b** shows that upon B doping, the peak corresponding to (002) plane shifts by 0.05° toward higher 2θ values, accompanied by peak

broadening. In contrast, O doping causes a 0.1° shift of the (002) peak toward lower 2θ values, indicating an increase in the interlayer spacing of the GCN framework. **Figure 5b.2c** illustrates the different types of electronic interactions that explain the observed shifts in XRD peaks upon B and O doping. In the case of B doping, an interaction occurs between the lone pair (lp) of nitrogen and the unoccupied p-orbital of boron, resulting in weak repulsion. This leads to lattice contraction, and repulsion is weaker compared to that in bare GCN, where bond pair (bp) –lone pair (lp) interactions exist between carbon and nitrogen. In contrast, O doping introduces additional lone pairs, leading to strong lp–lp repulsion with a bp-lp interaction, the highest among the three cases, which causes an expansion of the layers.

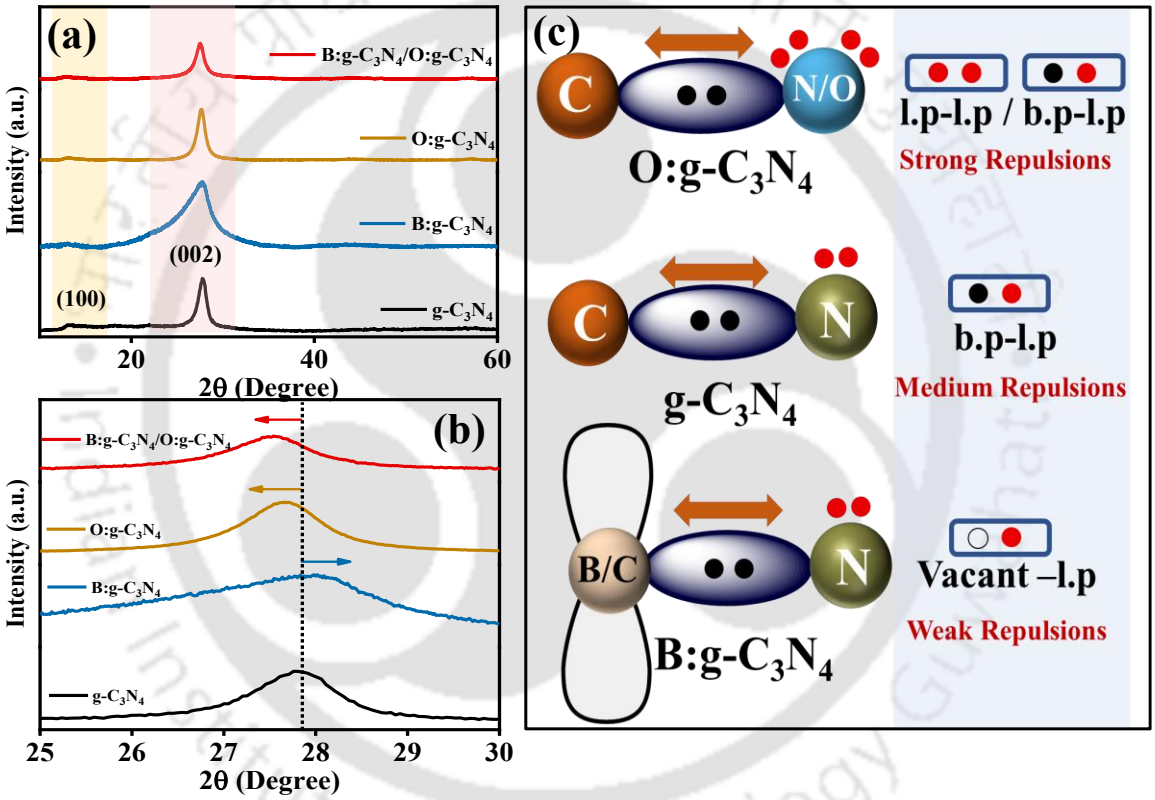

Figure 5b.2: (a) Comparative XRD patterns, (b) enlarged XRD at 23.75° to show the peak shift of (002) plane after B and O doping, (c) illustrates the different types of electronic interactions that correspond to shifts in XRD peaks upon B and O doping.

5b.3.3. Electronic State Analysis:

X-ray photoelectron spectroscopy (XPS) is employed to investigate the chemical states and electronic interaction in O:g-C_3N_4, B:g-C_3N_4, and O:g-C_3N_4/B:g-C_3N_4. The XPS survey spectra of O:g-C_3N_4 and B:g-C_3N_4 confirm the presence of oxygen and boron in the GCN. In the case of O:g-C_3N_4, the oxygen percentage is found to be 7.5%, whereas in B:g-C_3N_4 the boron content is found to be 6.7%, demonstrating substantial incorporation B and O into the GCN framework. **Figure 5b.3a** shows the high-resolution C1s spectra, which are deconvoluted into three peaks assigned with binding energy, 284.8 eV (sp^3 C–C), 286.2 eV (C–N) and 288.0 eV (N=C–N).With boron doping in GCN, an upshift in the C 1s binding energy is observed due to the electron-deficient nature of boron, which reduces the local electron density at carbon centre. Similarly, doping of oxygen into GCN, the C 1s spectrum shifts to higher binding energy as electronegative oxygen atoms withdraw electron density from neighbouring carbon atoms, making it more electron-deficient.[36]

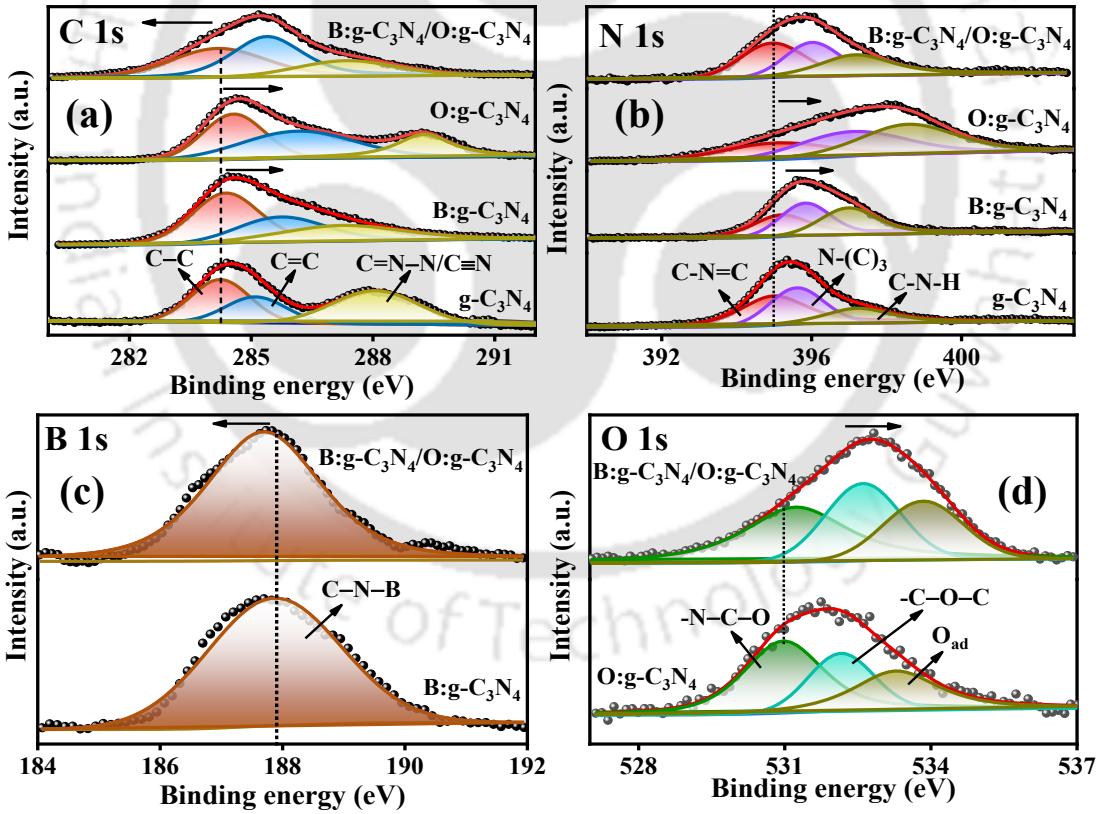

Figure 5b.3: High-resolution XPS spectra of (a) C1s (b) N1s (c) B1s (d) O1s showing synergistic interaction between B:g-C_3N_4 and O:g-C_3N_4.

Furthermore, in the B:g-C_3N_4/O:g-C_3N_4 composite, the C 1s spectrum shifts further to lower binding energy compared to pristine GCN, which is due to the combined effect of electron-deficient boron, electronegative oxygen, and interfacial charge redistribution between B:g-C_3N_4 and O:g-C_3N_4.Similarly, N 1s has been resolved to three peaks at 398.60, 399.4, and 400.43 eV, which correspond to three different types of nitrogen: aromatic (C–N=C), sp^2-hybridized N–$(C)_3$ or H–N–$(C)_2$, and terminal (–NH_2), **Figure 5b.3b**. A similar shift is observed in the N 1s spectra upon boron and oxygen doping of GCN, reflecting trends consistent with those seen in the C 1s spectra. **Figure 5b.3c** shows high-resolution B 1s XPS spectra with a peak assigned to C–N–B group, same as previously reported literature.[29] In the B:g-C_3N_4/O:g-C_3N_4 composite, the B 1s spectrum exhibits a shift toward lower binding energy compared to pristine B:g-C_3N_4, indicating boron sites in the composite experience an increase in electron density due to interactions between O:g-C_3N_4 and B:g-C_3N_4. **Figure 5b.3d** shows the O 1s XPS spectrum, which is deconvoluted into three peaks with binding energies at 531.9 eV (C–O–C), 533.4 eV (N–C–O), and 534.1 eV, attributed to adsorbed O_2 species in the lattice.[37,38] The O 1s peak of the composite is shifted to a higher binding energy as compared to O:g-C_3N_4, suggesting a decrease in electron density due to strong electronic interaction between O:g-C_3N_4 and B:g-C_3N_4. These shifts in binding energies confirm synergistic interactions among the two components, resulting in effective interfacial charge transfer and modification of the local electronic environment within the composite.

6.3.4. Electrochemical Analysis:

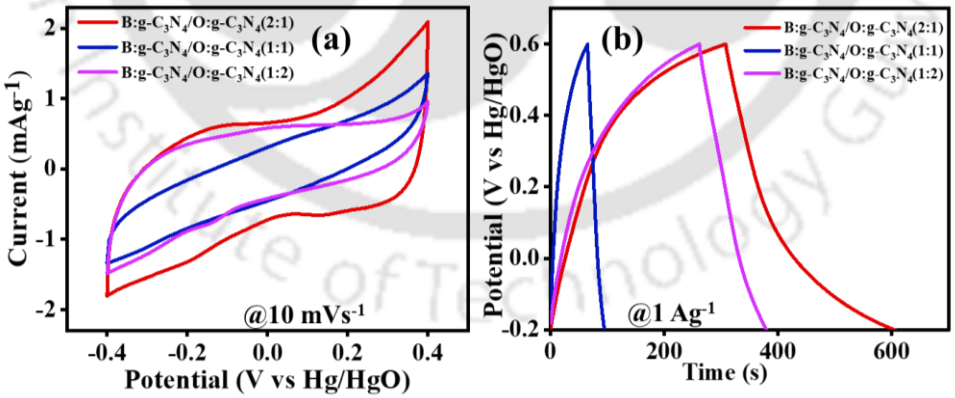

Figure 5b.4: (a) CV (b) GCD analysis of B:g-$C_3N_4$to O:g-C_3N_4 at different ratios for optimization of the electrode

The electrochemical properties of O:g-C_3N_4, B:g-C_3N_4, and B:g-C_3N_4/O:g-C_3N_4 composite are evaluated using a three-electrode setup in 2 M KOH aqueous electrolyte. Among various composite ratios studied, 2:1 ratio of B:g-C_3N_4 to O:g-C_3N_4 exhibited the highest specific

capacitance, as demonstrated by the largest CV area with longer charge discharge time, as shown in **Figure 5b.4**. **Figure 5b.5a** shows the comparative cyclic voltammetry (CV) analysis of the B:g-C_3N_4 /O:g-C_3N_4 composite and its bare counterparts in a voltage window of −0.4 to 0.4 V (vs. Hg/HgO), showing a larger integrated surface area for B:g-C_3N_4/O:g-C_3N_4 composite, indicating an enhanced capacitive behavior. **Figure 5b.5b** shows the CV profiles of the B:g-C_3N_4/O:g-C_3N_4 composite at scan rates ranging from 10 to 100 mV s^{-1}, exhibiting a quasi-rectangular shape that indicates dominant electric double-layer capacitive (EDLC) behavior of the composite material.

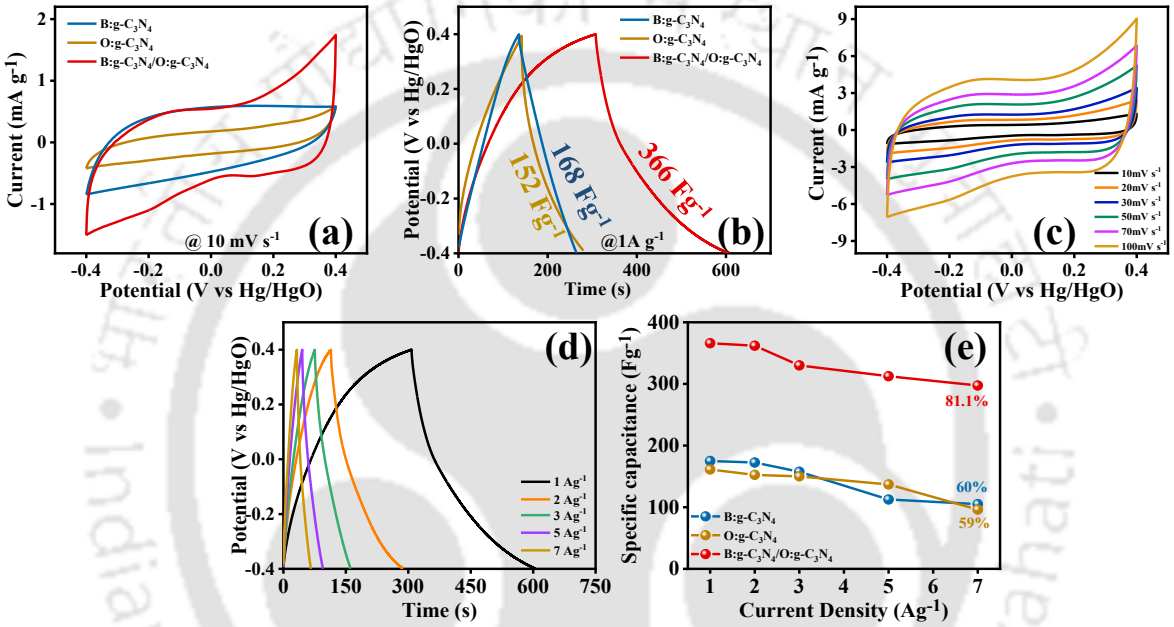

Figure 5b.5: (a) Comparison of CV curves at 10 mVs^{-1} (b) CV curves of the B:g-C_3N_4 /O:g-C_3N_4 electrode from 10 to 100 mVs^{-1} scan rate (c) comparative GCD curve at 1 Ag^{-1} of pristine B:g-C_3N_4, O:g-C_3N_4 and the B:g-C_3N_4 /O:g-C_3N_4 composite (d) GCD curves of the B:g-C_3N_4/O:g-C_3N_4 electrode from 1 to 10 Ag^{-1} (e) Plot of retention in capacitance with varying current density

The comparative galvanostatic charge/discharge (GCD) curves at 1 A g^{-1} (**Figure 5b.5c)** show that B:g-C_3N_4/O:g-C_3N_4 has a prolonged discharge time, confirming its enhanced specific capacitance. Based on the GCD discharge curve, the B:g-C_3N_4 /O:g-C_3N_4 demonstrated a specific capacitance of 366 F g^{-1} at 1 A g^{-1}, which is ~2 times higher than that of O:g-C_3N_4(161 F g^{-1}) and B:g-C_3N_4 (175 F g^{-1}). **Figure 5b.5d** illustrates the GCD curve of B:g-C_3N_4/O:g-C_3N_4, shows symmetric profiles across varying current densities of 1–7 Ag^{-1}, indicating high reversibility and low resistive losses. The specific capacitance values derived from GCD curves

across the current density range are used to evaluate capacitance retention, a key metric of rate capability, which reflects the ability of the material to maintain performance at higher charge–discharge rates. As shown in **Figure 5b.5e**, the B:g-C_3N_4/O:g-C_3N_4 composite retains 81.1± 5% of its initial capacitance at 7 A g^{-1}, significantly outperforming O:g-C_3N_4 (59±5%) and B:g-C_3N_4 (60±5%), highlighting its superior potential for high-rate supercapacitor applications.

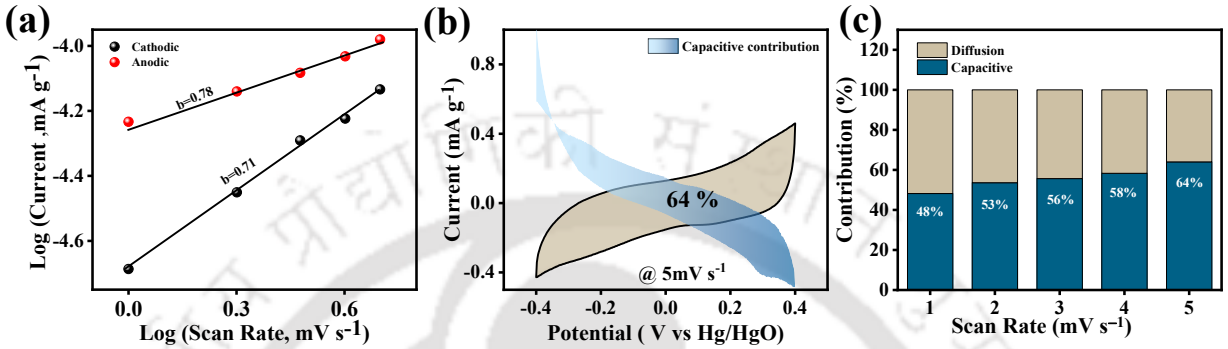

Figure 5b.6: (a) Logarithmic relationship between the peak current density and scan rate, (b) capacitive-controlled contribution at a sweep rate of 5 mVs^{-1} of B:g-C_3N_4 /O:g-C_3N_4 (c)Segregation of capacitive and diffusion-controlled area of B:g-C_3N_4/O:g-C_3N_4 at a scan rate

As shown in **Figure 5b.6a**, the b-values calculated for B:g-C_3N_4/O:g-C_3N_4 composite are 0.78 and 0.71, close to 1, indicating surface-controlled pseudocapacitance. Furthermore, Dunn's analysis offers a quantitative understanding of the charge storage mechanism, revealing that the capacitive contribution accounts for 64% at a scan rate of 5 mV s^{-1}, further confirming the dominance of surface-controlled processes in the enhanced performance of the B:g-C_3N_4/O:g-C_3N_4 composite, as shown in **Figure 5b.6b**. We have done the capacitive contribution calculation, scan rate varying from 1mV s^{-1} to 5mV s^{-1}, where with an increase in scan rate, the capacitive contribution increases from 48% to 64% indicating that at higher scan rates, the capacitive contribution becomes more significant, shown in **Figure 5b.6c**. This observation suggests that electrolyte ions have adequate time for faradaic interactions with the electrode materials at lower scan rates, whereas at higher scan rates, ions do not have sufficient time to engage with the electrodes, resulting in non-faradaic charge storage.

Table 5b.1: Comparison table of Specific Capacitances of the present work with g-C_3N_4-based supercapacitor electrode materials from the literature

System	Specific Capacitance of the electrode ($F\ g^{-1}$)	Electrolyte	Reference
B:g-C_3N_4 / O:g-C_3N_4	**366 F g^{-1} @ 1 A g^{-1}**	**2M KOH**	**This work**
NMCNFs	220 @ 0.2 A g^{-1}	2 M Li_2SO_4	39
3D g-C_3N_4/graphene	243.8 @ 1 A g^{-1}	6 M KOH	40
GCN	137.67 @ 1 A g^{-1}	0.5 M H_2SO_4	41
GCN/Bio-C	300 @ 1 A g^{-1}	0.5 M H_2SO_4	42
MGCN-0.3	286 @ 0.75 A g^{-1}	1 M H_2SO_4	43
O doped g-C_3N_4	262.5 @ 1 A g^{-1}	0.5 M Na_2SO_4	44
NiS_2@m-g-C_3N_4/gra	373.5 @ 1 A g^{-1}	2 M KOH	45
$NiCo_2S_4$ NSs/P-g-C_3N_4	277 @ 1 A g^{-1}	2 M KOH	46
3D RuO_2/g-C_3N_4@rGO	704.3 @ 0.5 A g^{-1}	6 M KOH	47
f-g-C_3N_4/f-CNF–TNS	817 @ 0.25 A g^{-1}	4M KOH	48
g-C_3N_4/$Ti_3C_2T_x$	414 @ 1 A g^{-1}	1 M H_2SO_4	49
SnS_2/g-C_3N_4	527 @ 0.5 A g^{-1}	3 M KOH	50

6.3.5. Electrochemical Impedance Spectroscopy Analyses followed by DRT:

Electrochemical impedance spectroscopy (EIS) is conducted to investigate the charge–discharge dynamics, as illustrated by the Nyquist plot (**Figure 5b.6a**). A very low series resistance (3.3 Ω) and charge transfer resistance (2.1 Ω) are estimated from the high-frequency region (inset of **Figure 5b.6a**) for the composite, indicating better conductivity and charge transport in the B:g-C_3N_4/O:g-C_3N_4 material. In the low-frequency region, both the B:g-C_3N_4/O:g-C_3N_4 composite and its bare counterparts, B:g-C_3N_4 and O:g-C_3N_4, exhibit a higher slope of the vertical line, indicative of ideal capacitive behavior. The steepness of the slope in the low-frequency region indicates the diffusion resistance of the electrodes. O:g-C_3N_4 with a steeper slope has a relatively high diffusion resistance compared to B:g-C_3N_4; and it appears that B:g-C_3N_4/O:g-C_3N_4 resistance value falls in between due to the combination of both materials.[51]

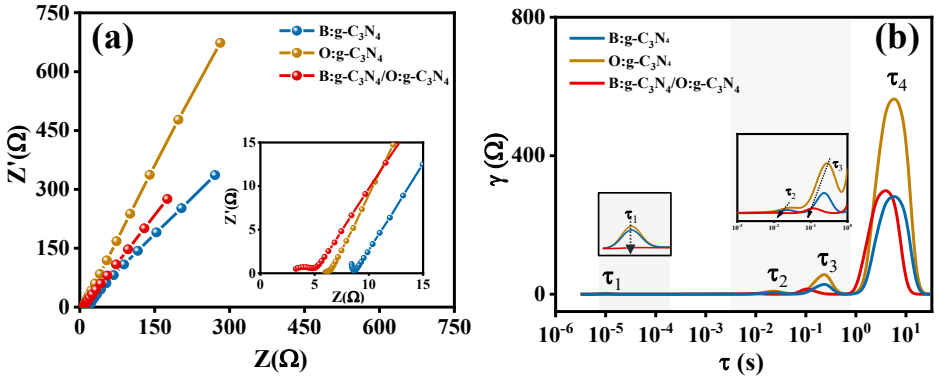

Figure 5b.7: (a) Nyquist plot of electrodes obtained from EIS (b) distribution of relaxation time curve of B:g-C_3N_4/O:g-C_3N_4 composite, B:g-C_3N_4, O:g-C_3N_4 (inset showing enlarged image of τ_1, τ_2, τ_3 peak)

To further elucidate the electrochemical processes within B:g-C_3N_4/O:g-C_3N_4, Distribution of Relaxation Times (DRT) analysis is employed using EIS data. **Figure 5b.7b** illustrates the DRT profile featuring four peaks, where:

τ_1: interfacial contact/conductivity of B:g-C_3N_4/O:g-C_3N_4

τ_2, τ_3: charge transfer process associated with the electrolyte, i.e. process involves electrolyte ion adsorption/desorption and rearrangement at the interface

τ_4: ion diffusion processes at the electrode/electrolyte interface

Table 5b.2: Represents the calculated resistance of each electrode obtained from DRT analysis

Material	**τ_1 Resistance(Ω)**	**τ_2 Resistance(Ω)**	**τ_3 Resistance(Ω)**	**τ_4 Resistance(Ω)**
O:g-C_3N_4	7.8×10^{-8}	0.00332	0.256	54.7
B:g-C_3N_4	3.64×10^{-9}	5.15×10^{-4}	0.0304	15.3
B:g-C_3N_4 /O:g-C_3N_4	**9.22×10^{-9}**	**5.22×10^{-5}**	**0.00728**	**18.8**

The resistances associated with various electrochemical processes are summarized in **Table 5b.2**. The resistance values for peaks τ_1, τ_2, and τ_3 correspond to conductivity, charge transfer, are significantly lower for the B:g-C_3N_4/O:g-C_3N_4 composite, whereas τ_4, corresponding to ion diffusion, has an intermediate resistance value for the composite, consistent with the EIS result. This improvement in charge transfer resistance in B:g-C_3N_4/O:g-C_3N_4 composite is further reflected in the faster relaxation times for τ_2 and τ_3 compared to bare B:g-C_3N_4 and O:g-C_3N_4.

These findings indicate an enhanced interfacial charge transfer and reduced ion diffusion resistance, substantially improving overall electrochemical performance.

5b.3.6. Electrochemical Characterization of Asymmetric Supercapacitor:

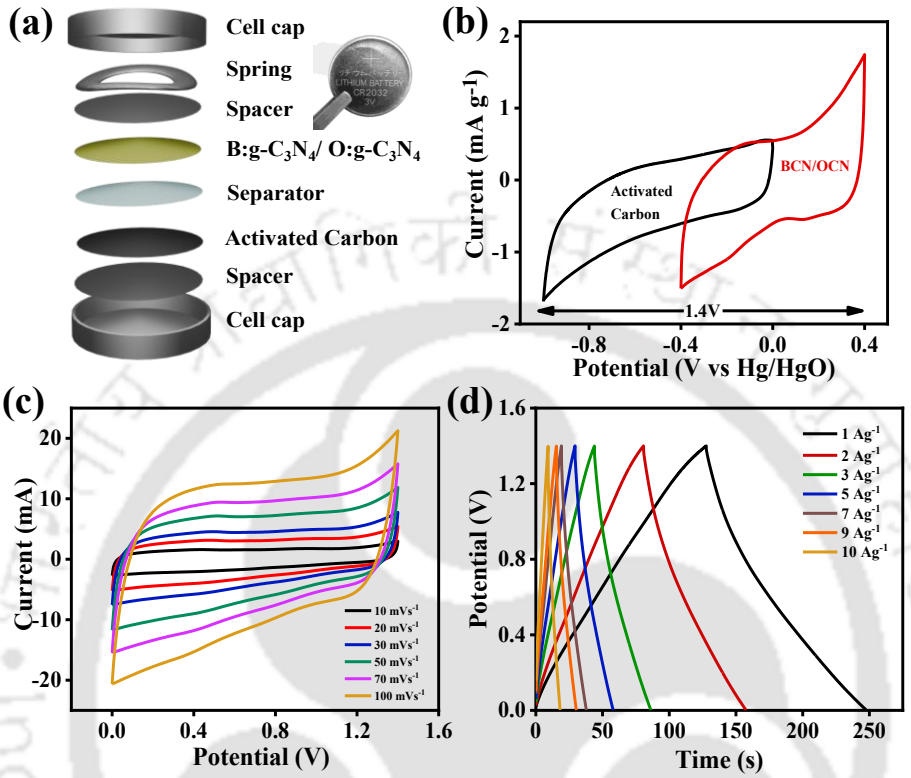

Figure 5b.8: (a) Schematic of the coin-cell supercapacitor device tested (inset showing CR2032 coin cell) (b) CV curves of AC and BCN/OCN electrodes in a three-electrode system with a scan rate of 10 mV s^{-1}, (c) CV curves from 10 to 100 mVs^{-1} (d) GCD curves from 1 to 10 Ag^{-1} of the BCN/OCN//AC coin cell asymmetric device

After thoroughly analyzing the physicochemical properties of the materials, the B:g-C_3N_4/O:g-C_3N_4 composite, along with its pristine counterparts, B:g-C_3N_4, O:g-C_3N_4, each paired with activated carbon (AC) as a counter electrode, is employed for practical application. The electrochemical testing is conducted in an asymmetrical coin cell architecture (CR2032), as shown in **Figure 5b.8a**. Individual electrodes are prepared by coating the active materials onto a carbon paper substrate. These active materials coated on carbon paper are stacked back-to-back within the cell, with the supporting membrane containing aqueous 2 M KOH electrolyte, acting as the ion-permeable charge separator, and providing direct electrical contact between the current collector and the active material. **Figure 5b.8b** presents the cyclic

voltammetry (CV) profiles of AC and B:g-C_3N_4/O:g-C_3N_4 electrodes with their respective stable potential windows at a scan rate of 10 mVs^{-1}. The AC electrode operates in the negative potential range (0 to −1 V), while the B:g-C_3N_4/O:g-C_3N_4 electrode functions within -0.4 to 0.4 V, and this complementary behavior enables an extended operating voltage window of 0-1.4 V in the asymmetric B:g-C_3N_4/O:g-C_3N_4//AC device. CV measurements of the B:g-C_3N_4/O:g-C_3N_4//AC coin-cell asymmetric supercapacitor device are performed within the potential range of 0–1.4 V at different scan rates ranging from 10 to 100 mVs^{-1}, as shown in **Figure 5b.8c**. The CV curves exhibit quasi-rectangular shapes even at high scan rates, suggesting an ideal capacitive behavior and shape is maintained even at high scan rates, indicating the excellent rate capability of asymmetric device. The GCD profile of the asymmetric coin-cell supercapacitor device exhibited a quasi-triangular shape, as observed in the CV results, owing to the dominant capacitive nature of the B:g-C_3N_4/O:g-C_3N_4 electrode **Figure 5b.8d**. Furthermore, with an increase in current density from 1 to 10 A g^{-1}, the B:g-C_3N_4/O:g-C_3N_4//AC coin-cell device demonstrated a remarkable rate capability of 73.67±5% The B:g-C_3N_4/O:g-C_3N_4//AC asymmetric coin-cell supercapacitor delivered a maximum energy density of 24 $Whkg^{-1}$ at a power density of 700 Wkg^{-1} (at 1 A g^{-1}), and even at a high-power density of 7 kW kg^{-1}, it maintained an energy density of 17.5 Wh kg^{-1}(at 10 A g^{-1}), confirming its high energy and power efficiencies.

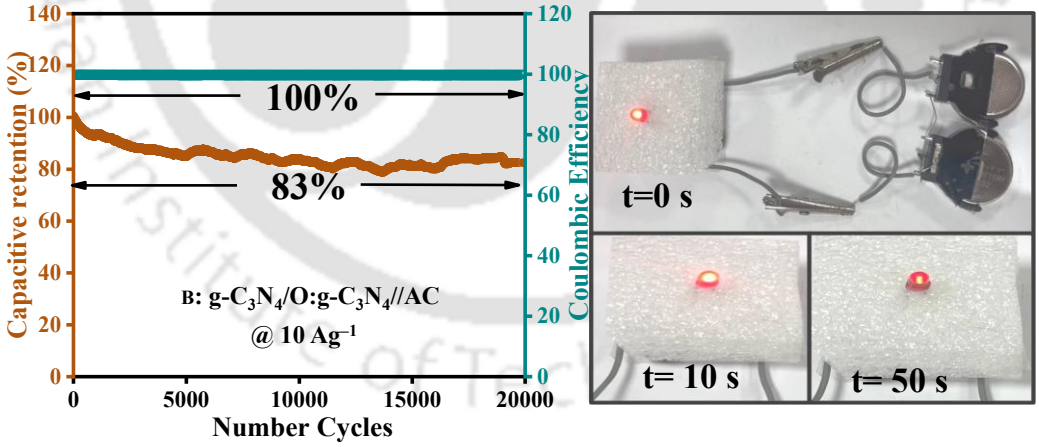

Figure 5b.9: (a) Long-term cycling performance and Coulombic efficiency of the device at a current density of 10 A g^{-1} over 20,000 cycles (b) digital photograph of LEDs powered by coin cell devices in series connection.

The stability of the supercapacitor device is important for practical applications. Thus, to evaluate this, the B:g-C_3N_4/O:g-C_3N_4//AC asymmetric supercapacitor coin cell is tested for

20,000 GCD cycles at a current density of 10 Ag^{-1}, as illustrated in **Figure 5b.9a**. The device maintained 83% retention of its specific capacitance with a coulombic efficiency of 100% after 20,000 cycles, indicating excellent electrochemical stability. Lastly, as shown in **Figure 5b.9b**, the practical applicability of the B:g-C_3N_4/O:g-C_3N_4//AC device is demonstrated by connecting two such devices in series and charging them to 2.8 V to power a red light-emitting diode (LED) with a voltage of 2 V. Upon discharge, the LED illuminated brightly and gradually dimmed, with visible brightness lasting for 50 seconds. These results underscore the promising potential of the assembled B:g-C_3N_4/O:g-C_3N_4//AC device for future energy storage applications.

5b.3.7. Plausible Mechanism of Charge Storage Mechanism:

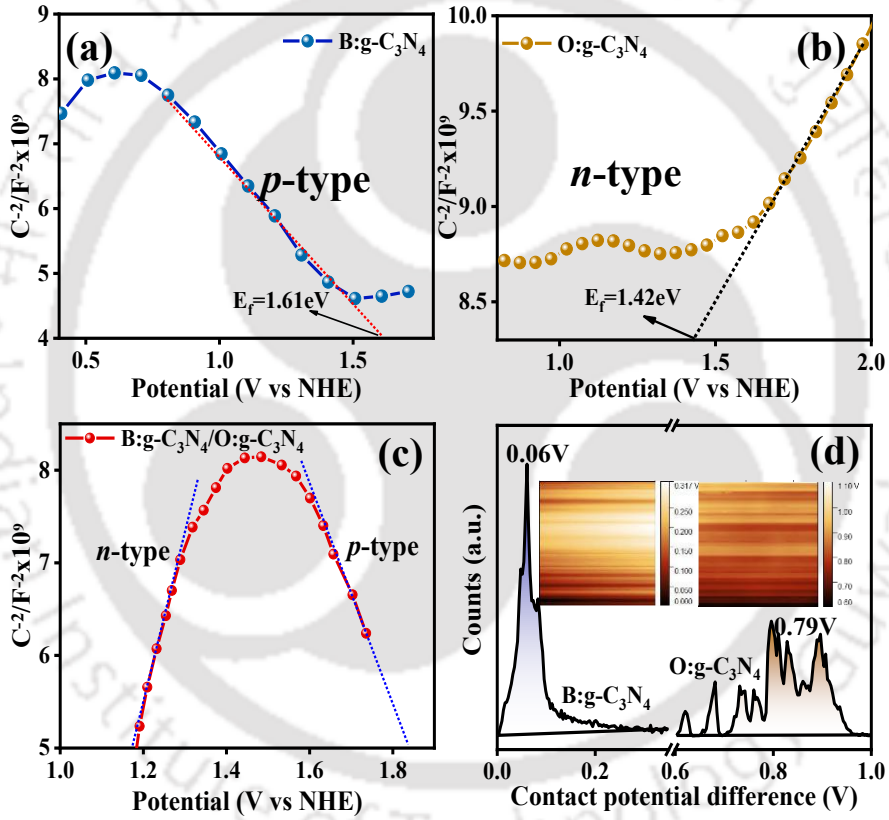

Figure 5b.10: Mott–Schottky curves of (a) B:g-C_3N_4(b) O:g-C_3N_4 (c) B:g-C_3N_4/O:g-C_3N_4 (d) Surface potential image from KPFM measurements on the sample and corresponding electric potential distribution image

The energy band structure is a key factor in determining the fundamental properties of materials and plays a crucial role in charge transport performance, as well as in their chemical and electrochemical behavior. To further elucidate the energy level structure and charge redistribution behavior in the B:g-C_3N_4/O:g-C_3N_4 composite, and thereby to explain enhanced

electrochemical activity of the composite electrodes, a detailed band alignment analysis and investigation of interfacial charge dynamics are conducted. Due to doping within the GCN framework, these materials typically exhibit characteristics of either p-type or n-type semiconductors, as determined by Mott-Schottky (M–S) measurements. As shown in **Figure 5b.10(a-b)**, the Mott-Schottky plots of B:g-C_3N_4 and O:g-C_3N_4 display linear regions with negative and positive slopes, respectively, indicating that B:g-C_3N_4 is a p-type semiconductor while O:g-C_3N_4 is n-type.[52] However, the B:g-C_3N_4/O:g-C_3N_4 shows a typical volcano M-S curve with both positive and negative slopes **(Figure 5b.10c)**, signifying the formation of p-n homojunctions. The band gap of pristine GCN is about 2.7 eV, which decreases to 2.3 eV for B:g-$C_3N_4$and increases to 2.6 eV for O:g-C_3N_4, as calculated from UV-Vis DRS Tauc plots. Furthermore, the valence band maximum (VBM) is determined using XPS valence band spectra, yielding values of 1.53 eV for B:g-C_3N_4 and 1.86 eV for O:g-C_3N_4. Using the relation E(VB) = E(CB) + E_g, the conduction band (CB) positions are calculated to be −0.72 eV for B:g-C_3N_4 and −0.27 eV for O:g-C_3N_4. Based on the calculated energy levels, B:g-$C_3N_4$and O:g-C_3N_4 form a type II *p–n* homojunction upon contact. Due to their work function difference (4.4 eV for B:g-C_3N_4 and 3.71 eV for O:g-C_3N_4), electrons flow from O:g-C_3N_4 to B:g-C_3N_4, as supported by XPS data (**Figure 5b.3).**

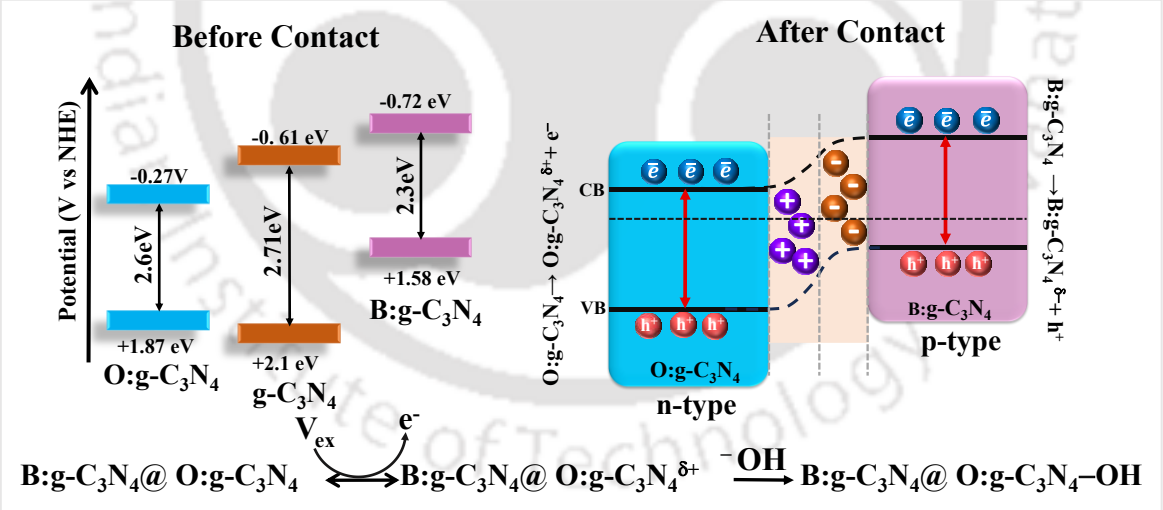

Figure 5b.11: (a)Energy level construction depicting before and after contact between *p*-type B:g-C_3N_4 and *n*-type O:g-C_3N_4, forming a *p–n* junction.

Electron transfer induces band bending and forms a built-in electric field, which drives efficient electron–hole separation, suppresses recombination, and improves charge transport. The resulting charge separation increases the polarity of the composite surface, thereby enhancing interaction between the electrode surface and electrolyte ions by facilitating ion adsorption and

improving ion diffusion kinetics (**Figure 5b.11**). These synergistic effects contribute to a notable improvement in electrochemical performance, including increased capacitance and better rate capability.

5b.4. CONCLUSIONS:

In conclusion, the synergistic effect of non-metal doping and homojunction formation in g-C_3N_4-based materials is successfully utilized to achieve enhanced energy storage performances. The electrostatic self-assembly method was utilized in order to successfully synthesize the homojunction of B:g-C_3N_4 nanotubes with O:g-C_3N_4 2D sheets. The inherent electric field produced at this interface markedly improved charge transport, leading to an enhancement in the intrinsic activity of the electrode. The unique hollow structure of B:g-C_3N_4 and the layered O:g-C_3N_4 nanosheets provided enough surface for ion diffusion, enabling a high specific capacitance of 366 F g^{-1} at 1 A g^{-1}. The asymmetric assembled B:g-C_3N_4 /O:g-C_3N_4 // AC coin cell demonstrated an energy density of 24 Wh kg^{-1} at a power density of 700 W kg^{-1}, exhibiting remarkable cycling stability by retaining 83% of its initial capacitance and achieving 100% coulombic efficiency after 20,000 charge–discharge cycles. This investigation highlights the potential of homojunction engineering and non-metal doping techniques in the creation of high-performance, metal-free electrode materials for cutting-edge electrochemical energy storage systems.

Author Contributions:

Alpana Sahu conceptualized and conducted all the experiments, analyzed the results, and wrote the manuscript. Peeyush Pandey contributed by analyzing the results and offering guidance. Mohammad Qureshi evaluated the results along with the overall coordination of the experiments, funding, and manuscript writing.

5b.5. REFERENCES:

1. P. E. Brockway, A. Owen, L. I. Brand-Correa, L. Hardt, *Nat. Energy* **2019**, *4*, 612.
2. S. Zhang, N. Pan, *Adv. Energy Mater.* **2015**, *5*, 1401401.
3. K. Krishnamoorthy, P. Pazhamalai, S.-J. Kim, *Energy Environ. Sci.* **2018**, *11*, 1595.
4. D. Larcher, J.-M. Tarascon, *Nat. Chem.* **2015**, *7*, 19.
5. Reenu, Sonia, L. Phor, A. Kumar, S. Chahal, *J. Energy Storage* **2024**, *84*, 110698.
6. L. Hao, X. Li, L. Zhi, *Adv. Mater.* **2013**, *25*, 3899.
7. B. Maria Mahimai, E. Li, J. Pang, J. Zhang, J. Zhang, *J Energy Storage* **2024**, *96*, 112598.
8. J. P. Paraknowitsch, A. Thomas, *Energy Environ. Sci.* **2013**, *6*, 2839.

9. F. Liu, Z. Fan, *Chem Soc Rev* **2023**, *52*, 1723.
10. S. Chen, W. Xing, J. Duan, X. Hu, S. Z. Qiao, *J. Mater. Chem. A* **2013**, *1*, 2941.
11. S. Adhikari, G.-H. Noh, A. T. Sivagurunathan, D.-H. Kim, *J Mater. Chem. A* **2025**, *13*, 16912.
12. I. Hussain, M. Z. Ansari, C. Lamiel, T. Hussain, M. S. Javed, T. Kaewmaraya, M. Ahmad, N. Qin, K. Zhang, *ACS Energy Lett.* **2023**, *8*, 1887.
13. L. Bai, H. Huang, S. Zhang, L. Hao, Z. Zhang, H. Li, L. Sun, L. Guo, H. Huang, Y. Zhang, *Adv. Science* **2020**, *7*,2001939.
14. Y. Hong, J. Yang, W. Choi, J. Wang, J. Xu, *ACS Appl. Energy Mater* **2021**, *4*, 1496.
15. M. Li, J.-S. Chen, M. Cotlet, *ACS Energy Lett.* **2019**, *4*, 2323.
16. G. Wu, W. Zhang, Z. Mo, X. Zhao, P. Sun, Q. Wang, P. Yan, X. She, H. Xu, *ACS Catal.* **2025**, *15*, 8822.
17. J. Wang, Y. Zhang, S. Jiang, C. Sun, S. Song, *Angew. Chem. Int. Ed.* **2023**, *62*, 2307808.
18. W. Li, Y. Shen, X. Xiao, C. An, G. Wei, Y. Wang, J. Wang, Y. Wu, C. An, *ACS Appl. Energy Mater.* **2019**, *2*, 8337.
19. M. Ghaemmaghami, R. Mohammadi, *Sustain. Energy Fuels* **2019**, *3*, 2176.
20. Z. Zhou, Y. Zhang, Y. Shen, S. Liu, Y. Zhang, *Chem. Soc. Rev.* **2018**, *47*, 2298.
21. X. Xin, Y. Xu, H. Wuliji, F. Sun, Q. Liu, Z. Wang, T. Wei, X. Zhao, X. Song, L. Gao, *ACS Nano* **2023**, *17*, 657.
22. L. Chen, J. Song, *Adv. Funct. Mater.* **2017**, *27*, 1702695.
23. T. H. Nguyen, D. Yang, B. Zhu, H. Lin, T. Ma, B. Jia, *J Mater. Chem. A* **2021**, *9*, 7366.
24. M. Devi, S. Yesmin, B. Das, S. S. Dhar, R. Dasgupta, *Energy & Fuels* **2023**, *37*, 3247.
25. S. Vinoth, K. Subramani, W.-J. Ong, M. Sathish, A. Pandikumar, *J Colloid. Interface Sci.* **2021**, *584*, 204.
26. R. Justinabraham, A. Durairaj, S. Ramanathan, A. Obadiah, R. John wesley, X. Lv, S. Vasanthkumar, *J Energy Storage* **2021**, *40*, 102786.
27. J. Zhao, H. Lai, Z. Lyu, Y. Jiang, K. Xie, X. Wang, Q. Wu, L. Yang, Z. Jin, Y. Ma, J. Liu, Z. Hu, *Adv. Mater.* **2015**, *27*, 3541.
28. Z. Lin, K. Wang, X. Wang, S. Wang, H. Pan, Y. Liu, S. Xu, S. Cao, *ACS Appl. Nano Mater* **2020**, *3*, 7016.
29. D. Zhao, C. Dong, B. Wang, C. Chen, Y. Huang, Z. Diao, S. Li, L. Guo, S. Shen, *Adv. Mater.* **2019**, *31*, 1903545.
30. P. Liu, T. Liang, Y. Li, Z. Zhang, Z. Li, J. Bian, L. Jing, *Nat. Commun.* **2024**, *15*, 9224.
31. D. Cvejn, H. Starukh, M. Koštejn, P. Peikertová, P. Praus, *Mater. Today Chem.* **2024**, *39*, 102157.
32. M. Tahir, C. Cao, N. Mahmood, F. K. Butt, A. Mahmood, F. Idrees, S. Hussain, M. Tanveer, Z. Ali, I. Aslam, *ACS Appl. Mater. Interfaces* **2014**, *6*, 1258.
33. M. Tahir, C. Cao, F. K. Butt, F. Idrees, N. Mahmood, Z. Ali, I. Aslam, M. Tanveer, M. Rizwan, T. Mahmood, *J Mater. Chem. A* **2013**, *1*, 13949.
34. H. Xie, Y. Zheng, X. Guo, Y. Liu, Z. Zhang, J. Zhao, W. Zhang, Y. Wang, Y. Huang, *ACS Sustain. Chem. Eng.* **2021**, *9*, 6788.

35. J. Pan, J. Wang, *Nanoscale Adv.* **2020**, *2*, 149.
36. H. Xie, Y. Zheng, X. Guo, Y. Liu, Z. Zhang, J. Zhao, W. Zhang, Y. Wang, Y. Huang, *ACS Sustain. Chem. Eng.* **2021**, *9*, 6788.
37. H. S. H. Mohamed, L. Wu, C.-F. Li, Z.-Y. Hu, J. Liu, Z. Deng, L.-H. Chen, Y. Li, B.-L. Su, *ACS Appl. Mater. Interfaces* **2019**, *11*, 32957.
38. J. Fu, B. Zhu, C. Jiang, B. Cheng, W. You, J. Yu, *Small* **2017**, *13*, 1603938.
39. Liang, Q.; Ye, L.; Xu, Q.; Huang, Z.-H.; Kang, F.; Yang, Q.-H. *Carbon* **2015**, *94*, 342.
40. Lin, R.; Li, Z.; Abou El Amaiem, D. I.; Zhang, B.; Brett, D. J. L.; He, G.; Parkin, I. P. A . *J Mater Chem A* **2017**, *5*, 25545.
41. Ghanem, L. G.; Hamza, M. A.; Taha, M. M.; Allam, N. K. *J Energy Storage* **2022**, *52*, 104850.
42. Taha, M. M.; Ghanem, L. G.; Hamza, M. A.; Allam, N. K. *ACS Appl. Energy Mater.* **2021**, *4*, 10344.
43. Idris, M. B.; Devaraj, S. *J Energy Storage* **2019**, *26*, 101032.
44. Devi, M.; Yesmin, S.; Das, B.; Dhar, S. S.; Dasgupta, R. *Energy & Fuels* **2023**, *37* , 3247.
45. Wu, Y.; Wei, W.; Ding, T.; Chen, S.; Zhai, R.; Bai, C. *J Mater. Chem. A* **2021**, *9*, 7791.
46. Li, Z.; Wu, L.; Wang, L.; Gu, A.; Zhou, Q. *Electrochim. Acta* **2017**, *231*, 617.
47. Zhang, J., Ding, J., Li, C., Li, B., Li, D., Liu, Z., Liu, Y. *ACS Sustain. Chem. & Eng.*, **2017**, *5*, 4982.
48. Zhang, S.; Huang, Y.; Wang, J.; Han, X.; Chen, C.; Sun, X. *Appl. Surf. Sci.* **2022**, *599*, 154015.
49. Nallapureddy, R. R.; Pallavolu, M. R.; Joo, S. W. *Energy & Fuels* **2021**, *35*, 1796.
50. Xu, Y.; Zhou, Y.; Guo, J.; Zhang, S.; Lu, Y. *J. Alloys Compd.* **2019**, *806*, 343.
51. A. Ch. Lazanas, M. I. Prodromidis, *ACS Measurement Science Au* **2023**, *3*, 162.
52. N. Sagara, S. Kamimura, T. Tsubota, T. Ohno, *Appl. Catal. B* **2016**, *192*, 193.

CHAPTER 6

Thesis overview and future perspective

This chapter, in brief, outlines the outcomes and overview of the current thesis. Herein, it also discusses the possible modification and development that can be done on 2D materials to enhance their charge storage for supercapacitor applications.

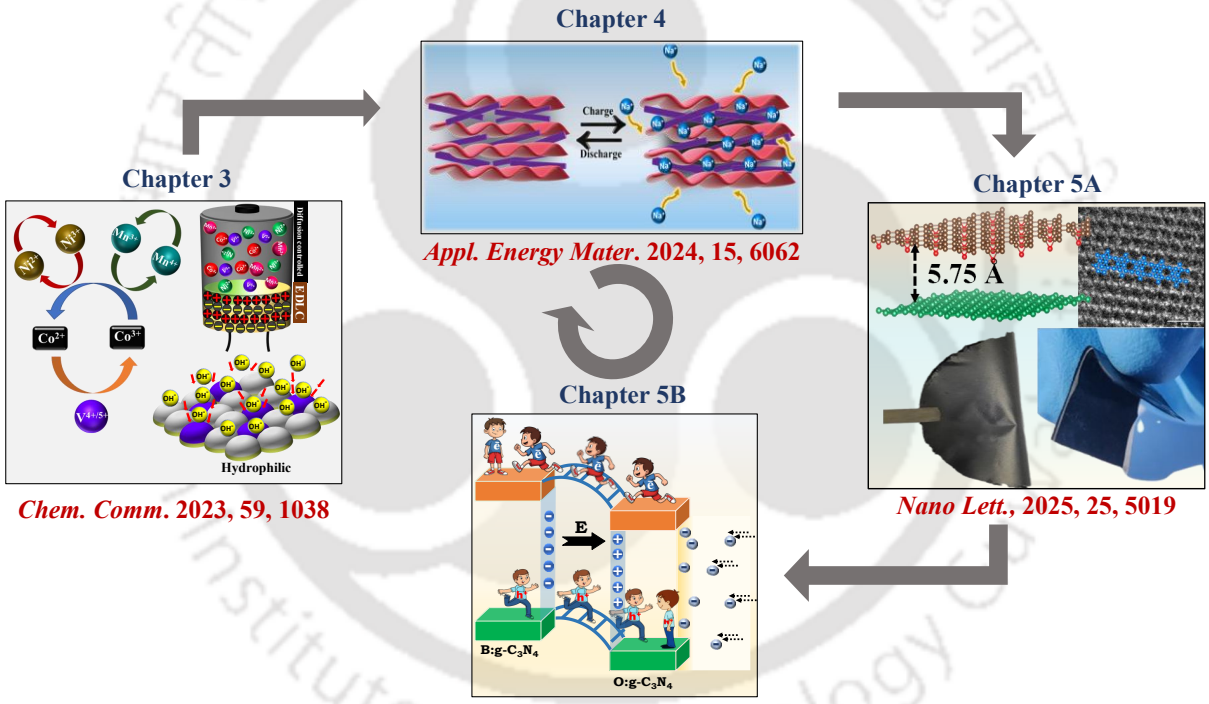

6.1. THESIS OVERVIEW:

The thesis mainly focused on the diverse strategies to be utilized for the betterment of charge storage of supercapacitors by utilizing 2D materials. The charge storage efficiency of the 2D materials was modified utilizing different methods like composite formation, elemental doping, morphological tuning, and junction formation. During the synthesis of the electrode materials, the hydrothermal and calcination routes were utilised considering their simplicity, cost-effectiveness, and environmentally friendly nature. The thesis prioritizes the different strategies utilized for the development of 2D materials and tuning the electronic and/or structural features based on their intrinsic properties. The summary and conclusions for each chapter (valuable outcomes obtained from the work done during my Ph.D. tenure) are summarized as follows:

- **Chapter 1**: In this discussion, we have pointed out that the increasing electricity demand, our reliance on fossil fuels, and the unpredictable nature of renewable energy sources all underscore the urgent need for effective energy storage systems, leading to the emergence of electrochemical supercapacitors, ensuring a reliable and sustainable power supply. The basic principle of different charge storage mechanisms and different strategies to enhance supercapacitor performance of a 2D material are discussed. A brief literature survey on the current state-of-the-art, as well as challenges related to the modification of 2D material, is also discussed. At last, this chapter is concluded with the objectives of the present thesis.
- **Chapter 2:** The different instrumental techniques, performance parameters, and different experimental setups, which were adopted for the characterization of the as-synthesized materials/ supercapacitor devices and determination of performance of the fabricated supercapacitor electrodes, are discussed in detail.
- **Chapter 3:** In this chapter, we have explored the criticality of spectator-metal ions such as vanadium in enhancing the electrochemical charge-storage performance in supercapacitors. The incorporation of high valent V ion induces more hydrophilicity, promoting the adsorption of the electrolyte/hydroxyl ions on the surface of COV, thereby increasing the redox cycles of Co ion. Vanadium-incorporated CoO(OH) combined with NiMn-LDH, yields a specific capacitance of 786 Fg^{-1} at $1Ag^{-1}$ with 96% retention, confirming its high activity and durability. The assembled asymmetric supercapacitor exhibits an energy density of 46 Wh Kg^{-1} at a power density 752 W kg^{-1}.
- **Chapter 4:** In this chapter, a synergistic approach of combining capacitive and redox-active materials is employed to develop supercapacitors that effectively bridge the gap

between traditional supercapacitors and batteries in terms of their high-power delivery and increased energy storage capacity. Here, we have reported MXene with manganese vanadium oxide ($Mn_2V_2O_7$) nanorods to eliminate the limitations such as restacking of MXenes, which poses a major problem in achieving high conductivity to be used in supercapacitor applications. Formation of pathways for ion migration in $Mn_2V_2O_7$/MXene composite resulting in increased conductivity, enhanced ion transport capacity, and structural stability in aqueous electrolytes, leading to superior performance with a specific capacitance of 627 F g^{-1} at 1 A g^{-1}. Assembled device $Mn_2V_2O_7$/MXene//AC gives a high potential window of 2 V with a high specific energy of 65 Wh kg^{-1} at a power density of 1000 W kg^{-1}. Moreover, complex impedance spectra are extracted using the Distribution of relaxation time (DRT) analysis to get insights into electrochemical processes with enhanced resolution to understand the dynamics of the charge transfer kinetic processes.

- **Chapter 5:** In this chapter, we have utilised semi-metallic Dirac Borophene 2D material and explored its charge storage properties. Borophene requires conductive substrates for stability, which limits its potential for energy storage applications. To address this, a strategy for fabricating flexible and conductive rGO-supported borophene supercapacitor electrodes is proposed, featuring a layered assembly of borophene nanosheets sandwiched between rGO layers. This architecture effectively prevents the self-restacking of rGO nanosheets, leading to a significant increase in interlayer spacing of 5.75 Å between rGO and borophene, promoting a rapid diffusion of electrolyte ions, making more electroactive sites accessible for electrochemical storage. The freestanding rGO/borophene electrode achieves a capacitance of 328 Fg^{-1} at 1 Ag^{-1}, with excellent rate capability, 98% capacitance retention at 10 Ag^{-1}, and long cycling stability. Additionally, the fabricated flexible symmetric supercapacitor achieves an energy density of 24.3 Wh kg^{-1} at a power density of 600 W kg^{-1} and maintains a stable energy output even under bending angles of up to 180°. DFT calculations reveal that boron and carbon significantly enhance electron density near the Fermi level, enabling semi-metallic behavior for rapid electron transfer, crucial for high-performance supercapacitors.
- **Chapter 5b:** In this chapter, we have utilised a doping and junction strategy to improve the charge storage performance by virtue of its increased intrinsic conductivity. Electronic structure modification and precise band alignments, including optimized

work function, enable the formation of a depletion zone at the material interface, which facilitates accumulation/storage of charges. Building on this principle, rational design of composite electrode materials consists of oxygen-doped g-C_3N_4 (O:g-C_3N_4) nanosheets exhibiting *n*-type characteristics combined with boron-doped g-C_3N_4 (B:g-C_3N_4) hollow nanotubes, which show a typical *p*-type carrier transport resulting in a well-defined homo-interface (*p–n*). The doping strategy successfully aligns the band positions of g-C_3N_4, with O:g-C_3N_4 and B:g-C_3N_4 aiding in redistribution of charges within the *p-n* junction, leading to the formation of space-charge regions and a built-in electric field, which promotes charge transfer at the interface. Unique hollow tubular morphology of B: g-C_3N_4 coupled with 2D layered structure of O:g-C_3N_4, affords a high surface area and shorter ion diffusion path, enabling rapid ion transport and enhanced electrochemical performance, achieving a remarkable specific capacitance of 366 F g^{-1} at 1 A g^{-1}. An asymmetric two-electrode supercapacitor using B:g-C_3N_4 /O:g-C_3N_4 as a positive electrode achieves an energy density of 24 Wh kg^{-1} @ 700 W kg^{-1}, demonstrating 83% capacitance retention at 100% coulombic efficiency after 20,000 charge-discharge cycles.

6.2. FUTURE PROSPECTIVES:

The presented thesis outlined the design aspects of 2D materials-based electrodes for energy storage performance in supercapacitor during the research tenure. A detailed study on 2D-material-based electrodes was carried out to resolve critical issues such as interfacial charge transfer resistance, limited ion diffusion, and the inherent restacking tendency of 2D layers, which restricts the electrochemically active surface area and hampers supercapacitor performance. Although, several strategies have been adopted here making substantial advancements in the field of supercapacitor, numerous scopes are still available to further improve the overall efficiency towards commercialization. The plausible scopes for the advancement of energy storage towards practicality are as follows:

- ✓ Designing high-performance supercapacitor electrodes considering pore size distribution, surface bonding, electrical conductivity, and mass transport properties.
- ✓ Using abundant and sustainable raw materials can considerably lower production costs. Research into alternate precursors for synthesis of 2D materials can lead to cost-effective production procedures, including next-generation supercapacitors.

- ✓ Future research should prioritize innovative, scalable, and cost-effective synthesis approaches. For example, chemical vapor deposition (CVD) and electrochemical exfoliation techniques could be optimized for mass manufacturing while lowering costs. Advanced electrode topologies, such as 3D porous structures or hybrid nanostructures, can improve ion diffusion and electron transport, resulting in greater performance in practical supercapacitor systems.
- ✓ Incorporating 2D materials into flexible and wearable electrical systems is a potential approach. Research should concentrate on improving the mechanical characteristics of 2D materials in order to preserve performance during deformation.
- ✓ To ensure long-term reliability, aqueous electrolyte supercapacitors require corrosion-resistant materials or coatings. Alternative organic electrolytes can also be used.
- ✓ Choosing the right electrolyte is crucial and should be customized based on the specific 2D electrode material to get a balance between voltage, conductivity, safety, and cycle life to achieve the best performance in next-generation supercapacitors.

LIST OF PUBLICATIONS

AND

CONFERENCES ATTENDED

JOURNAL ARTICLES:

Included in the thesis:

1. **Alpana Sahu**, Partha Pratim Borah, Kalishankar Bhattacharyya*, Mohammad Qureshi* Harnessing Dirac Semi-Metallicity in a Metal-Free Stand-alone Borophene Composite Electrode for High-Performance Supercapacitors. ***Nano Letters***, 2025, 25, 12, 5019–5026.
2. **Alpana Sahu**, N Anjana Singha, Mohammad Qureshi* Interplay of Capacitive and Diffusion Contributions in Redox Active Complex Metal Oxide Rods Channelled into MXene for Improved Charge Transfer Dynamics. ***ACS Applied Energy Materials***, 2024, 7, 15, 6062–6070.
3. **Alpana Sahu**, Peeyush Pandey, Sourav Bhowmick, Mohammad Qureshi* Spectator-metal ion guided redox-dominant cobalt oxy hydroxide as a high-performance supercapacitor. ***Chemical Communication***, 2023,59, 1038-1041.

Work contributed off the thesis:

4. Moumita Chandra, Peeyush Pandey, **Alpana Sahu**, Mohammad Qureshi* Magnetic Stimuli-Guided Multiple Charge Transfer Pathways for Boosted Overall Water Splitting. ***ACS Applied Energy Materials***, 2024, 7, 15, 6062–6070.
5. Moumita Chandra, **Alpana Sahu**, Nitul Kalita, Mohammad Qureshi* Geometry twisted intra-inter molecular cooperative interactions for enhanced photo-response in ORMOSIL based host-guest system. ***Chemical Communication,*** 2024, 60, 8553-8556
6. N Anjana Singha, Peeyush Pandey, **Alpana Sahu**, Mohammad Qureshi* Ultrathin Dielectric Triggered Charge Injection Dynamics for High-Performance Metal Organic Framework/MXene Supercapacitors. ***The Journal of Physical Chemistry Letters***, 2024, 15, 2123–2132.
7. **Alpana Sahu**, Aswathi K S, Amit Kumar Rajak, Roshan Naik, Mohammad Qureshi* Competing double-exchange / super-exchange ordering for enhanced water oxidation kinetics. ***Chemical Communication***, 2024, 60, 2236-2239.
8. Ching Thian Moi, **Alpana Sahu**, Mohammad Qureshi* Tapping the Potential of High-Valent Mo and W Metal Centers for Dynamic Electronic Structures in Multimetallic FeVO(OH)/$Ni(OH)_2$ for Ultrastable and Efficient Overall Water Splitting. **ACS *Applied Materials & Interfaces*,** 2023, 15, 45336–5344.

9. Nitul Kalita, **Alpana Sahu**, Sourav Bhowmick, Mohammad Qureshi* Synchronized redox pairs in metal oxide/hydroxide chemical analogues for efficient oxygen evolution reaction. ***Chemical Communication,*** 2022, 58, 13747-13750.
10. Sourav Bhowmick, Ching Thian Moi, Nitul Kalita, **Alpana Sahu**, Mohammad Qureshi* Spontaneous Fenton-like dye degradation in clustered-petal di-manganese copper oxide by virtue of self-cyclic redox couple. ***Journal of Environmental Chemical Engineering,*** 2021, 9, 106094.

CONFERENCES ATTENDED

1. Poster presentation in **Modern Trends in Inorganic Chemistry (MTIC XX),** IISc Bangalore, December 2023.
2. Poster presentation in **International Conference on Frontier Areas of Science & Technology-2024(ICFAST-2024),** IIT Guwahati, Guwahati, India, September 2024.
3. Oral presentation at **International Conference on Semiconductor Technologies-Materials to Chips (ICST-2024),** Amity University Uttar Pradesh, Noida, September 2024.
4. Poster presentation at **ACS-CRSI Early Career Researchers' Symposium 2024,** KIIT University, Bhubaneswar, October 2024.
5. Poster presentation at **7th International Conference on Frontiers in Chemical Sciences (FICS 2024),** IIT Guwahati, Guwahati, India, December 2024.

JOHN WILEY AND SONS LICENSE
TERMS AND CONDITIONS

Sep 03, 2025

This Agreement between Alpana Sahu ("You") and John Wiley and Sons ("John Wiley and Sons") consists of your license details and the terms and conditions provided by John Wiley and Sons and Copyright Clearance Center.

License Number	6101180449256
License date	Sep 03, 2025
Licensed Content Publisher	John Wiley and Sons
Licensed Content Publication	Advanced Energy Materials
Licensed Content Title	Energy Storage Data Reporting in Perspective—Guidelines for Interpreting the Performance of Electrochemical Energy Storage Systems
Licensed Content Author	Tyler S. Mathis, Narendra Kurra, Xuehang Wang, et al
Licensed Content Date	Sep 4, 2019
Licensed Content Volume	9
Licensed Content Issue	39
Licensed Content Pages	13

AMERICAN CHEMICAL SOCIETY LICENSE
TERMS AND CONDITIONS

Aug 03, 2025

This Agreement between Alpana Sahu ("You") and American Chemical Society ("American Chemical Society") consists of your license details and the terms and conditions provided by American Chemical Society and Copyright Clearance Center.

License Number	6081400080471
License date	Aug 03, 2025
Licensed Content Publisher	American Chemical Society
Licensed Content Publication	Chemical Reviews
Licensed Content Title	Pseudocapacitance: From Fundamental Understanding to High Power Energy Storage Materials
Licensed Content Author	Simon Fleischmann, James B. Mitchell, Ruocun Wang, et al
Licensed Content Date	Jul 1, 2020
Licensed Content Volume	120
Licensed Content Issue	14
Volume number	120
Issue number	14
Type of Use	Thesis/Dissertation
Requestor type	Author (original work)

CCC Marketplace

This is a License Agreement between Alpana Sahu ("User") and Copyright Clearance Center, Inc. ("CCC") on behalf of the Rightsholder identified in the order details below. The license consists of the order details, the Marketplace Permissions General Terms and Conditions below, and any Rightsholder Terms and Conditions which are included below.

All payments must be made in full to CCC in accordance with the Marketplace Permissions General Terms and Conditions below.

Order Date	29-Aug-2025	Type of Use	Republish in a thesis/dissertation
Order License ID	1646079-1	Publisher	RSC Publishing
ISSN	1754-5706	Portion	Image/photo/illustration

LICENSED CONTENT

Publication Title	Energy & environmental science	Rightsholder	Royal Society of Chemistry
Article Title	Pseudocapacitive oxide materials for high-rate electrochemical energy storage	Publication Type	e-Journal
		Start Page	1597
Author / Editor	Royal Society of Chemistry (Great Britain)	Issue	5
Date	01/01/2008	Volume	7
Language	English	URL	http://www.rsc.org/Publishing/Journals/E...
Country	United Kingdom of Great Britain and Northern Ireland		

REQUEST DETAILS

Portion Type	Image/photo/illustration	Distribution	Worldwide
Number of Images / Photos / Illustrations	1	Translation	Original language of publication
Format (select all that apply)	Print, Electronic	Copies for the Disabled?	No
Who Will Republish the Content?	Author of requested content	Minor Editing Privileges?	Yes
Duration of Use	Life of current edition	Incidental Promotional Use?	Yes

Copyright Permissions

JOHN WILEY AND SONS LICENSE
TERMS AND CONDITIONS

Aug 29, 2025

This Agreement between Alpana Sahu ("You") and John Wiley and Sons ("John Wiley and Sons") consists of your license details and the terms and conditions provided by John Wiley and Sons and Copyright Clearance Center.

License Number	6098001112891
License date	Aug 29, 2025
Licensed Content Publisher	John Wiley and Sons
Licensed Content Publication	Small
Licensed Content Title	Biomass-Derived Nitrogen-Doped Carbon Nanofiber Network: A Facile Template for Decoration of Ultrathin Nickel-Cobalt Layered Double Hydroxide Nanosheets as High-Performance Asymmetric Supercapacitor Electrode
Licensed Content Author	Feili Lai, Yue-E Miao, Lizeng Zuo, et al
Licensed Content Date	May 2, 2016
Licensed Content Volume	12
Licensed Content Issue	24
Licensed Content Pages	10
Type of use	Dissertation/Thesis
Requestor type	University/Academic

AMERICAN CHEMICAL SOCIETY LICENSE
TERMS AND CONDITIONS

Aug 29, 2025

This Agreement between Alpana Sahu ("You") and American Chemical Society ("American Chemical Society") consists of your license details and the terms and conditions provided by American Chemical Society and Copyright Clearance Center.

License Number	6098001436115
License date	Aug 29, 2025
Licensed Content Publisher	American Chemical Society
Licensed Content Publication	Chemistry of Materials
Licensed Content Title	Kinetics of Ti3AlC2 Etching for Ti3C2Tx MXene Synthesis
Licensed Content Author	Mark Anayee, Christopher E. Shuck, Mikhail Shekhirev, et al
Licensed Content Date	Nov 1, 2022
Licensed Content Volume	34
Licensed Content Issue	21
Volume number	34
Issue number	21
Type of Use	Thesis/Dissertation
Requestor type	Author (original work)

JOHN WILEY AND SONS LICENSE
TERMS AND CONDITIONS

Aug 29, 2025

This Agreement between Alpana Sahu ("You") and John Wiley and Sons ("John Wiley and Sons") consists of your license details and the terms and conditions provided by John Wiley and Sons and Copyright Clearance Center.

License Number	6098010292016
License date	Aug 29, 2025
Licensed Content Publisher	John Wiley and Sons
Licensed Content Publication	Small
Licensed Content Title	Interlayer Hydrogen-Bonded Metal Porphyrin Frameworks/MXene Hybrid Film with High Capacitance for Flexible All-Solid-State Supercapacitors
Licensed Content Author	Weiwei Zhao, Jiali Peng, Weikang Wang, et al
Licensed Content Date	Apr 8, 2019
Licensed Content Volume	15
Licensed Content Issue	18
Licensed Content Pages	10
Type of use	Dissertation/Thesis
Requestor type	University/Academic
Format	Print and electronic

AMERICAN CHEMICAL SOCIETY LICENSE
TERMS AND CONDITIONS

Aug 29, 2025

This Agreement between Alpana Sahu ("You") and American Chemical Society ("American Chemical Society") consists of your license details and the terms and conditions provided by American Chemical Society and Copyright Clearance Center.

License Number	6098010505193
License date	Aug 29, 2025
Licensed Content Publisher	American Chemical Society
Licensed Content Publication	Applied Materials
Licensed Content Title	Magnetically Triggered Interplay of Capacitive and Diffusion Contributions for Boosted Supercapacitor Performance
Licensed Content Author	Peeyush Pandey, Sourav Bhowmick, Mohammad Qureshi
Licensed Content Date	Aug 1, 2023
Licensed Content Volume	15
Licensed Content Issue	33
Volume number	15
Issue number	33
Type of Use	Thesis/Dissertation
Requestor type	Author (original work)

8/29/25, 10:07 AM RightsLink Printable License

ELSEVIER LICENSE
TERMS AND CONDITIONS

Aug 29, 2025

This Agreement between Alpana Sahu ("You") and Elsevier ("Elsevier") consists of your license details and the terms and conditions provided by Elsevier and Copyright Clearance Center.

License Number	6098010725871
License date	Aug 29, 2025
Licensed Content Publisher	Elsevier
Licensed Content Publication	Chemical Engineering Journal
Licensed Content Title	Amorphous vanadium oxides with metallic character for asymmetric supercapacitors
Licensed Content Author	Shuai Chen,Hao Jiang,Qilin Cheng,Gengchao Wang,Saha Petr,Chunzhong Li
Licensed Content Date	Jan 1, 2021
Licensed Content Volume	403
Licensed Content Issue	n/a
Licensed Content Pages	1
Start Page	126380
End Page	0
Type of Use	reuse in a thesis/dissertation

https://s100.copyright.com/AppDispatchServlet 1/7

8/29/25, 10:11 AM RightsLink Printable License

AMERICAN CHEMICAL SOCIETY LICENSE
TERMS AND CONDITIONS

Aug 29, 2025

This Agreement between Alpana Sahu ("You") and American Chemical Society ("American Chemical Society") consists of your license details and the terms and conditions provided by American Chemical Society and Copyright Clearance Center.

License Number	6098010971233
License date	Aug 29, 2025
Licensed Content Publisher	American Chemical Society
Licensed Content Publication	Applied Materials
Licensed Content Title	Self-Standing Metallic Mesh with MnO2 Multiscale Microstructures for High-Capacity Flexible Transparent Energy Storage
Licensed Content Author	Yan-Hua Liu, Zhou-Ying Jiang, Jian-Long Xu
Licensed Content Date	Jul 1, 2019
Licensed Content Volume	11
Licensed Content Issue	27
Volume number	11
Issue number	27
Type of Use	Thesis/Dissertation
Requestor type	Author (original work)

https://s100.copyright.com/AppDispatchServlet 1/4

JOHN WILEY AND SONS LICENSE
TERMS AND CONDITIONS

Sep 02, 2025

This Agreement between Alpana Sahu ("You") and John Wiley and Sons ("John Wiley and Sons") consists of your license details and the terms and conditions provided by John Wiley and Sons and Copyright Clearance Center.

License Number	6098011410576
License date	Aug 29, 2025
Licensed Content Publisher	John Wiley and Sons
Licensed Content Publication	ENERGY & ENVIRONMENTAL MATERIALS
Licensed Content Title	Definitions of Pseudocapacitive Materials: A Brief Review
Licensed Content Author	Yuqi Jiang, Jinping Liu
Licensed Content Date	Mar 5, 2019
Licensed Content Volume	2
Licensed Content Issue	1
Licensed Content Pages	8
Type of use	Dissertation/Thesis
Requestor type	University/Academic
Format	Print and electronic

8/3/25, 8:26 PM RightsLink Printable License

ELSEVIER LICENSE
TERMS AND CONDITIONS

Aug 03, 2025

This Agreement between Alpana Sahu ("You") and Elsevier ("Elsevier") consists of your license details and the terms and conditions provided by Elsevier and Copyright Clearance Center.

License Number	6080190822958
License date	Aug 01, 2025
Licensed Content Publisher	Elsevier
Licensed Content Publication	Journal of Energy Storage
Licensed Content Title	Experimental and theoretical investigation of free-binder V-doped CoP for high-performance supercapacitor and urea oxidation electrocatalyst
Licensed Content Author	M.H. Sepahdar,S.M. Masoudpanah,M.Sh. Bafghi,S. Mohammadi,M. Namayandeh Jorabchi
Licensed Content Date	Dec 20, 2024
Licensed Content Volume	104
Licensed Content Issue	n/a
Licensed Content Pages	1
Start Page	114557
End Page	0
Type of Use	reuse in a thesis/dissertation
Portion	figures/tables/illustrations
Number of figures/tables/illustrations	1
Format	both print and electronic
Are you the author of this Elsevier article?	No
Will you be translating?	No
Title of new work	Design and Development of Homo/Hetero Junction based 2D Materials for Supercapacitor Application
Institution name	IIT Guwahati
Expected presentation date	Feb 2026
Portions	Figure 2.2
The Requesting Person / Organization to Appear on the License	Alpana Sahu
Requestor Location	Ms. Alpana Sahu IIT Guwahati Guwahati, Not US or Canada 781039 India
Publisher Tax ID	GB 494 6272 12
Total	**0.00 USD**
Terms and Conditions	

INTRODUCTION

1. The publisher for this copyrighted material is Elsevier. By clicking "accept" in connection with completing this licensing transaction, you agree that the following terms and conditions apply to this transaction (along with the Billing and Payment terms and conditions established by Copyright Clearance Center, Inc. ("CCC"), at the time that you opened your RightsLink account and that are available at any time at https://myaccount.copyright.com).